2014

Reference Compensation for Localized Surface-Plasmon Resonance Sensors

Neha Nehru
University of Kentucky, nehru.neha@gmail.com

STUDENT AGREEMENT:

I represent that my thesis or dissertation and abstract are my original work. Proper attribution has been given to all outside sources. I understand that I am solely responsible for obtaining any needed copyright permissions. I have obtained needed written permission statement(s) from the owner(s) of each third-party copyrighted matter to be included in my work, allowing electronic distribution (if such use is not permitted by the fair use doctrine) which will be submitted to UKnowledge as Additional File.

I hereby grant to The University of Kentucky and its agents the irrevocable, non-exclusive, and royalty-free license to archive and make accessible my work in whole or in part in all forms of media, now or hereafter known. I agree that the document mentioned above may be made available immediately for worldwide access unless an embargo applies.

I retain all other ownership rights to the copyright of my work. I also retain the right to use in future works (such as articles or books) all or part of my work. I understand that I am free to register the copyright to my work.

REVIEW, APPROVAL AND ACCEPTANCE

The document mentioned above has been reviewed and accepted by the student's advisor, on behalf of the advisory committee, and by the Director of Graduate Studies (DGS), on behalf of the program; we verify that this is the final, approved version of the student's thesis including all changes required by the advisory committee. The undersigned agree to abide by the statements above.

Neha Nehru, Student

Dr. J. Todd Hastings, Major Professor

Dr. Cai-Cheng Lu, Director of Graduate Studies

REFERENCE COMPENSATION FOR LOCALIZED SURFACE-PLASMON RESONANCE SENSORS

DISSERTATION

A dissertation submitted in partial fulfillment of the requirements for the degree of Doctor of Philosophy in the College of Engineering at the University of Kentucky

By

Neha Nehru

Lexington, Kentucky

Director: Dr. J. Todd Hastings,

Associate professor of Electrical and Computer Engineering

Lexington, Kentucky 2014

ABSTRACT OF DISSERTATION

REFERENCE COMPENSATION FOR
LOCALIZED SURFACE-PLASMON RESONANCE SENSORS

Noble metal nanoparticles supporting localized surface plasmon resonances (LSPR) have been extensively investigated for label free detection of various biological and chemical interactions. When compared to other optical sensing techniques, LSPR sensors offer label-free detection of biomolecular interactions in localized sensing volume solutions. However, these sensors also suffer from a major disadvantage – LSPR sensors remain highly susceptible to interference because they respond to both solution refractive index change and non-specific binding as well as specific binding of the target analyte. These interactions can severely compromise the measurement of the target analyte in a complex unknown media and hence limit the applicability and impact of the sensor. In spite of the extensive amount of work done in this field, there has been a clear absence of efforts to make LSPR sensors immune to interfering effects. The work presented in this document investigates, both experimentally and numerically, dual- and tri-mode LSPR sensors that utilize the multiple surface plasmon modes of gold nanostructures to distinguish target analyte from interfering bulk and non-specific binding effects. Finally, a series of biosensing experiments are performed to examine various regeneration assays for LSPR sensors built on indium tin oxide coated glass substrate.

KEYWORDS: Localized Surface Plasmon Resonance, Biosensor, Optical sensing, Plasmonics, Interference Compensation

Author's Signature: Neha Nehru

Date: March 10, 2014

REFERENCE COMPENSATION FOR LOCALIZED SURFACE-PLASMON RESONANCE SENSORS

By

Neha Nehru

Director of Dissertation: Dr. J. Todd Hastings

Director of Graduate Studies: Dr. Cai-Cheng Lu

Date: March 10, 2014

ACKNOWLEDGEMENTS

First and foremost, I'd like to thank my advisor Dr. Todd Hastings for his insightful guidance, immense support and unwavering trust throughout the course of this project. No amount of thanks can show my appreciation for his constant encouragement and positive attitude that helped me persevere when things got tough. I would also like to express my appreciation to Dr. Wei, Dr. Singh and Dr. Chen for being a part of my advisory committee and helping me through the various stages of research work. I'd also like to acknowledge National Science Foundation (NSF) for funding my research.

This work would not have been possible without the assistance and encouragement of my colleagues both in and outside of the lab. Brian Wajdyk provided me the training and assistance to work with the instruments in CeNSE. Dr. Gazi Huda helped me get started on the simulation work for my project. Working besides him and Dr. Carlos Jarro everyday made this journey all the more enjoyable. Dr. Eugene Donev helped me develop my first optical setup and taught me to be a better researcher. I would also like to thank Dr. Matt Bresin for always lending a sympathetic ear when I needed to vent about my thesis. I would like to thank Dr. Wei and her graduate students, Dr. Linliang Yu and Dr. Cui Ye, for helping me with the biosensing experiments. I would like to acknowledge Dr. Yugu Yang for being a great friend and colleague, and sharing all the frustrations of life in grad school.

I am also very grateful to have a huge support of extended family and friends, all across the US and India, that have helped me at each and every step of the way. To

Pallavi for been a wonderful friend and a pillar of support throughout this journey. To Carole and Wayne Gnatuk for always being generous with your hospitality, love and support. Thank you for making me a part of your family. To Sid for helping me out with all the last minute proofreading. Finally, I would like to express my gratitude to my parents for their love and support throughout the course of my PhD. You helped me get started on this path, and have been with me every step of the way. Thank you for making this journey possible.

TABLE OF CONTENTS

LIST OF TABLES

LIST OF FIGURES

Chapter 1

Introduction to Plasmonics

The use of gold nanoparticles dates back to as early as 5th century B. C. when it was mostly employed to make beautiful stained glass panels. Michael Faraday, in 1857, was the first to discover metal colloids and attribute the ruby color in glass to dispersed gold colloidal particles [1]. However, it was not until 1908 that Gustav Mie proposed a mathematical explanation for the color of gold colloidal solution [2]. He formulated equations to calculate the scattering and absorption by spherical particles dispersed in a dielectric media as function of its size. Even though Mie theory came about in the early 20th century, significant interest in the optical properties of nanostructures only started to develop over the last several decades. This can largely be attributed to technological advancements that enabled a better understanding of the physical and chemical concepts behind this field. For example, invention of nanofabrication techniques like electron beam lithography, nanosphere lithography, nanoimprint lithography, etc. allowed researchers to design and manipulate complex nanoscale structures. Similarly, advancements in optical technologies including the invention of high intensity light sources as well as high precision data acquisition systems allowed scientists to study the properties of nanoscale structures. Finally, emergence in computational analysis tools helped researchers further explore the basic physics behind this phenomenon.

This evolution in the area of nanoplasmonics and nanotechnology has impacted a wide array of fields, ranging from microscopy and lithography to biological sensing, medicine

and energy [3]. For applications in biochemical sensing, plasmon resonance based nanostructures have been widely studied as a label-free sensing platform. The following sections provide an overview of the basic principle behind plasmonics as well as an introduction to sensing based on localized surface plasmon resonance (LSPR) based nanostructures.

1.1 Basic Principle

A plasmon is defined as the collective oscillation of conduction electrons within materials whose electrons are bound weakly to its lattice ions and are free to move around. Metals and some heavily doped semiconductors are examples of elements that support plasmon oscillations. Bulk plasmons are longitudinal charge density oscillations that are free to propagate within the volume of the metal. For an ideal metal whose dielectric function can be described using the free electron Drude formula,

$$\varepsilon(\omega) = 1 - \frac{\omega_p^2}{\omega^2 + i\gamma\omega} \tag{1.1}$$

where γ is the damping constant due to electron collisions and ω_p is the bulk plasmon frequency defined as-

$$\omega_p = \sqrt{\frac{Ne^2}{m_e \varepsilon_0}} \tag{1.2}$$

Here N is the free electron charge density of the metal, e and m_e are the electron charge and mass respectively and ε_0 is the permittivity of free space (8.854 x 10^{-12} F/m). Equation (1.1) suggests that the bulk plasmon resonance (ω_p) for most metals (assuming minimal damping) occurs at frequencies where its dielectric constant $\varepsilon(\omega) = 0$. It is clear from (1.2) that ω_p depends solely on the free electron density of the material. The

plasmon frequency of metals usually lies in the ultraviolet (UV) regime of the electromagnetic spectrum due to the large values of electron density (N ~10^{28} m^{-3}) [4, 5] Table 1.1 shows the bulk plasmon frequency of some common metals [6]. Due to its longitudinal nature, bulk plasmons cannot be excited by the transverse mode electromagnetic wave. Nevertheless, bulk plasmon can be observed via electron energy loss spectroscopy (EELS).

Surface plasmons are coherent oscillation of electrons confined at the surface between a metal and dielectric. Surface plasmons interact with light to form coupled waves called surface plasmon polaritons (SPP) that propagate along the length of the metal. Figure 1.1(b) displays the schematic of an SPP wave. The electric field of the SPP wave is strongest at the interface and decays evanescently in both the metal and the dielectric. The rate of decay of the SPP wave is higher inside the metal region as opposed to the dielectric region. However, due to its smaller wavelength, SPPs can only be optically excited using special configurations to match the momentum of surface plasmons with that of the incident photons. One of the most widely used methods, shown in Figure 1.1(c), involves using a prism to match the phase of the incoming wave with that of the SP wave [7]. The SP dispersion relation can be derived by solving the wave equation (Helmholtz equation) for an interface between two materials with appropriate boundary conditions [8]. The following equation gives the dispersion relation for an SPP wave

$$k_{sp} = \frac{\omega}{c}\sqrt{\frac{\varepsilon_m \varepsilon_d}{\varepsilon_m + \varepsilon_d}} \tag{1.3}$$

where ε_m is the complex dielectric constant of the metal, ε_d is the dielectric constants of the surrounding dielectric layer, c is the speed of light in vacuum and ω is the frequency

of the incident light. A complete and detailed electromagnetic analysis of SPPs can be found in [9].

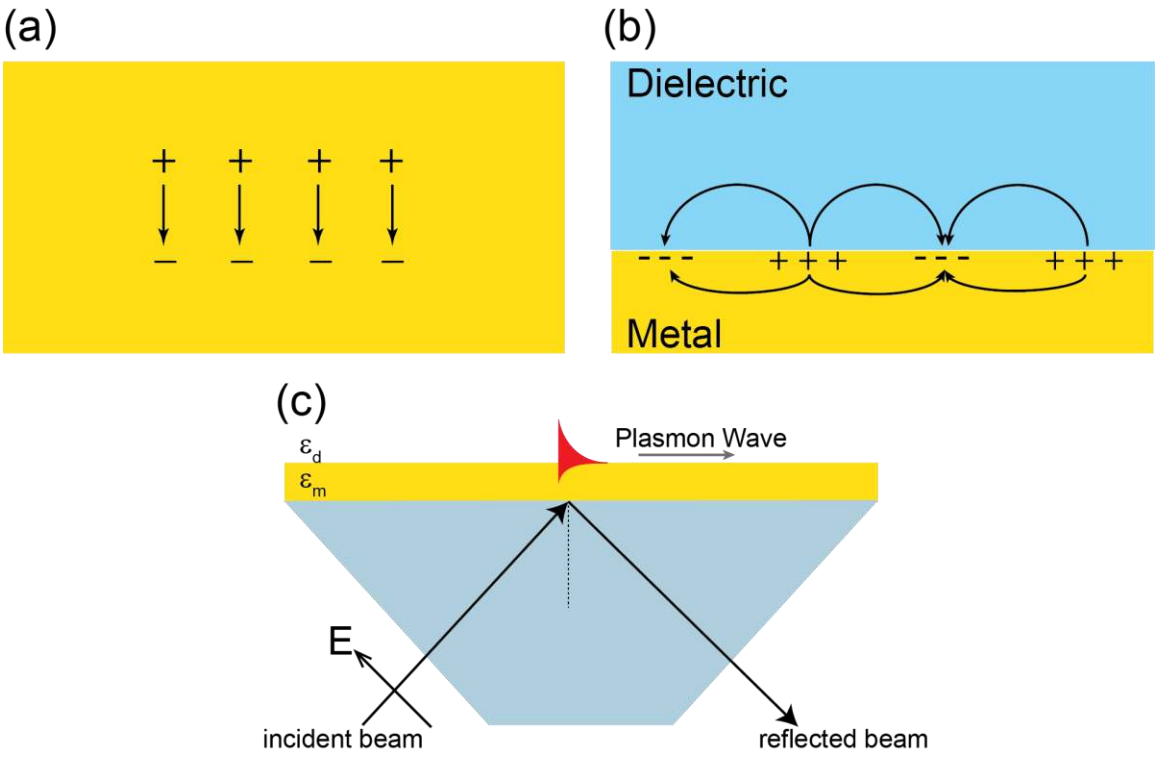

Figure 1.1 (a) Plasmon in bulk metal, (b) Schematic of propagating surface plasmon wave and (c) excitation of SPP wave at the metal-dielectric interface via prism coupling.

Table 1.1 Free electron density and bulk plasmon wavelengths of common metals. Adapted from [6].

Metal	N ($\times 10^{28}$ m^{-3})	λ_p (nm)
Au	5.90	138
Ag	5.86	138
Cu	8.47	115

In comparison to surface plasmon polaritons, localized surface plasmons (LSP) are non-propagating modes that exist in structures with sizes comparable to the wavelength of light. LSPs can be easily excited in nanostructures through direct light illumination without the use of any special configurations such as prisms or gratings. When illuminated, the incident electric field exerts a force resulting in displacement of the conduction electrons inside the nanoparticle with respect to the lattice, as demonstrated in Figure 1.2(a). The attraction between the positive lattice ions and the electrons acts as an effective restoring force causing the electrons to move back to its equilibrium position. The frequency of incident light that closely matches to the natural frequency of oscillation of the electrons inside the nanoparticle leads to resonance. This resonance is defined as the localized surface plasmon resonance (LSPR) of the nanoparticle. Localized surface plasmon resonance leads to two very important effects – strong absorption and scattering of the incident light at LSP frequencies as well as strongly enhanced electric fields near the nanoparticle surface [10]. Figure 1.2 illustrates the two effects for an 85 nm gold nanoparticle suspended in vacuum.

1.2 Calculation of Surface Plasmons in Nanoparticles

The optical properties of nanostructures are governed by the solution of Maxwell's equations for the interaction of particles with electromagnetic wave, under appropriate boundary conditions. This section provides a summary of the different methods used for calculating the optical properties of metallic nanoscale structures.

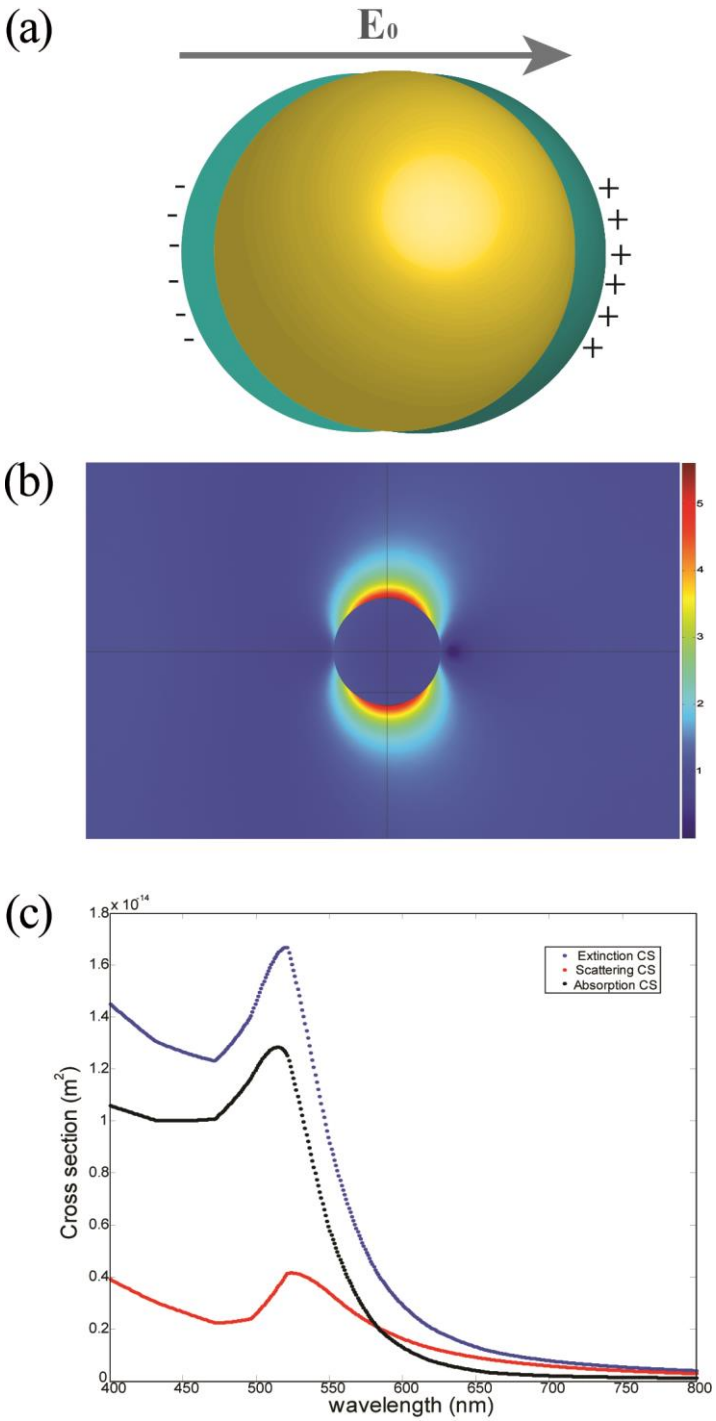

Figure 1.2 (a) Schematic of LSPR, (b) Normalized E field around 85nm Au NP surface at LSPR wavelength and (c) enhanced absorption and scattering cross-section for the same NP at LSPR wavelength.

1.2.1 Electrostatic Approximation

Electrostatic approximation provides a compact analysis of localized surface plasmon resonance in nanoparticles with sizes much smaller than the wavelength of incident light. In such cases, the LSPR as well as the optical properties of the nanoparticle can be easily derived by approximating the nanoparticle with an electric dipole. Figure 1.3 illustrates the case in which light with electric field E_0 is incident on a spherical nanoparticle of diameter d, such that $d<<\lambda$. As seen in the figure, the electric field can be considered uniform inside the nanoparticle (neglecting spatial retardation) causing the conduction electrons to respond simultaneously and move in phase to each other.

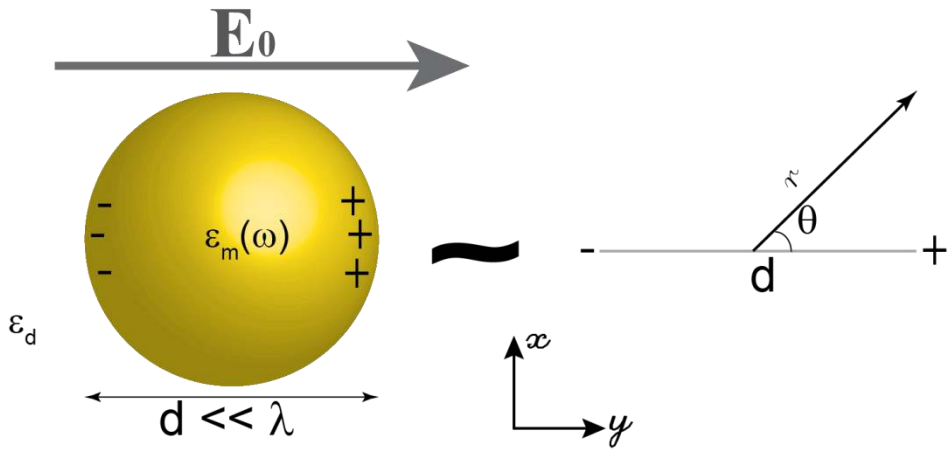

Figure 1.3 E-field and charge distribution for a metal nanoparticle in quasistatic approximation.

The solution for the electric field inside and outside the nanoparticle for the electrostatic case can be calculated by solving the Laplace equation with appropriate boundary conditions [5, 11, 12]. Assuming a uniform incident electric field $\mathbf{E_0} = E_0\hat{y}$,

the quasi-static solution for the electromagnetic field inside and outside the sphere is given by –

$$E_{in} = E_0 \frac{3\varepsilon_d}{\varepsilon_m + 2\varepsilon_d}$$
$$E_{out} = E_0 \hat{y} + \frac{\varepsilon_m - \varepsilon_d}{\varepsilon_m + 2\varepsilon_d} \frac{a^3}{r^3} E_0 (2cos\theta . \hat{r} + sin\theta . \hat{\theta}) \quad (1.4)$$

Here ε_m and ε_d represent the dielectric constant of the sphere and the surrounding medium, a is the radius of sphere (d=2a), E_0 is the magnitude of the incident electric field and θ is the angle between the position vector r and the y-axis. It is clear from the above equation that the electric fields near the particle will be strongest when the denominator, $\varepsilon_m + 2\varepsilon_d$, is minimum. In case of metals with a frequency dependent complex dielectric function, the above condition can be written as –

$$Re\left(\varepsilon_m(\omega)\right) = -2\varepsilon_d \quad (1.5)$$

Here *Re* denotes the real part of the dielectric function. The frequency (or wavelength) value for which the above condition, also known as the *Fröhlich condition*, is satisfied corresponds to the localized surface plasmon resonance of the metal nanoparticle. Substituting this condition in the free electron Drude model (assuming negligible damping) for a metal described in (1.1), the localized surface plasmon resonance (LSPR) frequency for a small sized spherical metal nanoparticle can be reduced to –

$$\omega_{spr} = \sqrt{\frac{\omega_p^2}{1 + 2\varepsilon_d}} \quad (1.6)$$

where ω_p is the bulk plasmon frequency described in (1.2). This equation also describes the relationship of the plasmon resonance of the metal nanoparticle to its surrounding environment (ε_d.) This is an important property of the localized surface plasmons as it

allows metal nanoparticles to be used as sensors for various chemical and biological applications [13, 14]. This will be discussed in greater detail in section 1.4.

Going back to (1.4), one can conclude that the electric fields both inside and outside the particle are resonantly enhanced at the at the LSPR frequency, i.e., when $\varepsilon_m = -2\varepsilon_d$. Furthermore, E-field inside the particle (E_{in}) is uniform for spheres with $d \ll \lambda$ (no spatial dependence) and the electric fields outside the sphere (E_{out}) decays at the rate of $1/r^3$ from the nanoparticle surface.

As illustrated in Figure 1.3, a metal nanoparticle in the presence of a uniform time-varying electric field can be approximated as a dipole consisting of two point charges separated by a distance d. The dipole moment induced by the external field can be calculated as –

$$p = \varepsilon_d \alpha \mathbf{E_0} \tag{1.7}$$

where the polarizability α is defined as –

$$\alpha = 4\pi a^3 \frac{\varepsilon_m - \varepsilon_d}{\varepsilon_m + 2\varepsilon_d} \tag{1.8}$$

Here a is the radius of the sphere ($d=2a$). Using the polarizability of the sphere, we can now define the optical (absorption, scattering and extinction) cross-sections as [12]-

$$C_{abs} = k_0 Im(\alpha)$$

$$C_{sca} = \frac{k_0^4}{6\pi}|\alpha|^2 \tag{1.9}$$

$$C_{ext} = C_{abs} + C_{sca}$$

where k_0 is the wavenumber of light in vacuum. The product of the extinction cross-section and the incident intensity corresponds to the total loss of power from the incident beam due to absorption and scattering from the nanoparticle. C_{ext} can also be thought of

as the geometric area of an ideal opaque particle with the same extinction characteristics as the metal nanoparticle. Certain key observations can be made from the above set of equations. First, both the scattering and the absorption cross-section depend on the polarizability and hence, the LSPR frequency of the sphere. Therefore, the extinction, scattering and absorption cross-sections are strongest at the localized plasmon frequency (ω_{spr}). Second, it is clear from the equations that the absorption scales with a^3 and scattering with a^6. Therefore, extinction cross-section (C_{ext}) is dominated by absorption for small sized nanoparticles and scattering for larger particles. Figure 1.4 further illustrates the point by displaying the extinction, absorption and scattering cross-sections of two gold nanoparticles of size 50nm and 200nm respectively.

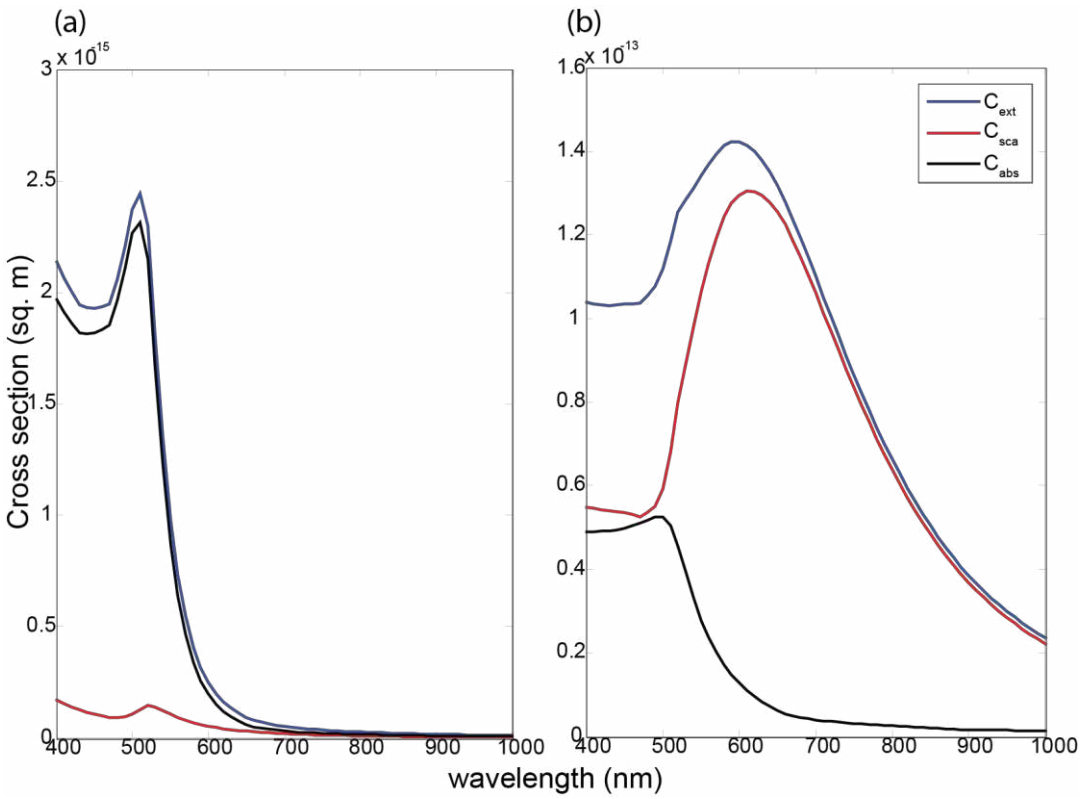

Figure 1.4 Absorption, scattering and extinction cross-section spectra of (a) 50nm and (b) 200nm diameter gold nanoparticle suspended in vacuum.

1.2.2 Mie theory

The electrostatic approximation theory discussed until now only works for particles smaller than the wavelength of light, where a fair assumption can be made that the particle experiences a uniform electric field. This conjecture becomes invalid as the particle size increases and can no longer be approximated as a dipole. For such cases, there exists a classical electrodynamic model that can be utilized to compute the optical properties of spherical nanoparticles of arbitrary size.

Mie theory, developed in 1908 by Gustav Mie, provides an exact analytic solution to Maxwell's equations for the interaction of light with a single isotropic homogenous spherical nanoparticle suspended in a uniform media under appropriate boundary conditions [2]. The solution can be expressed in terms of the extinction, scattering and absorption cross-sections of the nanoparticle. The extinction cross-section for a spherical nanoparticle calculated using *Mie theory* can be expressed as[12, 15] –

$$C_{ext} = \frac{2\pi}{|k^2|} \sum_{L=1}^{\infty} (2L+1)\mathrm{Re}[a_L + b_L] \tag{1.10}$$

$$a_L = \frac{m\psi_L(mx)\psi_L'(x) - \psi_L'(mx)\psi_L(x)}{m\psi_L(mx)\eta_L'(x) - \psi_L'(mx)\eta_L(x)}$$
$$b_L = \frac{\psi_L(mx)\psi_L'(x) - m\psi_L'(mx)\psi_L(x)}{\psi_L(mx)\eta_L'(x) - m\psi_L'(mx)\eta_L(x)} \tag{1.11}$$

where a_L and b_L are the scattering coefficients described in terms of *Riccati – Bessel* functions(ψ_L and η_L), k is the wave vector of incident light in the medium, $x = |k|a$ represents the size parameter with a being the radius of the sphere, $m = n_m/n_d$ where n_m

and n_d are the refractive indices of the nanoparticle and the surrounding media respectively. The summation index L defines the order of plasmon oscillations. Figure 1.5(a) displays the surface charge distribution for L=1, 2 and 3 modes representing the dipole, quadrupole and octupole mode for a spherical nanoparticle.

A complete electrodynamic solution for the extinction cross-section defined in (1.10) consists of a series of multipole resonances leading to several peaks in the LSPR spectra. Figure 1.5 also shows the extinction spectra for 60 nm and 140 nm silver nanoparticles suspended in vacuum. For nanoparticles with sizes smaller than the wavelength of incident light, i.e., $a << \lambda$, the higher order modes (L >1) are not very significant and hence can be ignored. In such cases Mie theory reduces to the electrostatic approximation theory described previously.

1.2.3 Numerical Methods

As explained above, Mie theory provides a complete analytic solution to Maxwell's equations for a spherical, homogenous, isotropic and non-magnetic particle in a non-absorbing media. Nevertheless, there are plenty of practical real world cases for which no analytic solution exists. Some examples include complex arbitrary shaped structures like triangular prisms [16, 17], stars [18, 19], cubes [20] and core-shell nanoparticles [21] or non-homogenous surroundings like particles on a substrate [22]. However, there has been an emergence of powerful numerical analysis techniques that can be utilized to solve for scattering properties of nanostructures in such cases. Some of the widely used methods include Finite Element Method (FEM) [23], Finite Difference Time Domain (FDTD) [24] and Discrete Dipole Approximation (DDA) [25]. Each technique holds several advantages and disadvantages over the others and the use of a particular technique is

highly dependent on the problem at hand. A qualitative analysis of some of the widely used numerical techniques can be found in various journal articles including papers by Zhao *et al.* and Parsons *et al.* [26, 27]. Most of the techniques rely on a similar basic principle of discretization or meshing of the problem domain into smaller cells and solving for the fields inside each cell. The size and shape of the cell is vital to the convergence and accuracy of the numerical solution. For an accurate depiction of the propagation of light the cell size is kept smaller than the wavelength of light in the target. Efficient utilization of the method requires a complete knowledge of both the electromagnetic problem and the numerical technique being used to solve it.

Finite Element Method or FEM is one of the widely used computational analysis techniques used for electromagnetic analysis in the areas of near-field optics and plasmonics to solve for light interaction with irregular geometries. FEM method solves for the electromagnetic scattering problem in frequency domain by discretizing the volume of the simulation domain into small 3D elements like tetrahedra and triangular prisms, depending on what best describes the geometry of the scatterer [28]. The simulation domain is truncated by a bounding box and the electromagnetic field values are calculated at the nodes and the edges of the discretized elements. This technique is especially useful for simulating large domains containing very fine details. Further details regarding the finite element method and the computational software used to implement it can be found in Chapter 5.

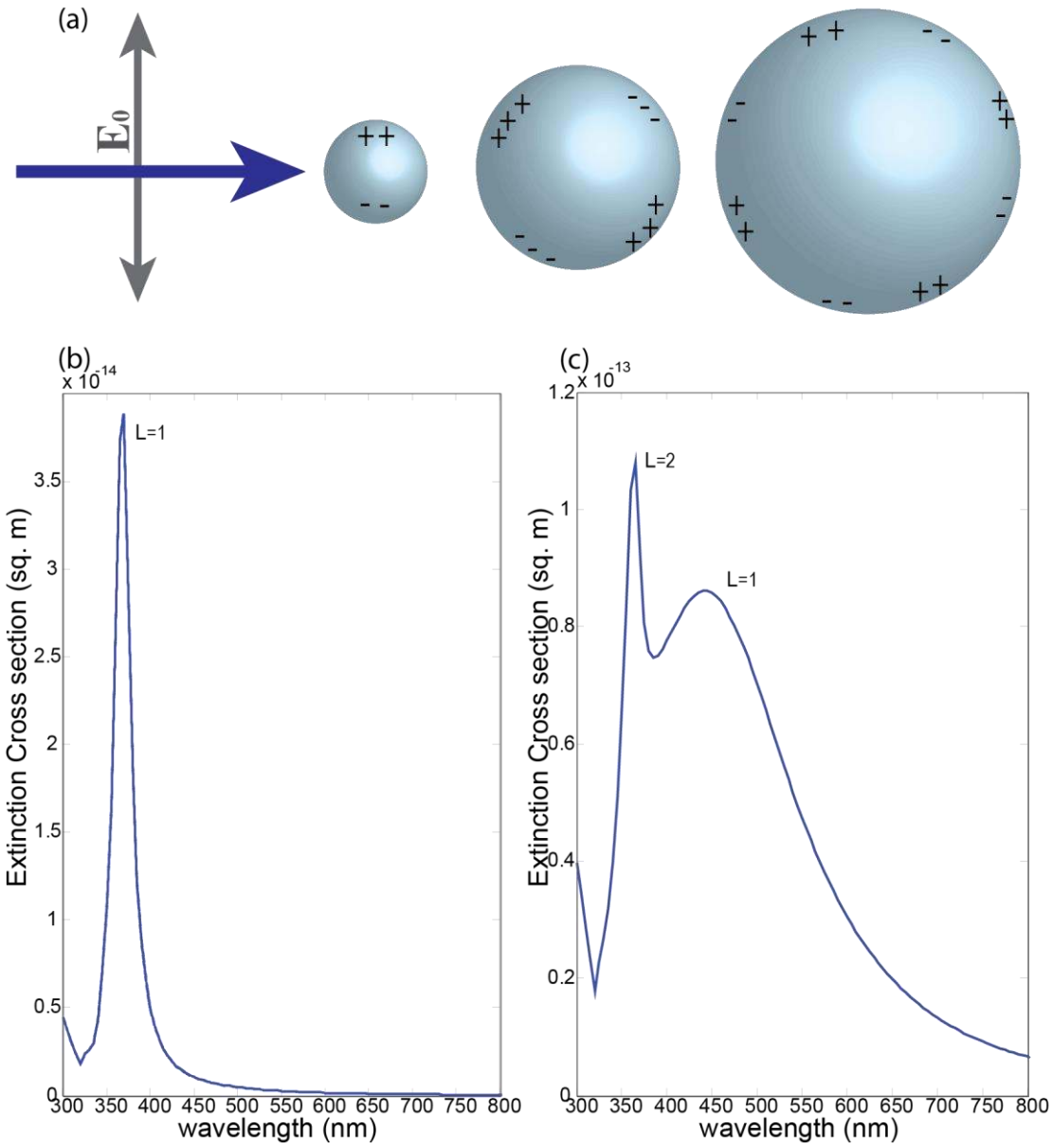

Figure 1.5 (a) Charge distribution (from left to right) for dipole (L=1), quadrupole (L=2) and octupole modes (L=3) for a spherical nanoparticle, and, extinction spectra of (b) 60nm, and (c) 140nm spherical silver nanoparticles in vacuum. The number associated with each peak indicates the order of the multipolar excitation.

1.3 LSPR Characteristics

The spectral position of the localized surface plasmon resonance of metallic nanoparticles depends on many factors including, but not limited to its size, shape and material properties [29]. This section provides a brief overview of the various factors that govern the LSPR wavelength.

1.3.1 Size dependence

The dependence of LSPR wavelength on the size of the nanoparticles can be clearly seen by the size dependence in the scattering and absorption cross-section as defined by the Mie theory. Figure 1.6 displays the dependence of LSPR wavelength to the nanoparticle size. The red-shifting of the plasmon resonance, in most simple terms, can be attributed to the reduction in the restoring force due to increasing distance between the conduction electrons and the positive ions. Further increase in the size of the nanoparticles leads also to higher modes of oscillations as the electrons are no longer able respond homogenously to the applied field due to field retardation across the nanoparticle [30].

In case of nanoparticles that can be classified within the electrostatic approximation, plasmon resonance do not show any appreciable shift with change in size of the nanoparticles [31]. Figure 1.7 shows the shift in the resonance with increasing size of the gold nanoparticles. For particles under 20nm, which defines the dipolar limit for gold, almost no appreciable shift is observed. These nanoparticles, however, show a considerable dependence of the plasmon resonance linewidth to the size of the nanoparticles. As the nanoparticles become smaller than the mean free path of electrons (~40-50 nm for gold and silver), there is an increase in the scattering between the

electrons and the nanoparticle surface. This scattering increases as the size of the nanoparticle decreases. This introduces a size dependence damping term in the Drude formula for the dielectric constant of the metals. This dependence of plasmon resonance within the dipolar approximation is termed as intrinsic (due to the size dependence of the metal dielectric constant) as opposed to the extrinsic effect (beyond the dipolar regime) where the absorption and scattering spectra directly depend on the size of the nanoparticle.

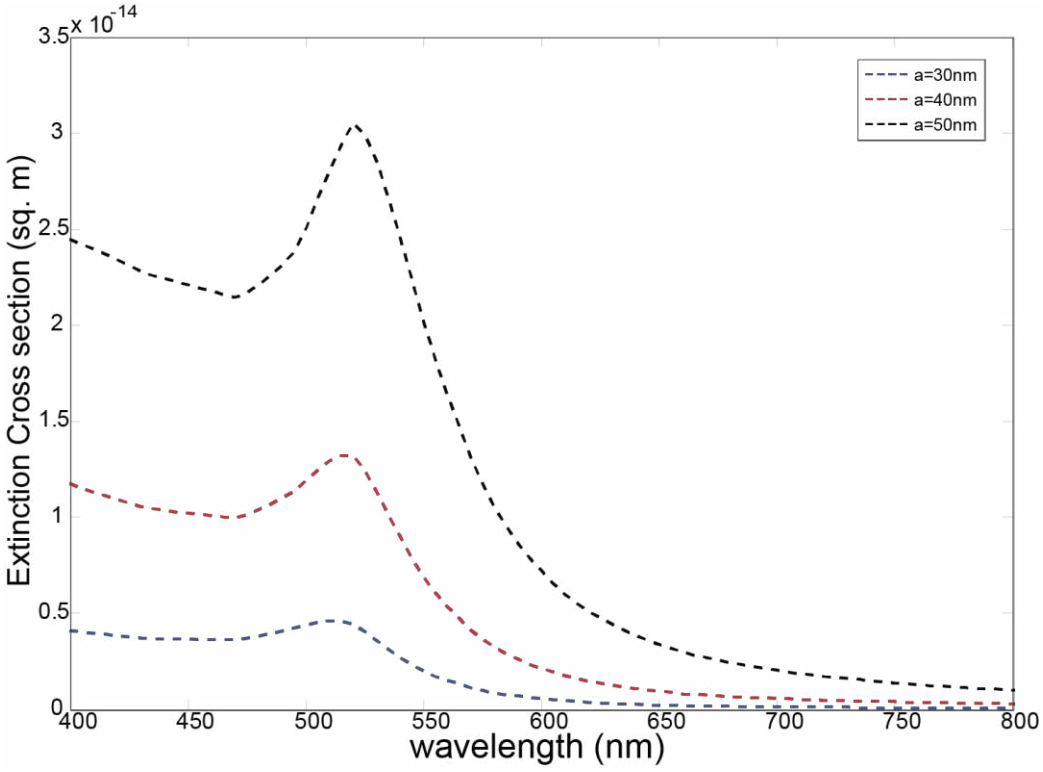

Figure 1.6 Shift in the extinction spectrum with increasing size of spherical gold nanoparticles.

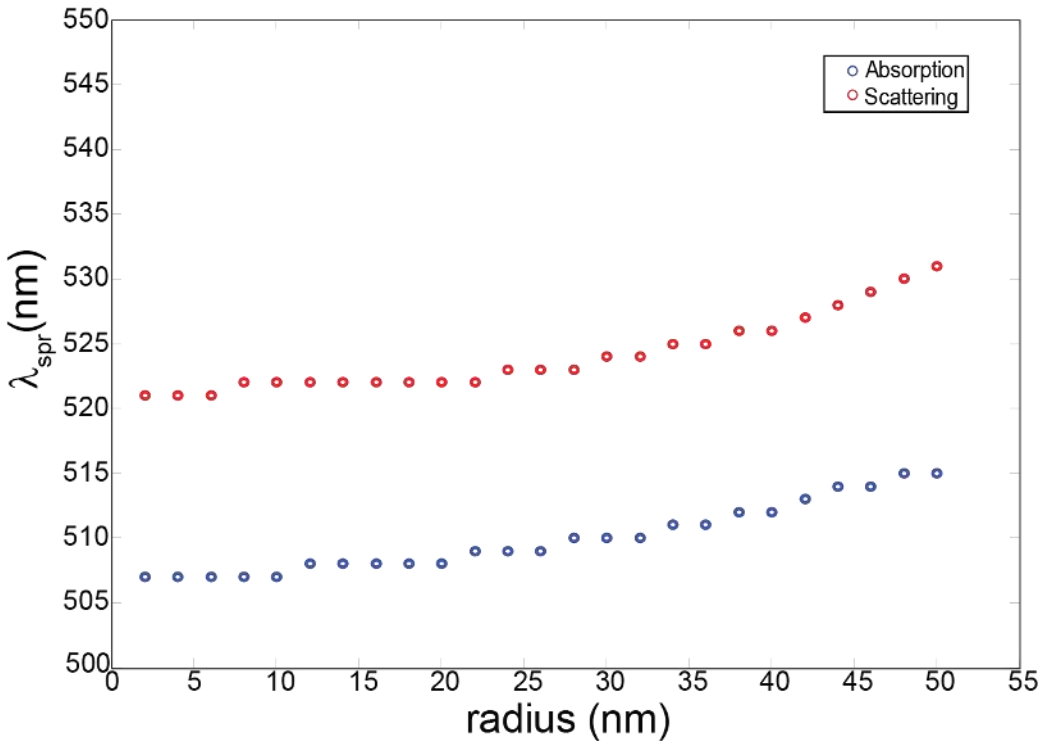

Figure 1.7 Change in the scattering and absorption wavelength with respect to the radius of spherical gold nanoparticle in air.

1.3.2 Shape dependence

Apart from size, localized surface plasmon wavelength is also highly dependent on the shape of the nanostructure. The most common example of this can be seen in the case of rod shaped nanostructures. Nanorods can be approximated as nanoparticles elongated along one of its axis. The elongated shape of the nanorod causes the conduction electrons to oscillate in two different directions depending upon the polarization of the incident light. The resultant resonances are termed as either longitudinal or transverse resonances depending on whether the direction of oscillation is along the long or short axis of the nanorod. Section 3.1.1 provides a more detailed explanation of the plasmon resonances in nanorod based structures.

Besides nanospheres and nanorods, various other nanostructures of different shapes have been designed and fabricated both through colloidal synthesis as well as lithography. The LSP resonance wavelength can be tuned throughout the electromagnetic spectra by fabricating nanostructures of different shapes. Even though nanospheres and nanorods are some of the most widely studied structures, more and more complex structures have been the subject of study in the recent years, thanks to the advances in the fields of computation and fabrication. Figure 1.8 illustrates the optical properties of silver nanostructures of various shapes, ranging from the isotropic spherical particle to the more complex tetrahedral and octahedral shapes. The plot in Figure 1.8 clearly demonstrates that the plasmon resonance wavelength can be easily tuned from the near-UV to near-IR range by just changing the shapes of silver nanoparticles.

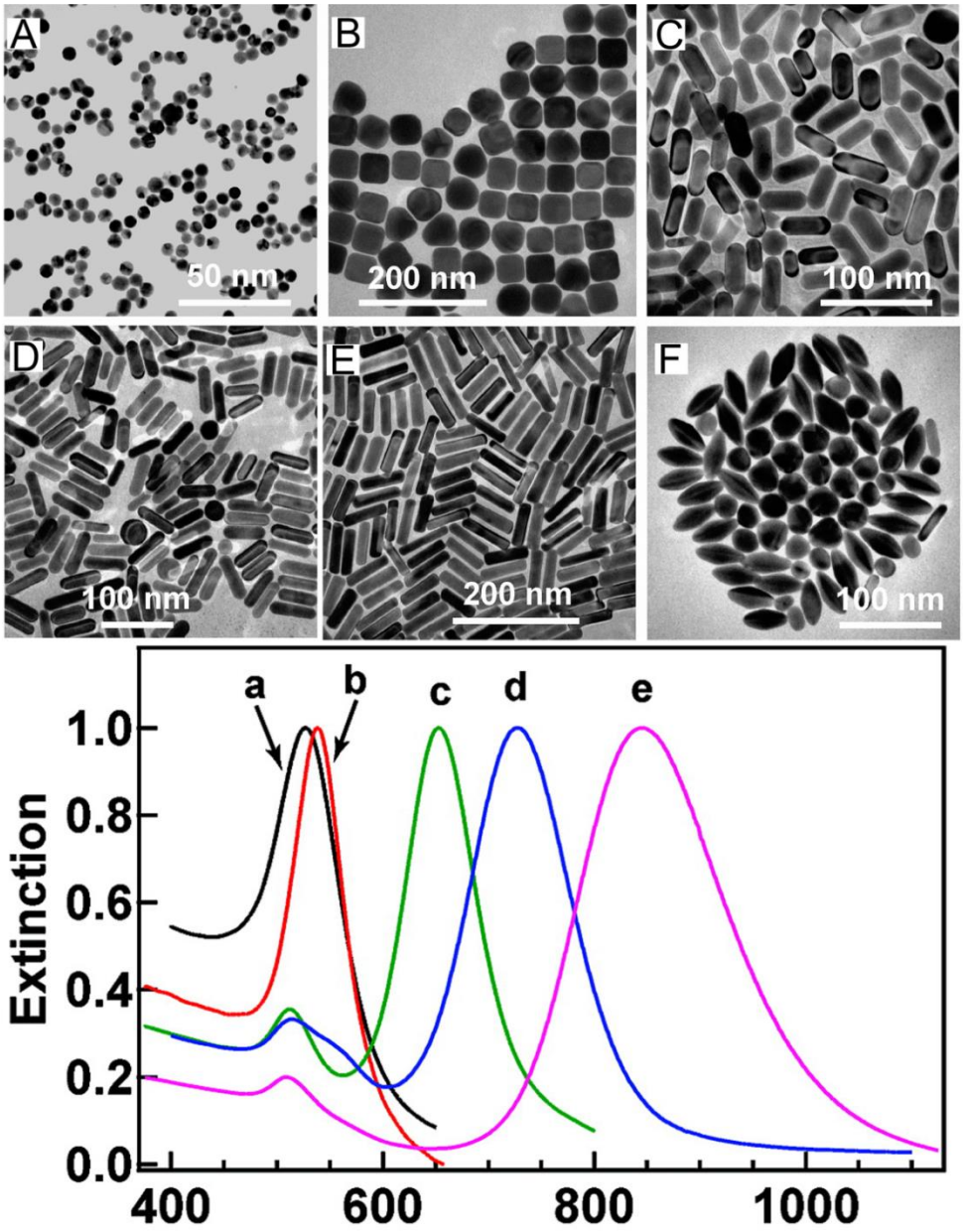

Figure 1.8 (top) TEM images of Au nanostructures of various shapes and sizes. (A) Nanospheres, (B) Nanocubes, (C) Nanorods (AR=2.4), (D) Nanorods (AR=3.4), (E) Nanorods (AR=4.6) and (F) Nanobypyramids (AR=1.5), and (bottom) representative normalized extinction spectra of the above structures (from A-E). Adapted with permission from [32].

1.3.3 Material dependence

As shown in (1.5), the dielectric properties of the nanoparticles also alter its surface plasmon resonance. Nanoparticles with similar shapes and sizes exhibit plasmon resonances at different wavelength positions for different materials. Gold and silver are the two most widely studied materials as their LSPR wavelengths are positioned in the visible region of the electromagnetic spectra, making them easily accessible experimentally. Figure 1.9(b) displays the scattering cross-section of similar sized gold and silver nanoparticles. The differences in the two spectra can be attributed to the different permittivity values of gold and silver. Figure 1.9(a) also displays the real and imaginary dielectric constant values for gold and silver [33]. Differences in the LSPR resonances can be attributed be attributed to dissimilar ε_1 values of gold and silver. The differences in the values of the imaginary part of the dielectric constant, ε_2, affect the plasmon resonance linewidths for gold and silver particles. Lower values of ε_2 results in sharper peaks and higher extinction efficiencies for silver nanostructures as compared to its gold counterpart.

Besides gold and silver, various other materials including metals as well as semiconductors with enough free electrons and negative permittivity have the potential to support LSPR. Copper is one such material that has been studied by various groups as it exhibits comparable imaginary dielectric constants to gold in the visible range [34]. However, it is highly reactive and easily oxidizes in air and therefore, is not used as widely as Au. Similarly, various 'poor metals' like Al, Sn etc. have also been shown to exhibit strong plasmon resonance as well as enhanced electric fields in the near to far UV range [35].

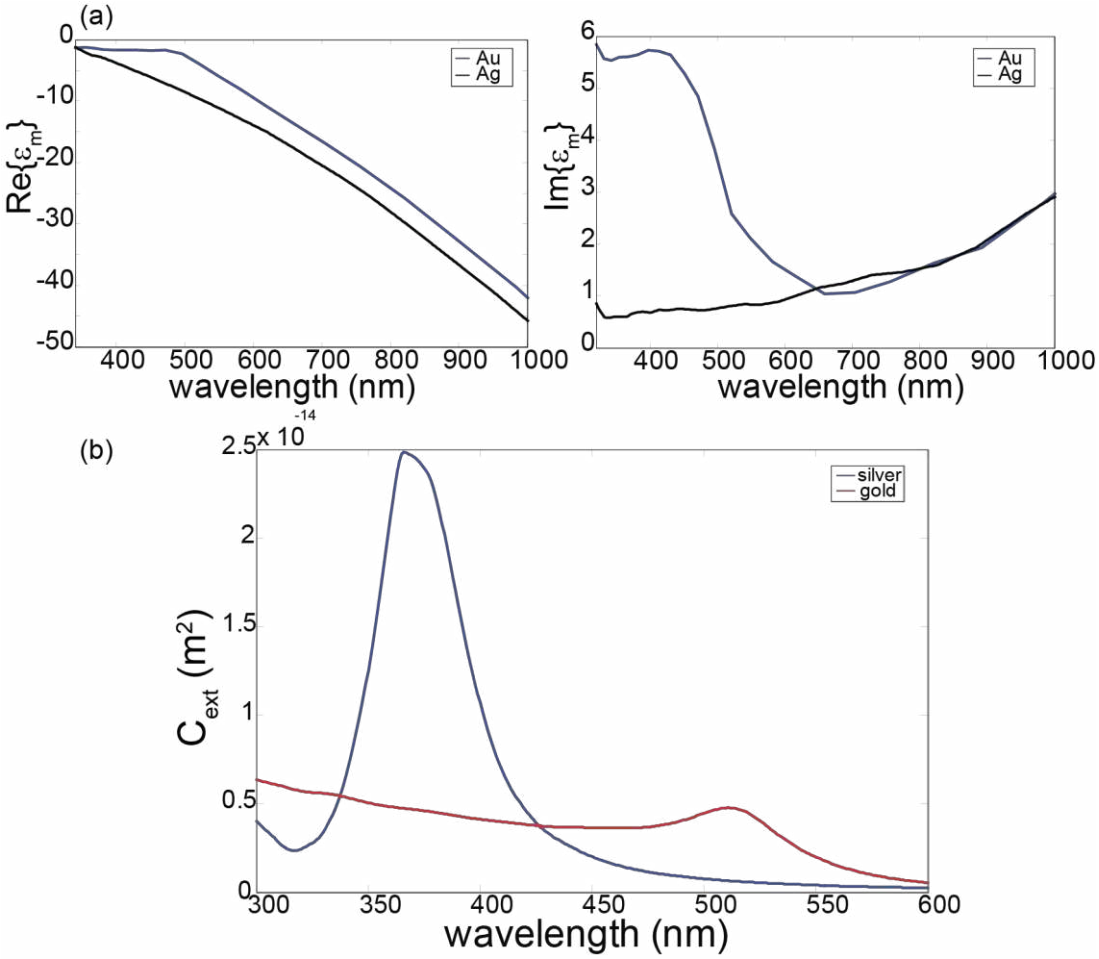

Figure 1.9 Real and imaginary part of the dielectric constant for gold and silver, data adapted with permission from [33] and, (b) Extinction spectra of 60nm gold and silver spherical nanoparticles with air as the surrounding media.

1.3.4 Effect of surrounding media

The LSPR wavelength of the metal nanoparticle, as evidenced in (1.6), is also influenced by the dielectric properties of the surrounding media. The presence of electric field around the nanoparticle surface also induces the polarization of the surrounding medium. This polarized medium compensates for some of the charges on the metal nanoparticle surface resulting in a reduced restoring force. Higher value of ε_d results in smaller

restoring force as more surface charges are compensated by the polarized charges of the surrounding medium. Hence, as seen in Figure 1.10, surface plasmon resonance wavelength red-shifts with increasing permittivity of the surrounding media [3, 36].

The dependence of resonance wavelength position to the dielectric property of the surrounding media is an important property of LSPs as it allows them to be used as sensors for various biological and chemical applications. The use of LSP based metal nanostructures as sensors is one of the most widely utilized applications of such structures [13, 37, 38]. More details regarding LSPR based sensors will be discussed in the following section.

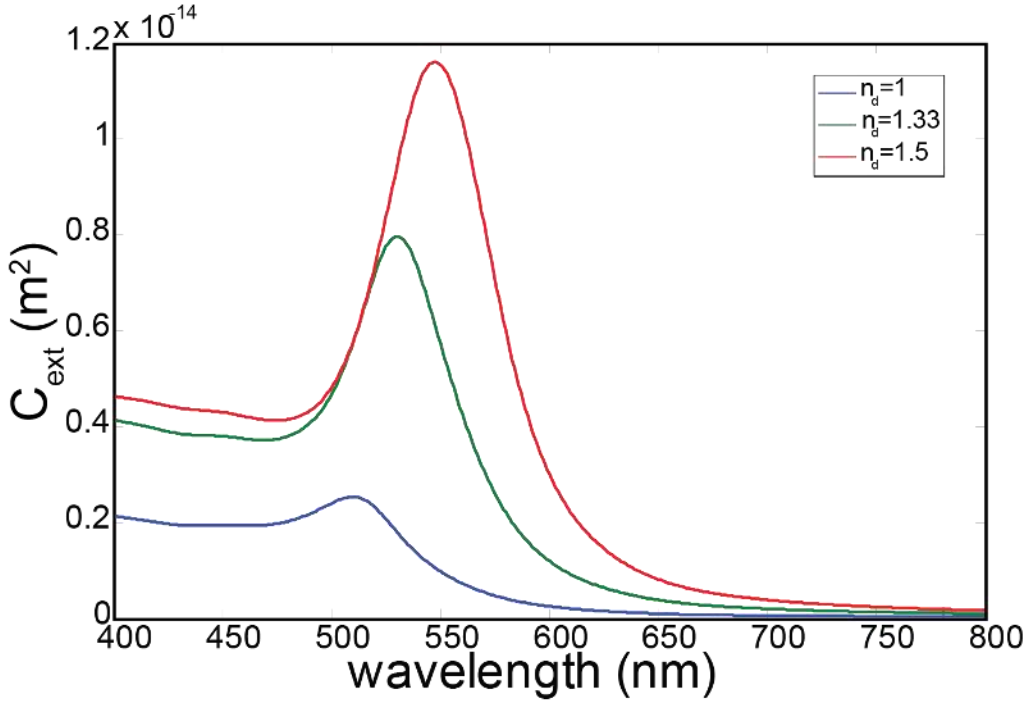

Figure 1.10 Extinction cross-section of a 50nm gold nanoparticle embedded in various media.

1.4 LSPR nanostructures as optical sensors

The unique optical properties of nanostructures exhibiting surface plasmons have been utilized in a wide range of applications. Some examples of fields where LSPR has been applied include drug delivery [39], cell labeling for identification of tumors *in-vivo* [40] and *in-vitro*[41, 42], biochemical sensing, nanolithography, nanophotonic devices [43], solar cells [44, 45] and optical trapping [46].

The use of metal nanostructures as sensors is one of the most important applications of LSPR. The first ever LSPR based sensor, demonstrated by Englebienne in 1998, utilized the shift in plasmon resonance of colloidal gold nanoparticle in solution to detect analyte-ligand binding interactions [47]. Since then, LSPR based optical sensors have been employed in areas ranging from disease diagnosis [48] to food safety and environmental toxins [49]. This area has witnessed tremendous growth in the past decade, mainly due to the advancements in the field of nanoscale fabrication and synthesis along with improvement in optical characterization tools.

The fundamental mechanism involving LSPR sensing can be understood by returning to (1.6) which defines the resonance frequency for a quasistatic approximated spherical nanoparticle. Converting from ω_{spr} to λ_{spr}, we can rewrite the equation as –

$$\lambda_{spr} = \lambda_p \sqrt{1 + 2\varepsilon_d} \tag{1.12}$$

where λ_p corresponds to the bulk plasma wavelength of the metal ($\lambda_p = 2\pi c/\omega_p$) and ε_d is the dielectric constant of the surrounding medium. Equation (1.12) clearly shows that the plasmon resonance wavelength position for a metal nanoparticle is directly proportional to the permittivity or the refractive index, n_d of the surrounding medium (where $n_d = \sqrt{\varepsilon_d}$). Therefore, as illustrated in Figure 1.10, a change in the refractive index

of the environment can be directly measured from the shift in the absorption or scattering spectra of the nanoparticles. This section summarizes the different characteristics used for measuring and comparing the performance of LSPR sensors.

1.4.1 Performance Characteristics

Sensitivity is one of the main performance characteristics of an LSPR sensor. It can be classified as bulk or surface sensitivity depending on the type of quantity being measured. Bulk sensitivity, expressed in nm/RIU where RIU denotes refractive index units is defined as the change in resonance wavelength due to the change in refractive index of the bulk solution surrounding all or a part of the nanoparticle. Mathematically, it can be expressed as –

$$S_B = \frac{\Delta\lambda_{spr}}{\Delta n_B} \tag{1.13}$$

where Δn_B and $\Delta\lambda_{spr}$ represent the shift in the refractive index of the surrounding medium and the change in the resonance wavelength it induces. S_B values for a sensor have been shown to be highly dependent on the nanoparticle morphology. Chen *et al* showed that the bulk refractive index sensitivity values for gold LSPR based sensors can change from 44 nm/RIU for a 15 nm spherical nanoparticle (λ_{spr}=527nm) to 703 nm/RIU for more complex star-shaped structures with λ_{spr} in the near-IR range [32]. Table 1.2 gives the bulk sensitivity values for some of the more complex nanoparticle shapes. Miller *et al.* showed through simulations that, irrespective of its type, the RI sensitivity of an LSPR sensor is highly dependent on the resonance wavelength position, increasing as it shifts to higher wavelengths [50]. However, this dependence of bulk sensitivity on the spectral position of plasmon wavelength is valid only for cases in which λ_{spr} occurs in the region

where ε_1 varies linearly with wavelength. The bulk sensitivities of LSPR based sensors are orders of magnitude lower than that of propagating surface plasmon resonance based sensors (S_B ~ 10^4 nm/RIU for a thin gold film sensor) [51]. This could be attributed to the larger decay length of SPP as compared to its LSPR counterpart as well as the closely matched dispersion dependence of SPP to the prism used for its excitation. Thus, a small change in refractive index requires a large change in wavelength to retain the phase matching conditions for SPP sensors. For LSPR sensors a small change in wavelength is sufficient to match the change in resonance condition because the condition depends primarily on the dispersion of the metal.

Besides sensitivity, figure of merit (FOM) is also widely used to characterize sensor's performance. It was established in order to compare performances of various LSPR based sensors irrespective of their shapes and sizes [20]. The figure of merit of an LSPR sensor is governed by its sensitivity and resonance linewidth, and is calculated as follows–

$$FOM = \frac{S_B}{FWHM} \tag{1.14}$$

where *FWHM* (full width at half maximum) denotes the resonance linewidth. LSPR sensors with high figures of merit are indicative of good sensors that are capable of resolving very small bulk RI changes. Kvasnička *et al* [52] suggested another formulation that incorporated the metal permittivity to calculate the bulk FOM for a sensor -

$$FOM = \frac{2n_d}{\varepsilon_m''(\lambda_{sp})} \tag{1.15}$$

The above equation suggests that metal nanostructures with low losses at its resonance frequency possess a higher FOM. This is understandable as higher imaginary dielectric constant values (as discussed in Section 1.3.3) result in broader plasmon resonance

linewidths. Hence Ag nanoparticle sensors, due to Ag's smaller imaginary ε_m, exhibit higher figures of merit as compared to their Au counterparts. FOM also decreases with increasing plasmon resonance wavelength of the nanoscale metal sensor. As shown in Figure 1.11(a) by Otte *et al.* [53], an increase in nanoparticle size leads to radiation damping and broader resonance linewidths (FWHM) resulting in reduced FOM.. Various authors have proposed solutions to reduce radiative damping at longer λ_{spr} through techniques like fano resonances in complex structures [54-57]. Similarly, a single nanoparticle based sensor gives sharper linewidths as compared to a sensor based on an ensemble of nanoparticles. Figure 1.11(b) illustrates this by comparing the LSPR wavelength of a single triangular silver nanoprism versus an array of such structures [17]. Table 1.1 displays the FOM values of some of the complex shaped LSPR sensors found in literature.

Surface sensitivity is employed when LSPR sensors are used for the detection of biomolecular interactions occurring close to the nanoparticle surface. Surface sensitivity can be defined as –

$$S_B = \frac{\Delta\lambda_{spr}}{\Delta d} \tag{1.16}$$

where Δd denotes the change in thickness due to the adsorption of the molecular layer. The binding of molecules to the surface of a nanostructure results in a measurable shift in its LSPR wavelength. In many cases, Δd is replaced by ΔC indicating the change in surface coverage due to adsorption of the molecules. This shift is induced due to the interaction between the target molecule and the localized E-fields around the nanoparticle surface. The sensor surface is usually coated with a recognition element to improve its selectivity and allows strong binding to the target molecules in solution. Besides the

thickness of the target molecule, the magnitude of shift observed in an LSPR sensor also depends on the refractive index and the thickness of the recognition element. The response of an LSPR sensor functionalized with sensing elements of thickness d_{func} to protein binding can be estimated using the following equation [58] -

$$\Delta\lambda_{sp} = S_B \Delta n e^{-\frac{2d_{func}}{l_d}}\left(1 - e^{-\frac{2d_{analyte}}{l_d}}\right) \tag{1.17}$$

where ℓ_{d} is the decay length of the electric field surrounding the nanoparticle, d_{analyte} is the thickness of the analyte layer and Δn is the refractive index difference between the surrounding dielectric and the target molecules. Various studies have been conducted to experimentally investigate the distance dependence of LSPR nanostructures by attaching different length SAM molecules onto the sensor surface. Malinsky *et al.* [59] reported that the plasmon resonance of Ag nanoparticles on glass substrate red-shifted linearly for addition of every methylene group present in an alkanethiol chain $CH_3(CH_2)_xSH$ of varying length with x spanning from 3-15. The authors also measured bulk RI sensitivity of the Ag nanoparticles before and after the binding of SAM molecule and observed a 20% reduction in S_{B}. In a similar manner, Haes *et al.* [60] investigated the long range distance dependence of resonance wavelength and concluded that the shift due to target molecules depends on the nanoparticle composition including its size, shape and material. Figure 1.11(c) shows the shift dependence for both Ag and Au nanoparticles of same sizes with different analyte thicknesses. Ag nanoparticles were found to give larger shifts compared to Au nanoparticles for the same adsorbate thickness. Au nanoparticles were also found to saturate at smaller layer thickness (~17nm) as compared to Ag (~26nm); demonstrating weaker electric fields surrounding the gold particles compared to its silver counterpart. The size of functionalization layer also affects the overall response of the

sensor to the target protein binding. In case of larger recognition element, the protein will bind farther away from the nanoparticle surface; inducing a much smaller shift due to the exponentially decaying electric fields, than if the recognition element were smaller. This was verified experimentally by Fuez *et al.* [61] where they utilized two different sized functionalization layers, thiol-PEG-biotin (polyethylene glycol) and disulphide-OEG-biotin (olego-ethylene glycol), and measured the sensor response to neutravidin binding. Hence, type of functionalized element being used plays a very important part in sensor design as it greatly affects the selectivity as well sensitivity of the biomolecular interaction to be detected.

Limit of detection (LOD) is another sensor characteristic widely reported in literature. It defines the smallest change in sensing parameter (bulk refractive index or surface coverage) that can be detected by the sensor. It is often expressed mathematically as-

$$LOD = \frac{3\sigma}{S} \tag{1.18}$$

where S can be either the bulk or surface sensitivity and σ calculates the standard deviation of the measured parameter. Apart from the shape of the sensor's spectra (i.e., its width and position), σ also depends on other experimental parameters including the type of light source and the detector being used.

Lastly, another term used when discussing sensor's performance is the dynamic range. It is defined as the range between the highest and the lowest possible concentration that can be reported accurately by the sensor. The sensor is usually limited by its LOD at low measurement levels. At the high levels, the sensor is limited by saturation, which could happen, for e.g., due to the use of all binding sites in a functionalized LSPR biosensor [9].

Table 1.2 Bulk sensitivities as well as figures of merit of several complex shaped LSPR nanostructures found in literature.

Shape	Size	λ_{spr} (?)	S_B (nm/RIU)	$\mathcal{FOM}$	References
Gold nanorings. Colloidal lihtography on glass, ensemble msmt	150 nm diameter	~1.3 μm	880	2	[62]
Gold nanorice with Fe_2O_3 core on glass	340nm by 54nm LxD	1160nm (long. Wavelength)	800 (longitudinal sensitivity)	N/A	[63]
Gold-silica nanoshells on glass	r_1 = 102nm r_2 = 122nm internal, external radius	N/A	555	N/A	[64]
Single Ag triangular nanoprism	111nm edge length, 15nm snip	630 nm	205	3.3 (in terms of eV, ev RIU^{-1}/ ev)	[17]
Single Au nanorod on glass	50nm by 15nm LxD	~660 nm	170	1.3	[65]
Silver nanostar	69.5nm edge length with 30° vertex angle	~700 nm	625	9.5	[66]

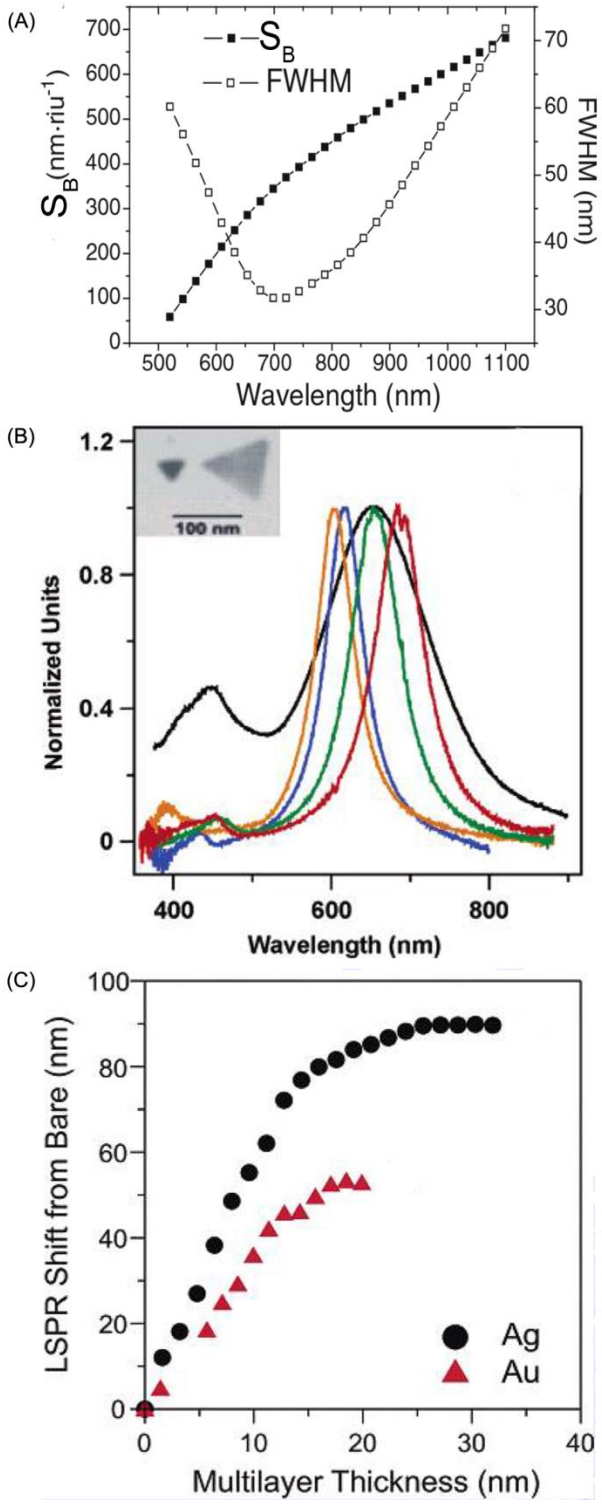

Figure 1.11 (A) Bulk sensitivity and FOM for ellipsoidal Au nanoparticles of different AR calculated, (B) Normalized ensemble (black) vs single nanoparticle (colored) scattering spectra of silver triangular nanoprisms, and (C) LSPR shift with respect to layer thickness for Ag and Au elliptical nanoparticles of size 70nm by 50nm. Reprinted with permission from [17, 53, 60].

To summarize, this chapter gave an overview of the physics behind localized surface plasmon resonance as well as its use as optical sensors. Significant strides in the field of nanotechnology have allowed researchers to explore in detail the field of optical nanosensing using LSPR nanostructures. As a result, its applications can be seen in every possible field including disease diagnosis and therapy. Plasmon resonance based nanostructures have been widely studied as label-free sensors for applications in biochemical sensing. The next chapter provides a literature review of the work done over the past decade in the field of nanoscale optical sensing using LSPR structures.

Chapter 2

Optical Biosensing using LSPR nanostructures

2.1 Introduction

A biosensor is defined as an instrument used for the detection and analysis of various biological and chemical compounds. Vo-Dinh *et al.* [67] described biosensor as a device comprising of a bio-recognition and a transduction element. The bio-recognition element selectively recognizes and interacts with the target analyte to produce an effect that can be transformed into a measurable quantity by the transduction element. Figure 2.1 displays the conceptual diagram of the biosensing principle. Biosensors can be further classified depending on the type of bio-recognition element or transduction mechanism being used. The most common form of bio-recognition element involves the use of specific binding property of antibodies to detect target antigens. Such sensors are commonly referred to as immunosensors or immunoassays.

Based on the different types of transduction signals, a biosensor can be divided into three major categories – mechanical, electrical and optical. Biosensors based on mechanical transduction can be achieved through cantilever based sensors. As seen in Figure 2.2(a), these sensors are made of long thin membranes with one free end, and the other side anchored to a substrate. They are usually made of silicon or silicon based materials and can be fabricated using the well-established micro- and nanofabrication techniques. Cantilever based sensors can be further classified depending on the type of mechanical force being measured. Fritz *et al.* were among the first to utilize silicon based

microcantilever stress sensors to detect DNA hybridization [68]. Arrays of microcantilevers were functionalized with two different ssDNA base sequences – one complimentary to the target being detected and the other to a random sequence, and the difference in the deflection between the two cantilevers was measured. Since then, these sensors have been utilized for the detection and analysis of various biochemical elements including cancer biomarkers like prostate specific antigen (PSA), proteins, pathogens, mRNA molecules, *E.coli* cells and environmental toxins among many others [69-71].

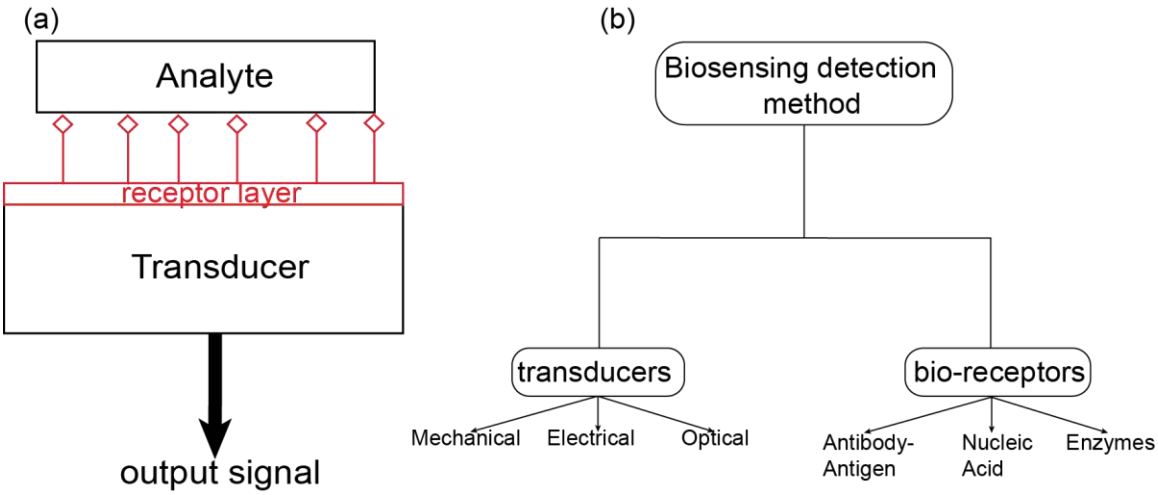

Figure 2.1 (A) Biosensing principle, and (B) Classification of various biosensors based on the type of bio-recognition and transduction element being used.

Electrical or electrochemical biosensors can be categorized based on the type of electrical signal being measured [72]. These could be – amperometric devices, which involve measurement of current resulting from redox reactions on an electrode surface; potentiometric devices, which measure the potential difference or charge accumulation between two electrodes; or conductometric devices that measure changes in conductive properties of a medium. One of the oldest and most successful examples of an electrical sensor involves the measurement of glucose through the amperometric detection of hydrogen peroxide. The sensing device, developed in the 1970s, consisted of an electrode coated with the glucose oxidase (GOx) enzyme that converted glucose (in the presence of oxygen) to gluconic acid, releasing H_2O_2 in the process [73]. Improvement in fabrication techniques have allowed for the development of smaller and more sensitive electrical sensors that can be used for various sensing applications. For e.g., Cui *et al.* [74] reported a nanoscale field effect transistor (FET) based electrical sensor with a functionalized gate for measuring pH changes. As seen in Figure 2.2(b), the sensor measured the shift in conductance due to the protonation or deprotonation of amine groups on its surface. Other applications for electrical biosensors include cancer biomarker detection, DNA hybridization and various other antigen-antibody interactions [75-77].

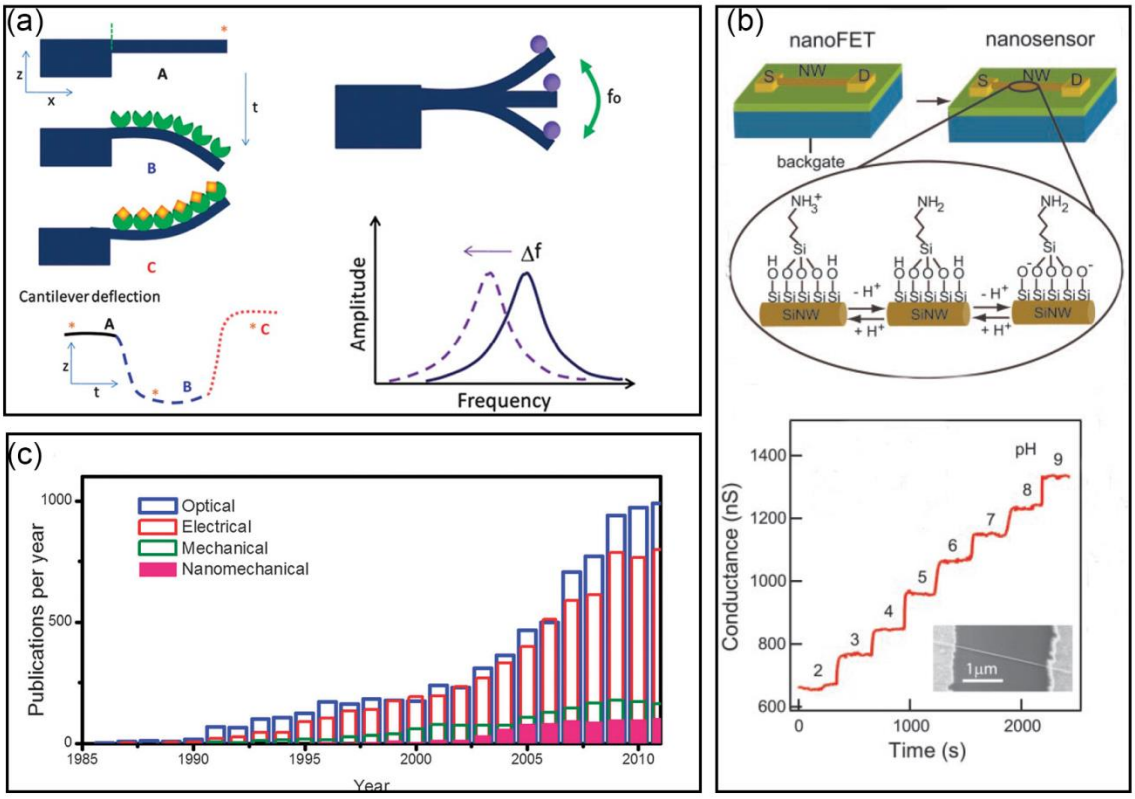

Figure 2.2 (a) Working principle of a cantilever based nanomechanical sensor. The binding of target on one side of the cantilever surface causes a change in the deflection of the cantilever's free end that can be detected through a shift in position. Cantilever sensor on the right measures the change in mass due to the binding of target molecules that is detected through shifts in its resonance frequency. (b) Electrical nanosensor used for the detection of pH changes through shifts in conductance, and (c) Plot showing the number of publications in each of the major sensing techniques over the years. Reprinted with permission from references [70, 74, 78].

2.2 Optical Sensors

Optical sensing involves the detection of biochemical interactions through optical measurements. Binding of target molecules onto the sensor surface functionalized with bio-receptors, can be measured by monitoring changes in its absorption, reflectance, scattering or fluorescence spectra. Advancements in the field of nanofabrication and optical technologies have made optical detection the most widely used biosensing mechanism over the past couple of years. Figure 2.2(c) plots the number of publications in the various fields of biosensing over the last two decades.

Optical sensors can be vaguely classified in terms of label and label-free sensing. Label based optical sensing involves the use of fluorescent, luminescent, enzymatic or radioactive markers to detect the presence of target molecules. These tags may be attached to either the bio-recognition element or the target molecule, and the intensity of fluorescence emission indicates the concentration of target analyte. Another format, called the sandwiched assay technique, involves the use of a fluorophore tagged secondary antibody to bind to the already captured target molecules on the sensor surface [79]. This method requires the use of antigens with atleast two binding sites for the primary and secondary antibody. Figure 2.3 shows the direct and sandwiched assay format used in label based sensors. One of the most widely used biosensor, Enzyme Linked ImmunoSorbent Assay (ELISA) is an example of a label based sandwiched sensing technique. ELISA is an end point immunoassay used for the detection and analysis of antibodies or antigens in a sample [80]. The antigen–antibody binding, one of which is bound to the plate surface, is followed by the addition of an enzyme labeled secondary antibody, forming a sandwiched assay. This enzyme metabolizes the dye

molecule present in the solution resulting in a detectable colorimetric shift. This method is used widely in clinical settings for the purpose of medical diagnostics [81]. Another example of a label based sensor is the commercially available high throughput DNA microarray chips for the determination of unknown sequences of nucleotides. As shown in Figure 2.3(c), the chips are printed with arrays of known short strand DNA sequences and the binding of unknown tagged nucleotides to its complementary strand is observed through fluorescence [82].

Label-free sensors, on the other hand, detect and measure biological and chemical interactions without the use of any labels or tags. One of the ways label free sensors detect analyte interactions involves measuring refractive index changes close to its surface. Some common examples of label-free sensors include photonic crystal based devices [83], optical waveguides based devices [84], ring resonators [85] and surface plasmon resonance based devices [86]. Label-free sensors have attracted considerable attention over the last decade or so due to improvements in the field of micro and nanoscale technology. As a result, these sensors have become smaller as well as more sensitive and robust making them useful for various biological and chemical applications.

As mentioned above, SPR based sensors fall under the category of label free optical sensors. Both propagating and localized SPR sensors detect molecular interactions by monitoring the shifts in plasmon resonance wavelength through its absorption or scattering spectrum [87]. These shifts are proportional to the concentration of target analyte that binds to the sensor surface. The propagating SPR sensor is the more mature technology of the two, having been in existence since 1982 when it was first utilized by Nylander *et al* [88] for the purpose of gas detection. Biacore was the first company to

pioneer commercial SPR devices in the early 1990s. Since then, these devices have been employed in both research and, to a somewhat lesser extent, in clinical settings to study the sensitivity, specificity, concentration as well as to acquire kinetic measurements of various molecular interactions.

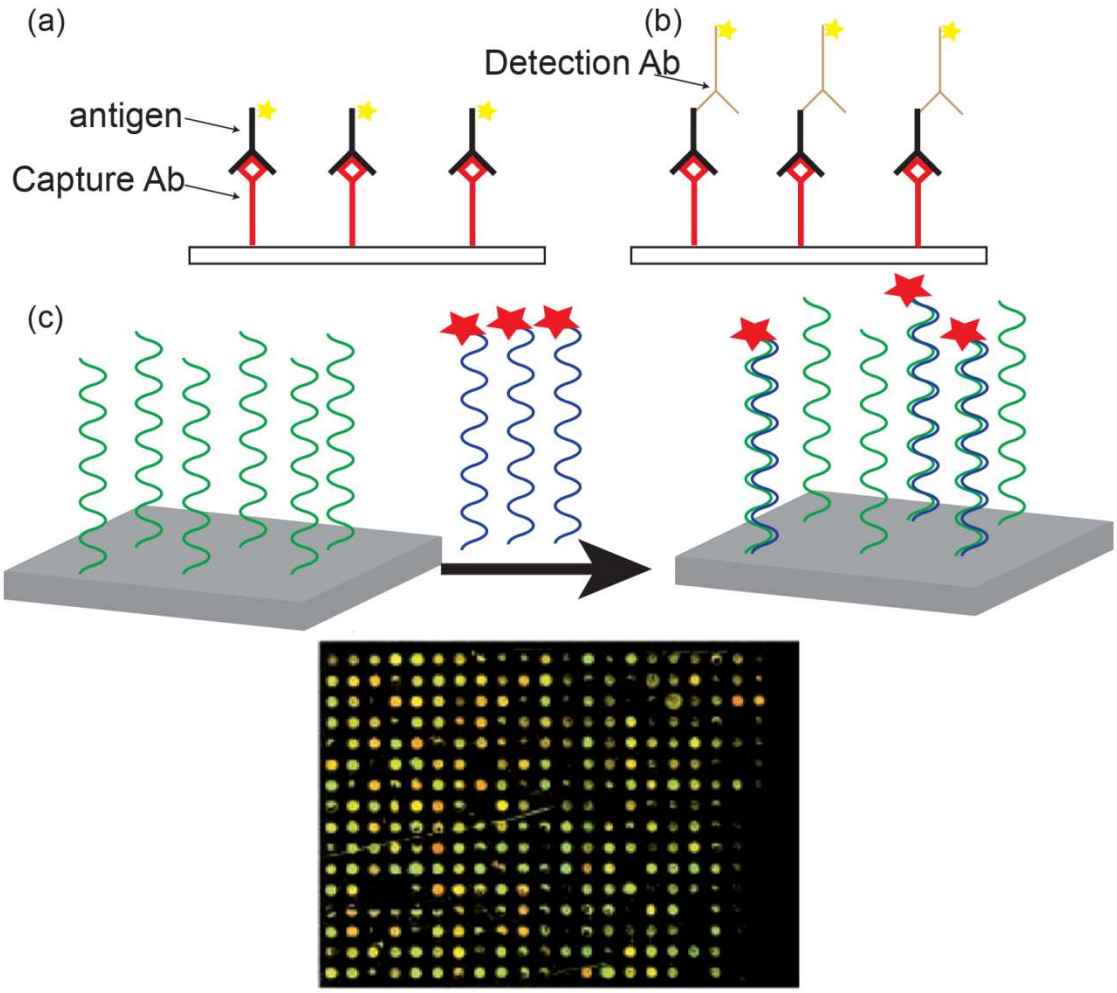

Figure 2.3 Different kinds of immunoassay techniques (a) Direct detection format where the antigen is fluorescently labeled, (b) Sandwiched assay format utilized by ELISA that employs a secondary antibody for the detection of target molecules, and (c) Schematic of the DNA microarray technique. The image at the bottom shows the result obtained from a typical chip. DNA chip reprinted with permission from ref [89].

2.2.1 Comparison between various optical techniques

Both localized and propagating surface plasmon resonance sensors exhibit several attractive properties when compared to other optical sensing techniques. In contrast to ELISA and other label based sensors, sensing using SPR devices allow label-free detection of bio-molecular interactions. Most of the label based methods are endpoint assays techniques that only measure the change in signal before and after the binding. Plasmon resonance based sensors, on the other hand, provide real-time kinetic analysis that can be used to measure the association and dissociation constants of various ligand-analyte binding interactions.

As explained previously, both SPR and LSPR devices are based on the similar technique of detecting small refractive index changes close to the sensor surface. However, in contrast to its propagating counterpart, localized plasmon resonance based sensors offer more strongly enhanced fields with shorter decay lengths allowing the LSPR sensors to exhibit high sensitivity toward molecular binding interactions. This was proven theoretically by Otte *et al* [90] where they compared the bulk surface sensing characteristics of an SPR (50 nm gold layer) and LSPR based sensor (gold nanorods). It was demonstrated that even though the bulk sensitivities and figures of merit were atleast one order of magnitude higher for thin film SPR sensor, the LSPR sensors displayed three times higher surface sensitivities and FOM making it the preferred candidate for bio-molecular sensing applications.

Another difference between the two devices involves the propagating nature of traditional SPR sensors. The extended propagation distance of surface plasmons limits the sensor's size between tens to hundreds of microns [5]. This property of SPR sensors

prevents a true miniaturization of the system that is easily obtainable with an LSPR sensor. The presence of a localized sensing volume allows LSPR devices to work in extremely low solution volumes. Furthermore, localized plasmon sensors offer a great deal of flexibility of design in terms of its size and shape (for e.g., ellipsoids, disks, crescents etc) as compared to its propagating counterpart allowing LSPR sensors to easily tune their resonance wavelength position across the visible to near-IR spectra. Finally, the simple instrumentation required for the excitation and measurement of localized surface plasmons makes it easier to work with, especially as devices in point of care applications.

2.3 Background and Perspective on LSPR sensing

LSPR sensors were first reported in literature by Englebienne in 1998 when he exploited the plasmon properties of gold nanoparticles coated with various monoclonal antibodies to measure its binding affinities to the antigen of interest [47]. Since then, remarkable progress has been made in the field of localized surface plasmons, and LSPR sensors in particular. Besides biological sensing, LSPR sensors have also been used in various other application including environmental sensing and food safety [91-93].

The potential of LSPR sensors to demonstrate improved surface detection parameters as compared to its traditional SPR sensors counterpart has been shown numerically. However, in reality, various experimental factors prohibit the LSPR sensors from reaching their full efficiency. This was shown by Otte and co-workers where they reported a 60% drop in the surface sensitivity and FOMs of a gold nanorod based sensor compared to theoretical calculations [90]. Therefore, the major focus of research in this area has mostly been on improving the surface sensitivities and detection limits of the sensors through various techniques. Higher sensitivities have been achieved by

introducing more complex structures than spherical nanoparticles, with sharper features and more hot spots where the E-field enhancement is orders of magnitude higher at plasmon resonance wavelength. Several groups have tried to improve the detection limits through other means, for e.g., through improvements in detection as well as the data analysis techniques [94]. Others have also looked into improving the detection limits through selective immobilization of antibodies to high sensitive areas on the sensor's surface [95].

Several researchers have focused their efforts on studying biochemical sensing using localized surface plasmon resonance. LSPR based nanostructures, in the past 15 years, have been exploited for various sensing application, including, among various others, detection of disease biomarkers, DNA hybridization detection and protein-protein interaction analysis [96]. Gold and silver are the two most common materials used for designing LSPR biosensors. However, gold has always been the preferred candidate of the two, due to its stability, biocompatibility, easy conjugation to biomolecules and low toxicity to the human body. The unique optical properties of LSPR sensors have rendered them useful as both simple colorimetric sensors as well as refractometric sensors.

Colorimetric sensing is a relatively simple, inexpensive and sensitive method for biological and chemical detection. In this method, shown in Figure 2.4, LSPR nanoparticles aggregate in the presence of target molecules, causing a visible change in color of the solution. The color change is a result of the coupling between plasmon modes of individual nanoparticles in close proximity to one another, causing a shift as well as broadening of its resonance wavelength. Perhaps, one of the most important applications of this mechanism has been for the detection of specific sequences of oligonucleotides.

Mirkin's group were the first to report the observation of DNA hybridization using two different 15 base pair (bp) nucleotide target probes attached to a 13nm gold nanoparticle. Addition of the complementary 30 base nucleotide sequence results in the aggregation of nanoparticles as the two probes attach to their complementary parts of the target, thereby cross-linking the nanoparticles and causing the solution color to change from red to purple [97]. The authors were further able to improve the sensor's selectivity and response time by employing two 5′ and 3′ target probes (12 base) attached to gold nanoparticles [98]. This allowed them to differentiate mismatches, deletions as well as insertions from the complete 24bp complementary target sequences. Similarly, Sato *et al.* [99] reported on a non-cross-linking colorimetric method to determine the presence of complementary nucleotide sequence. They showed that target DNA probes coated gold nanoparticles hybridize to its complementary sequence and at high salt concentration, induces aggregation of the nanoparticle resulting in the change in solution color. This aggregation was not observed in the absence of the target nucleotide. The authors reported faster reaction times (at room temperature) as compared to the cross-linking method reported by Mirkin's group.

Besides DNA hybridization, colorimetric sensing has also been utilized for the detection of various other biochemical interactions. For example, Kang *et al.* [100] have used the non-cross-linked aggregation method to differentiate between normal and cancerous human breast tissues using gold nanoparticles labeled with a cationic protein kinase C (PKC). Similarly, Chen *et al.* [101] developed a colorimetric label-free sensor for the detection of thrombin, an enzyme (serine protease) involved in blood coagulation. Using 56nm gold nanoparticles labeled with fibrinogen as probes, the authors were able

to detect thrombin down to 0.04pM in buffer solution as well as 0.2pM in 10-fold diluted human plasma samples, as compared to nanomolar levels of detection using other nanomaterial and aptamer based detection methods [102]. Apart from nanoparticles, researchers have also looked to other structures for aggregation based sensing. For example, Hirsch *et al.* [103] used gold/silica nanoshells to successfully detect low (sub-nM) concentration of immunoglobulin (IgG) in various media. The authors observed the aggregation of anti-rabbit-IgG coated gold/silica nanoshells within half an hour of adding target rabbit-IgG solution, with a dynamic range from 88ng/mL to 0.8ng/mL. Successful detection of immunoglobulins was also observed in saline, serum as well as 20% whole blood, although with a slight (20%) reduction in the sensitivity of the sensor. Further details summarizing the various designs, methods as well as different applications of colorimetric sensors can be found in review papers by Zhao *et al.* and Vilela *et al.* [104, 105].

LSPR sensors that do not involve aggregation of colloidal nanoparticles to determine the presence of target analyte, may be grouped together as refractometric sensors. Such sensors, as explained in Section 1.4, operate by examining any changes or perturbations in the refractive index close to its surface that occurs when a target molecule binds to its functionalized surface. Figure 2.5 displays the operating principle behind the sensing technique. These sensors may exist either in solution phase or on a substrate. The following section gives a brief overview on some of the most widespread applications of refractometric LSPR based sensors.

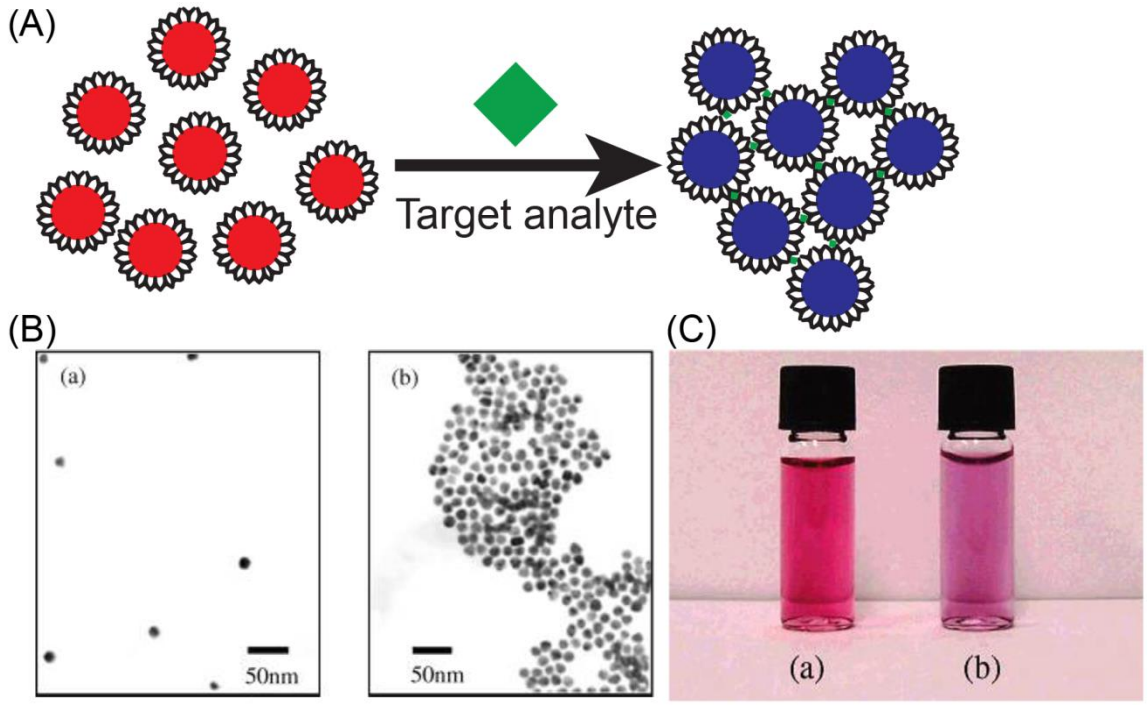

Figure 2.4 Schematic of a colorimetric LSPR sensing technique. (A) The functionalized gold nanoparticles suspended in solution aggregate in the presence of the target molecules causing a change in solution color from red to purple observed in (C), and (B) shows the TEM image of functionalized gold nanoparticles before and after the addition of target molecule (here cholera toxin). Images (B) and (C) reprinted with permission from ref [106].

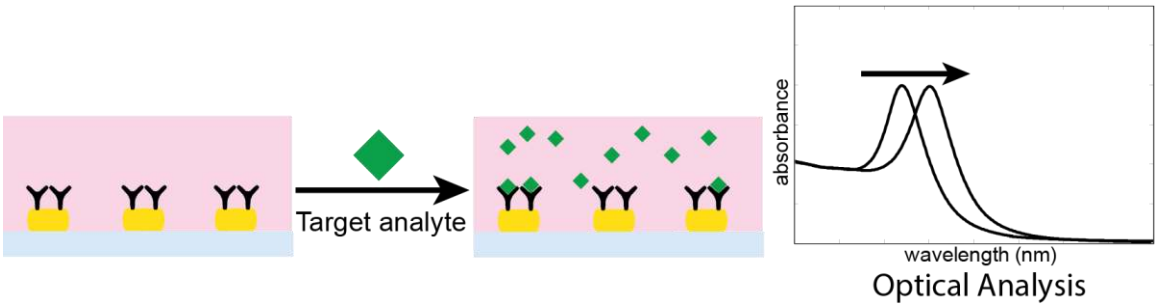

Figure 2.5 Basic principle behind the refractometric LSPR sensing technique. The target molecules in solution bind to the functionalized sensor surface causing a perturbation in the refractive index close to its surface. The refractive index change is easily measured by observing the shifts in the plasmon resonances of the LSPR sensor.

2.3.1 Biotin-streptavidin interaction

Biotin – streptavidin binding is one of the most widely studied immunoassays using LSPR sensors. Due to its small size, biotin can be easily conjugated to metal surfaces without any significant loss in its biological activity. Streptavidin, on the other hand, is a large tetramer molecule (M.W. ~60 kD) that exhibits extremely high binding affinity towards biotin. Due to its high specificity and sensitivity of interaction, biotin-streptavidin is often employed as a model for analyzing the sensor's performance, especially with respect to other LSPR based sensors. For example, Nusz *et al.* used biotin-streptavidin interaction to compare their single gold nanorod based sensor to previously described gold nanoparticle based sensor [107]. The gold nanorods, synthesized in solution, were coated with biotinylated bovine serum albumin (BSA) and immobilized on a glass substrate. The LOD for this system was measured to be 1nM and found to be 1000-times lower than the detection limit for a single Au nanoparticle based affinity biosensor, developed by Raschke *et al.* [14]. Similarly, biotin-streptavidin system was employed by Chilkoti's group to separately study the sensing characteristics of assemblies of gold nanorods as well as nanoparticles adsorbed on a silanized glass substrate. Once again, lower limits of detection were observed for nanorod (94pM) [108] compared to nanoparticle based devices (94nM) [109]. These experiments provided substantial proof that compared to spherical nanoparticles; nanorods exhibit higher sensitivity and LOD.

In addition to nanorods and nanospheres, streptavidin-biotin receptor ligand assay have also been employed to demonstrate sensing performances of other complex nanostructures. For example, Haes *et al.* [110] utilized this system to test the biosensing

capabilities of triangular silver nanoparticles fabricated using nanosphere lithography (NSL) on a glass substrate. The authors estimated the LOD of streptavidin to be less than 1pM using this LSPR sensor. Besides using biotin-streptavidin for testing sensors of different shapes and sizes, it has also been used to show improved sensitivities and detection limits in sensors. For instance, Fredrik Höök's group [95] demonstrated that selective binding of neutravidin (similar to streptavidin) to the highly sensitive areas (i.e., the walls) of Au nanohole based sensor improves its sensitivity as well as allows for a faster detection time as compared to when the entire surface is used for sensing. The same effect was also observed in case of coupled nanoparticles based sensors. Controlled binding of neutravidin to gaps between the gold nanodisks, also referred to as hot spots for the strong localized electric fields observed at these regions, improved the signal obtained per bound molecule by a factor of 4 compared to using single gold nanodisks for binding interactions [61].

2.3.2 Cancer diagnostics

Perhaps one of the more important applications for LSPR biosensors has been in the field of cancer diagnosis. According to the American Cancer Society, roughly 13 million people were diagnosed with cancer worldwide in 2010 [111]. This number is anticipated to increase to more than 20 million by 2020. Therefore, there is a growing need to discover novel ideas and techniques for the prevention, diagnosis and effective treatment of cancer. Researchers, over the past decade, have extensively looked into the field of nanotechnology as an alternative means for the detection and treatment of cancer [112]. Techniques like localized surface plasmon resonance have proven effective in facilitating growth in areas such as diagnosis and treatment of cancer. LSPR nanostructures have

enabled enhanced treatment of cancer; through both targeted drug delivery and photothermal therapy. This technique allows several advantages over the current methods including improved drug delivery through specific targeting of cancerous cells in the body, thereby reducing side-effects. Huang *et al.* [113] and Dreaden *et al.*[114] provide a good review of the various ways LSPR devices are being employed in the area of cancer treatment and therapy.

In addition to therapy, LSPR nanoparticles have been thoroughly studied as biosensors for both in-vitro and in-vivo cancer diagnosis. Low detection limits exhibited using this method makes it an attractive candidate as sensors for early cancer diagnosis. Rapid and early detection is an important parameter to consider when exploring new methods for cancer screening, as early detection greatly improves the patient's prognosis. LSPR sensors provide a simple, rapid and sensitive method to detect cancer biomarkers in low solution volumes. It can be used for detecting any kind of cancer, provided the appropriate biomarker as well as its specific antibody is available.

Table 2.1 provides an overview of the LSPR biosensors utilized for the detection of various cancer biomarkers. LSPR nanostructures of various shapes and sizes have been employed for the ultra-sensitive and label-free detection of various cancer biomarkers including breast, prostate and lung. The detection limits obtained through this method are far better than some of the commercially available techniques. For e.g., the nanorod based sensor developed by Sim and co-workers [115] utilize single particle spectroscopy as well as improved surface immobilization procedures to detect extremely low concentrations (~1aM) of prostate specific antigen (PSA), a biomarker used in the screening of prostate cancer.

Table 2.1 Summary of various nanoparticle based LSPR sensors in literature used for the detection of different kinds of cancer antigens.

Particle/Type	Cancer type	Biomarker	LOD	Reference
Au nanorod Single	Prostate	PSA (Prostate Specific Antigen)	111 aM	Truong *et al.*[116]
Au nanorod Single	Prostate	PSA	1 aM	Truong *et al.*[115]
Au nanoparticle Single	Prostate	PSA	0.1 pg/mL	Cao *et al.* [117]
Ag nanotriangles Ensemble	Head &Neck squamous cell carcinoma	p53 protein		Zhou *et al.*[42]
Ag nanotriangles Ensemble	Ovarian	HE4 (Human Epididymis secretory protein 4)	4 pM	Yuan *et al.*[118]
Au nanorods & nanoparticles Ensemble	Breast	CCL2 (chemokine ligand 2)	0.099 μg/mL	Roche *et al.*[119]
Au nanoparticles	Head &Neck squamous cell carcinoma, colorectal, gastrointestinal, prostate	IL-6 (interleukin-6)	10 pg/mL	Munge *et al.* [120]
Au oval shaped nanoparticles Ensemble	Breast	SK-BR-3 cell lines	100 cells/mL	Lu *et al.*[121]
Hollow Au nanospheres	Lung	CEA (Carcinoembryonic Antigen)	1 pg/mL	Chon *et al.* [122]
Hollow Au nanospheres	Breast	HER2 (Human epidermal growth factor)	N/A	Lee *et al.* [123]

2.3.3 Other bio-molecular examples

Besides its application in cancer diagnosis, LSPR sensors have also been employed for the sensitive detection of various other diseases and viruses. Van Duyne and co-workers [124] reported using NSL fabricated triangular silver nanoparticles on a glass substrate as biosensors for the possible detection of Alzheimer's. The sensor surface was functionalized using ADDL (Amyloid β-derived diffusible ligands), a potential biomarker known to exist in elevated forms in autopsied patients brain samples, and then exposed to varying concentrations of anti-ADDL antibody while recording changes in the extinction spectra. The authors also reported on increased effect of non-specific binding at low concentrations (~10mM) of anti-ADDL due to the presence of the underlying Cr layer that was used to improve adhesion between silver and glass. Another group, in 2008, described an LSPR sensor for the selective and sensitive detection of tau protein, another biomarker for Alzheimer's disease, using a '*multi-spot nanoparticle*' chip [125]. The sensor comprised of chrome and gold thermally evaporated on the glass substrate. This was followed by addition of silica nanoparticles on its surface and a final evaporation of a thin gold film over the particles surface. This robust and reproducible fabrication technique was developed to simulate the formation of gold-silica core-shell nanoparticle monolayer on the substrate, thereby circumventing any complicated chemistry associated with depositing monolayer of colloidal core-shell particles. The detection limit for the sensor was reported to be as low as 10 pg/mL.

Similarly, Lai *et al.* [126] utilized LSPR sensor for the detection of micro-albuminuria, a monomeric protein, which can help identify patients at high risk for cardiovascular events. Unlike other commercially available methods (e.g., high performance liquid

chromatography (HPLC)) that are time-consuming and labor intensive, LSPR technique offers a simple, rapid and label-free method for urinary albumin detection in clinical environment. Triangular Ag nanoparticle, fabricated using NSL, and functionalized with anti-albumin antibodies (10 μg/mL) were used as sensing device. Urine samples, taken from pre-eclampsia patients, were diluted by a factor of 1000 with PBS before using the samples for LSPR analysis. Using this device, the authors reported a dynamic range from 1ng/ml to 1μg/ml for albumin proteins in PBS solution.

LSPR nanosensors have also been exploited for the highly sensitive detection of HIV-1 virus with a detection limit as low as 200 fg/mL [127]. Like cancer, rapid detection of HIV is important for the long term well-being of the patient. The sensor consisted of Au nanodots fabricated on an ITO coated glass substrate through electrochemical deposition with monoclonal HIV-1 antibodies coupled to its surface through gold-thiol interaction. The specific binding of HIV-1 virus like particles to the sensor surface was monitored through absorbance measurements. Compared to conventional methods of detection for HIV-1 virus, LSPR sensors are highly sensitive, require almost zero preprocessing steps and low sample volume solutions. The authors also compared it to an angular SPR setup using Au surface and found it to less sensitive compared to LSPR sensor (LOD ~ 25pg/mL). Besides HIV virus, LSPR sensors have also been used for the detection of various other diseases. For e.g., Wang *et al.* [128] utilized the longitudinal mode of colloidal gold nanorods for the detection of Hepatitis B (HB). The HB antibodies were directly adsorbed onto the gold surface followed by the addition of BSA to block any active sites. The LOD for HB antigens using the sensor was measured to be 0.01 IU/mL with a dynamic range extending from 0.01 to 1 IU/mL.

The various examples mentioned above provide an overview of the different applications of an LSPR based sensor. Majority of research being done in this field investigates ways and means to improve LSPR sensors in terms of its sensitivity or detection limits. Despite the progress made in this area, far less work has been done in tackling the problem of non-specific interference prevalent outside laboratory environments. Biological samples, e.g., serum and plasma samples, consist of molecules other than the target molecule of interest that can potentially interact with the sensor surface, resulting in inaccurate concentration measurements of target molecule. Therefore, interference compensation is essential for use of LSPR sensors in clinical settings. The following chapters provide a brief review of the interference compensation schemes employed by various groups as well as demonstrate, both numerically and experimentally, our research effort in developing multi-mode LSPR sensors to distinguish target analytes from various non-specific interferences.

Chapter 3

Differentiating Surface and Bulk Interactions using Dual Mode Sensor

3.1 Background

Localized surface plasmon resonance based sensors for applications in biochemical interactions have been widely studied over the past decade. Due to its enhanced electric field profile at plasmon resonance as well as its ability to provide a kinetic response, LSPR sensors have been employed majorly for the detection of antibody-antigen interactions. However, the major challenges faced by LSPR sensors, that also plague any immunoassay based biosensor, involve its susceptibility to various interference interactions.

The fundamental sensing mechanism of surface plasmon based sensors, as mentioned in previous chapters, involve measuring refractive index changes due to the binding of target molecules on their functionalized surface. This change in refractive index is directly measured from the shift in the resonance wavelength in their absorption or scattering spectra [87]. This technique possesses several advantages over the widely used and commercially available propagating surface plasmon resonance sensors, including greater field enhancement at the metal surface, significantly reduced sensing volumes and extensive resonance wavelength tunability [60, 129, 130].

In spite of all their advantages, LSPR sensors suffer from the same problems inherent in immunosensors that detect target analyte in solution by measuring localized refractive index changes close to the sensor's surface [131]. In particular, these sensors cannot

distinguish specific target interactions from non-specific interfering effects. These effects include variations in the solution refractive index and non-specific binding between the sensor and non-target molecules. These interactions can compromise the measurement of the target analyte in a complex unknown media and hence limit the applicability and impact of LSPR sensors.

Various groups have investigated techniques to compensate for interfering interactions in propagating SPR sensors. For example, Homola *et al.* [132] developed a dual-channel SPR sensor that can compensate for small changes in non-specific binding provided they have the same effect on both the channels. However, using separate channels for reference and sensing makes the system more complex and less accurate. Hastings *et al.* [133] and Slavik *et al.* [134] introduced an improved technique utilizing multiple surface plasmon waves present on the same sensing channel to distinguish background interfering effects with surface binding interactions. This dual-mode sensing approach performs sensing and interference compensation at the same sensing channel, thereby eliminating any errors associated with multi-channel sensing.

Even though significant advances have been made to provide reference compensation in propagating SPR sensors, the same cannot be said for localized SPR sensors. In a somewhat related effort, Irudayaraj and co-workers utilized a multi-probe sensing technique to detect two different target analytes in solution [49]. Gold nanorods with aspect ratio 2.0 and 3.2 were functionalized with different ligand molecules and used for the simultaneous detection of E.coli and S.typhimurium pathogens. Despite all the advances made in improving its sensitivity and detection limits, there has been a notable absence of efforts to make LSPR sensors more immune to interfering effects. To address

this problem we investigated a self-referencing technique that utilizes the multiple plasmon modes of a metallic nanostructure to distinguish target analyte from non-specific interactions. This body of work was inspired from dual-mode sensing technique employed for propagating SPR sensors described above.

SPR sensors, in their most basic form, measure only a single parameter, i.e., change in the resonance wavelength, that allows them to measure only one unknown quantity. Therefore, they cannot distinguish between specific target binding and other non-specific effects. Various LSPR sensors discussed in Chapter 2 that do support multiple surface plasmon modes, e.g., nanorods, triangular nanoparticles etc., only utilize its strongest resonance mode to measure antigen-antibody interactions. This work demonstrates that utilizing the various modes of complex nanostructures can optically compensate for non-specific interactions and allow the binding of target molecules to be measured separately. For example, to differentiate solution refractive index changes from surface binding interactions one would require nanostructures that support at least two surface plasmon modes. Ellipsoidal or rod-like particles are some of the simplest structures that exhibit two plasmon modes.

3.1.1 LSPR in elliptical nanoparticles

As explained in the previous chapters, LSPR is the result of collective oscillation of conduction electrons inside a metal nanoparticle with respect to the positive ions. In case of an elliptical nanoparticle, that can be imagined as a spherical nanoparticle elongated along one direction, the conduction electrons can oscillate in three different directions depending on the direction of polarization of the incident electric field [135]. Figure 3.1(a) displays the modes of oscillation of a prolate shaped elliptical nanostructure, also

known as a nanorod. The transverse mode, or high frequency mode, arises when the electric field of the incident electromagnetic wave is parallel to the short axis of the rod and the longitudinal mode, or low frequency mode, appears when the incident field is parallel to the long axis of the rod. Consequently, the spectrum of an ellipsoidal particle consists of two separated resonances in which the longitudinal mode appears at a higher wavelength (or lower frequency) as compared to the transverse mode in the electromagnetic spectrum. This can be explained intuitively by considering the restoring forces for the two resonance modes [136]. The smaller restoring force for longitudinal mode is a result of increased charge separation between the positive ions and its surface electrons. The spectral position of the transverse resonance mode coincides with the plasmon resonance of a spherical nanoparticle of the same size. Figure 3.1(b) also displays the absorption cross section for a typical nanorod based structure.

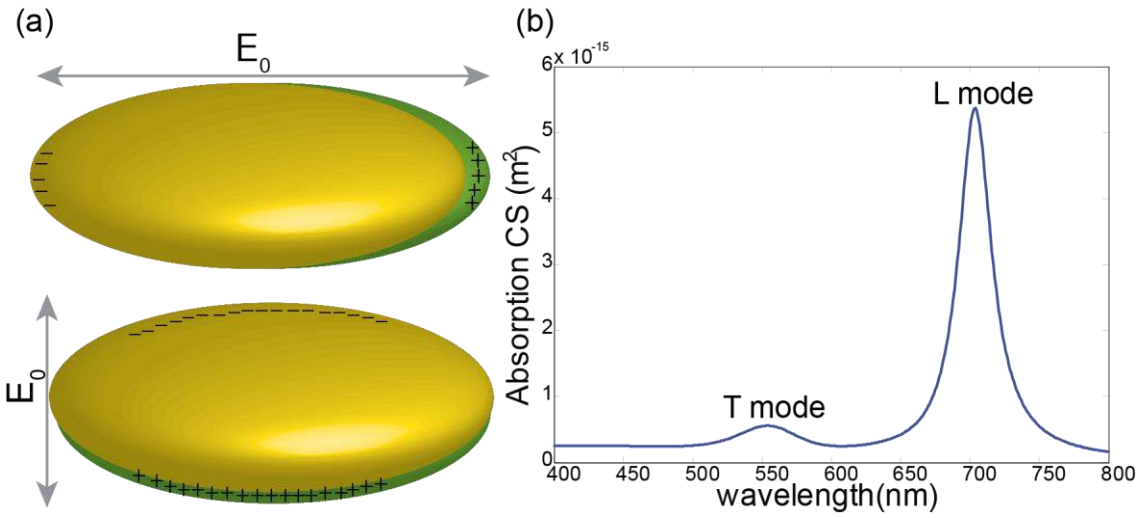

Figure 3.1 (a) Schematic of the two plasmon oscillation modes for a nanorod based structure, showing the displacement of conduction electron charge cloud relative to the nuclei, and, (b) Absorption cross-section of a gold nanorod with an aspect ratio($\mathcal{R}$) of 2 calculated using electrostatic approximation.

The optical properties of ellipsoidal nanoparticles in quasitatic approximation are very similar to that of spherical nanoparticles. Absorption and scattering cross-sections can still be calculated using (1.9) [12]. However, to accommodate for its anisotropic shape, the dipolar polarizability in the above equations is modified to include shape dependent depolarization factors, L_i –

$$\alpha_i = V \frac{\varepsilon_m - \varepsilon_d}{L_i(\varepsilon_m + \varepsilon_d) + \varepsilon_d} \tag{3.1}$$

where V denotes the volume of the elliposid, ε_m and ε_d the permittivity of nanorod and its surrounding medium and i defines its resonances mode. L_i is a function of the nanoparticle's aspect ratio ($\mathcal{R}$), defined as the ratio of its long axis to short axis, and in the case of prolate like ellipsoidal particles, can be calculated as –

$$\begin{aligned} L_1 = L_L &= \frac{1-e^2}{e^2}\left(-1 + \frac{1}{2e}\ln\left(\frac{1+e}{1-e}\right)\right) \\ L_2 = L_3 &= L_T = 1 - 2L_L \end{aligned} \tag{3.2}$$

where $e = 1 - 1/\mathcal{R}^2$ specifies the nanorod's ellipticity. Localized plasmon resonance for a nanorod occurs at frequencies for which the following condition is met–

$$\varepsilon_m = -\varepsilon_d \left(1 + \frac{1}{L_i}\right) \tag{3.3}$$

Both C_{abs} and C_{sca} exhibit strong enhancement around the two resonance modes with the longitudinal mode showing greater absorption and scattering as compared to the transverse mode. The electric field enhancement at the longitudinal plasmon resonance of a nanorod is orders of magnitude higher than what can typically be obtained for a spherical nanoparticle [137]. Figure 3.2 displays the E-field enhancement obtained at the longitudinal resonance mode of a silver nanorod as well as a spherical nanoparticle.

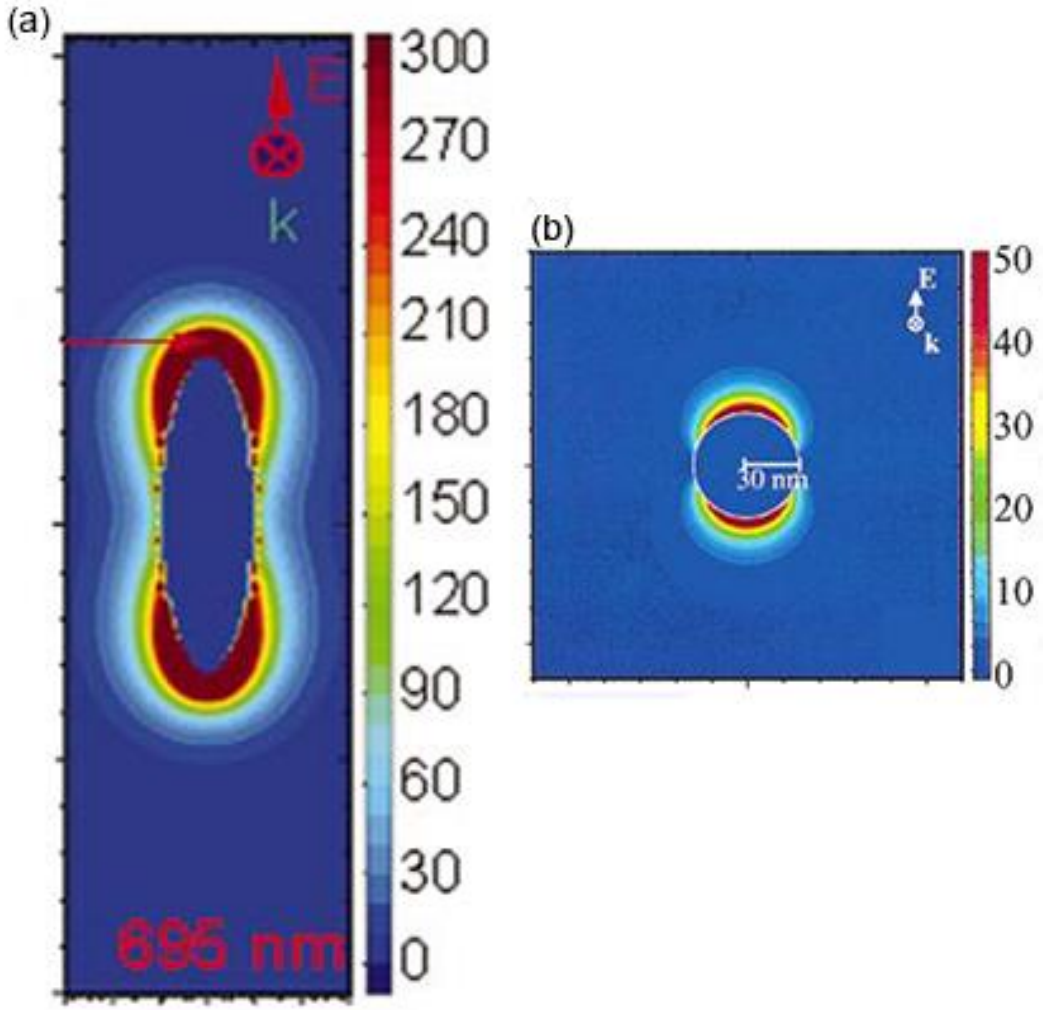

Figure 3.2 (a) Electric field enhancement at longitudinal plasmon resonance mode for a silver nanorod with $\mathcal{R}$ of 3.4 and an effective radius of 1.5nm, and (b) Electric field enhancement for a 30 nm radius silver nanoparticle at its surface plasmon resonance wavelength. Adapted with permission from [29, 137]

The LSPR of a nanorod is highly dependent on its size [138]. Figure 3.3 displays the extinction spectra of gold nanorods with different aspect ratios. As seen in the figure, the longitudinal mode strongly depends on the size of the nanorod, red shifting with increasing $\mathcal{R}$. The transverse mode, on the other hand, shows no appreciable change with increasing aspect ratio. Thus, the longitudinal plasmon resonance wavelength of nanorods

can be easily tailored from visible to near-IR, providing easier and improved tunability compared to various other nanostructures. This ability of nanorods to easily tune its plasmon wavelength, combined with the presence of a highly enhanced E-field around its surface make it extremely useful for biochemical sensing applications [37, 108, 139].

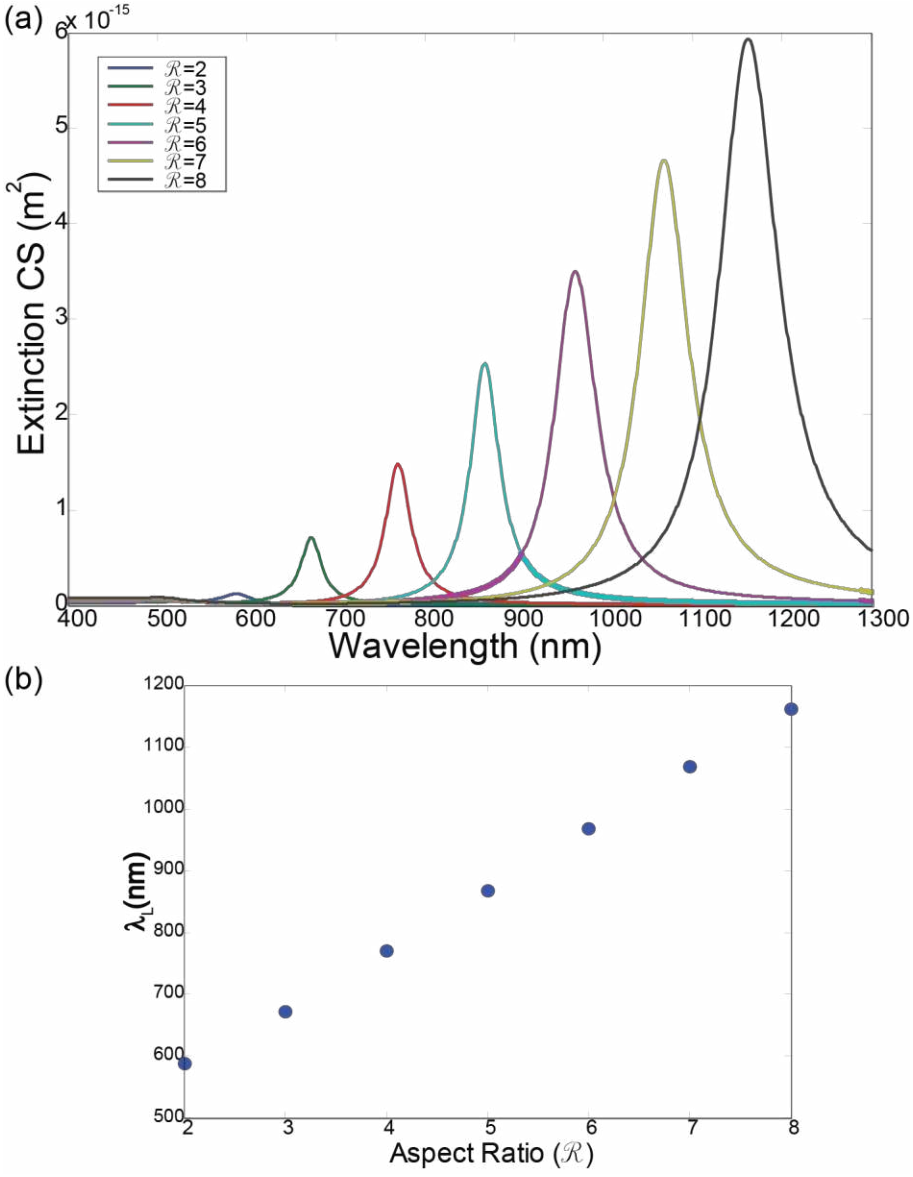

Figure 3.3 (a) Electrostatic extinction CS for a range of Au nanorods in aqueous solution using electrostatic approximation. The short axis of the nanorod is constant at 5nm and the long axis ranges from 10 to 40nm, and, (b) Linear shift of longitudinal wavelength of the nanorods with increasing $\mathcal{R}$.

3.1.2 Principle of Operation

If it is assumed that the two resonances of the metal nanorod are linearly related to the surface coverage of the bound analyte and to changes in the solution refractive index, the shifts in the longitudinal and transverse surface plasmon resonance can be expressed as –

$$\begin{aligned} \Delta\lambda_L &= S_{BL}\Delta n_B + S_{SL}\Delta C_S \\ \Delta\lambda_T &= S_{BT}\Delta n_B + S_{ST}\Delta C_S \end{aligned} \tag{3.4}$$

where S_{ST} and S_{SL} are the surface binding sensitivities, S_{BT} and S_{BL} are the bulk refractive index sensitivities for transverse and longitudinal resonance modes respectively. ΔC_{s} and Δn_{B} denote the surface coverage of the adsorbed layer and refractive index change respectively. If the bulk and surface sensitivities and the resonance wavelength shifts are known, the surface coverage and bulk index changes can be calculated directly from the following equations –

$$\begin{aligned} \Delta n_B &= \frac{\frac{\Delta\lambda_L}{S_{SL}} - \frac{\Delta\lambda_T}{S_{ST}}}{\frac{S_{BL}}{S_{SL}} - \frac{S_{BT}}{S_{ST}}} \\ \Delta C_S &= \frac{\frac{\Delta\lambda_L}{S_{BL}} - \frac{\Delta\lambda_T}{S_{BT}}}{\frac{S_{SL}}{S_{BL}} - \frac{S_{ST}}{S_{BT}}} \end{aligned} \tag{3.5}$$

Simple calculations using the electrostatic approximation for a core shell ellipsoidal structure in a homogenous medium were performed to demonstrate the self-referencing capability of nanorod based sensors. Figure 3.4 verifies that the plasmon resonances in gold nanorod shifts by different amounts for bulk and surface changes and thus, can help separate the two effects. This chapter shows, through biosensing experiments, that the two resonances of a gold nanorod can be used to differentiate between bulk and surface interaction in a biosensor.

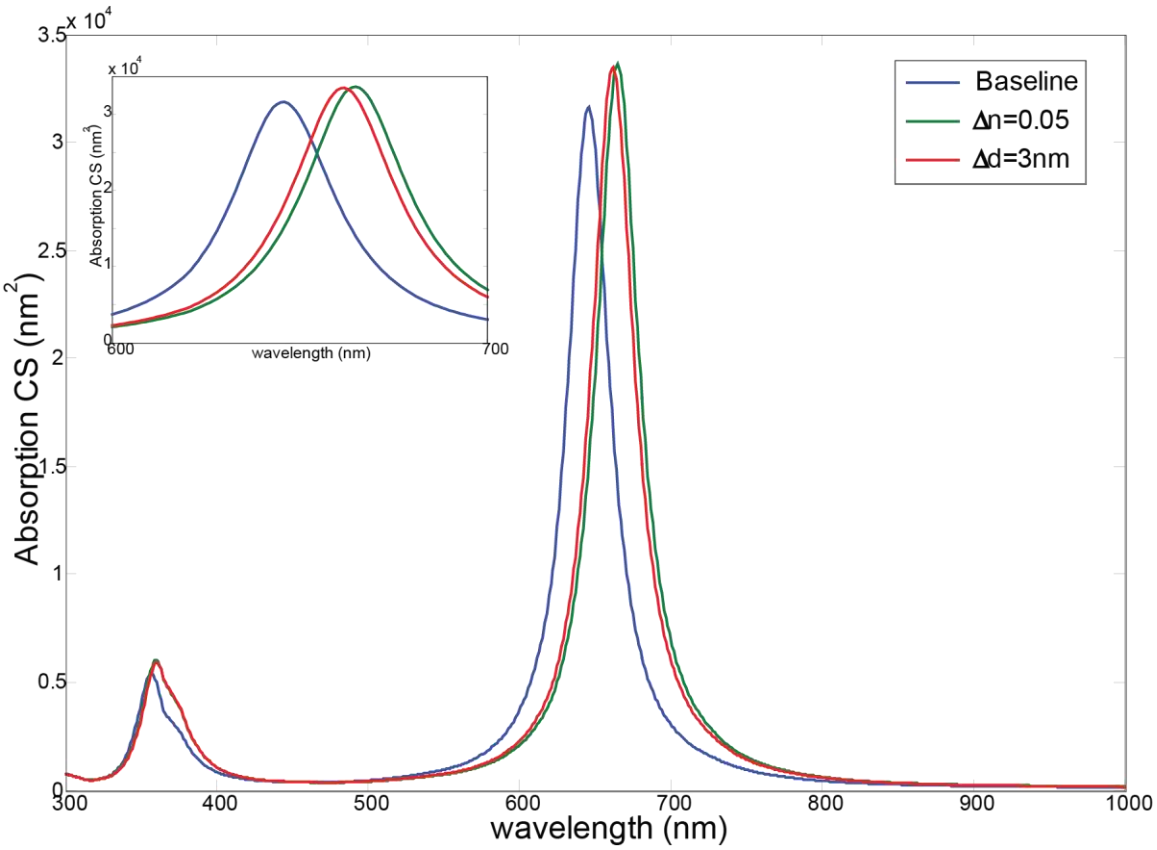

Figure 3.4 Calculated absorption cross section for silver ellipsoids in water with 50nm by 15nm by 15nm semi-axis. The change in absorption is shown due to change in solution refractive index by 0.05 RIU (Δn) and adsorption of 3 nm thick surface layer (Δd). Inset gives a zoomed in view of the wavelength shifts due to the two effects.

3.2 Sample Preparation

3.2.1 Materials

Indium Tin Oxide (ITO) coated glass substrates with resistivity of 15-30 Ω/m^2 were purchased from SPI supplies (West Chester, PA) and used as substrates. Gold (99.99%) sputtering target was purchased from Kurt J. Lesker (Jefferson Hills, PA). The resist, polymethyl methaacrylate (PMMA) was obtained from MicroChem (Newton, MA). Methyl IsoButyl Ketone (MIBK), N-methyl pyrrolidone (NMP), glycerol, acetone,

isopropyl alcohol (IPA) and ethanol were obtained from Fisher Scientific (Pittsburg, PA). Streptavidin and N-(6-[biotinamido]hexyl)-3′-(2’-pyridyldithio)propionamide (Biotin-HPDP) were purchased from Pierce Biotechnology (Rockford, IL). Tris-buffer saline solution (TBS) was generously provided by Dr. Yinan Wei’s laboratory at the University of Kentucky.

3.2.2 Sensor Fabrication

Gold nanorods were fabricated on an indium tin oxide (ITO) coated glass substrate. The substrate was first pretreated by sonicating in acetone, ethanol, isopropyl alcohol (IPA) and DI water for 5 minute each. The sample was then pre-baked at a temperature of 150°C for 3-5 minutes on a hot plate. This is done to ensure that the substrate is completely dry before proceeding to the next step. The substrate was allowed to cool down before spin coating it with 2% 950K PMMA dissolved in anisole, an electron beam sensitive positive resist at 1200rpm for 30 seconds. After spin coating, the substrate was again placed on a hot plate at 200°C for 3-5 minutes to harden the e-beam resist and evaporate any solvent that may be present on the substrate surface. This step is generally identified as soft-bake in the lithography process.

Gold nanorods were fabricated on the PMMA coated ITO substrate using Raith e_LiNE electron beam lithography tool (Raith Gmbh). Selected areas of the resist coated substrate were exposed to electron beam to pattern arrays of single pixel lines with a range of lengths and doses. Table 3.1 provides the e-beam exposure parameters used for writing arrays of nanorods. The pitch size within each array was kept constant at 1μm. The exposed areas of the substrate were developed by immersing the sample in a solution containing 1:3 ratio of MIBK and IPA for 30 seconds. The sample was then washed in

IPA and air dried. A 30 nm thin gold layer was then sputtered at the rate of 1.5 Å/sec on the developed ITO substrate. Finally, the remaining PMMA resist was stripped off by immersing the sample in 70°C NMP solution followed by washing the substrate in ethanol.

Table 3.1 Electron beam lithography exposure parameters used for writing nanorods on ITO substrate.

Primary Beam Energy	10keV
Aperture	30 µm
Line Dose	330 pC/cm
Line Step-size	4 nm
Dose Range	1 to 4 in intervals of 0.5
Working Distance	7 mm

3.2.3 Optical Characterization

Figure 3.5 illustrates the experimental setup used for measuring the scattering spectra from the arrays of nanorods. The apparatus was built around a Zeiss Axiovert 405M inverted microscope (Carl Zeiss Inc.). Light from a 100W halogen lamp was incident on the substrate through a 20X dark field infinity corrected objective with a Numerical Aperture (NA) of 0.5. Light scattered from the nanorods was collected using the same objective and directed to a port containing an adjustable aperture and a Glan Taylor polarizer (Thorlabs Inc.). The aperture suppresses scattered light from any other source on the sample allowing only the light scattered from the selected area to pass through. The scattered light was dispersed using an Acton SP-150 spectrograph (Princeton

Instruments) fitted with a 150 lines/mm grating. The dispersed light was measured using a thermoelectric cooled CCD camera (PIXIS 256, Princeton Instruments). All spectra were normalized to scattering from the bare substrate.

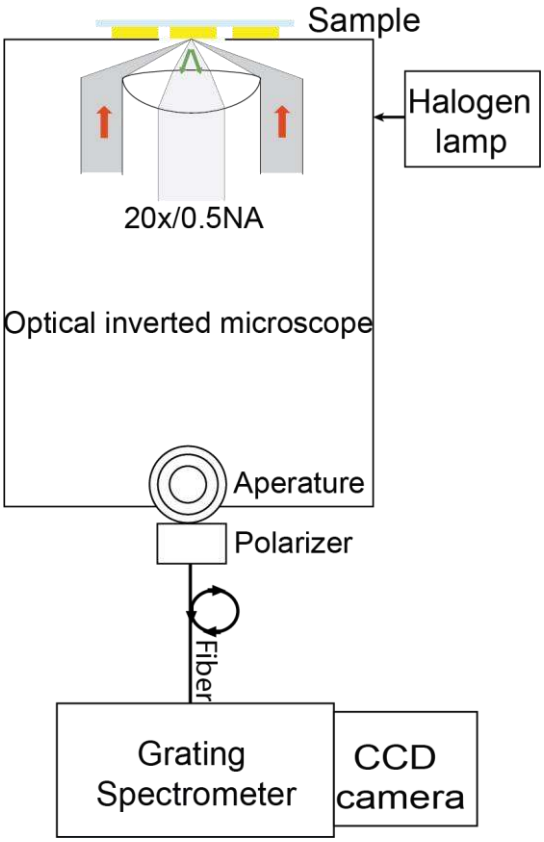

Figure 3.5 Schematic of the optical setup used for scattering measurements.

3.3 Biosensing Experiment

Biotin-streptavidin bio-sensing experiment was implemented to test the bulk referencing capability of the nanorod based sensor. The sample was incubated with 200 μM Biotin-HPDP in a 10 mM phosphate buffer solution with a pH of 7.2 at room temperature overnight for biotin labeling. The coated surface was rinsed with deionized water and air-

dried. The sensor was then clamped in a custom made acrylic flow cell with fluorinated ethylene propylene (FEP) coated channels. It was then placed on the microscope stage and the scattering measurements were recorded using custom software scripted in LabView (National Instruments). Solutions were introduced to the sensor surface through polytetrafluoroethylene (PTFE) tubing at a constant flow rate of 500 µl/min using a low pulsation peristaltic pump (Ismatec). A 50 mM Tris buffer (pH=8.0) solution was used as the baseline to carry out the sensing experiments. The buffer solution was modified by adding either 50% (w/v) glycerol to change the background refractive index by Δn_B=0.068 or 0.2 mg/ml streptavidin to provide a surface binding interaction.

3.4 Results and Discussions

Gold nanorod arrays were fabricated on an ITO coated glass substrate using the electron beam lithography process described previously. The ITO coating mitigated charging during electron beam exposure and also improved adhesion of the gold compared to uncoated BK7 glass substrates. As a result, no additional adhesion layer, such as Ti or Cr, was required. Figure 3.6(a) shows a representative scanning electron micrograph of such arrays with a gap size of 1 µm. The approximate in-plane dimensions of the nanorods are 140 nm by 85 nm and 180 nm by 80 nm respectively. The thickness of gold nanorods is confirmed to be 30 nm through AFM measurements as shown in Figure 3.6(b).

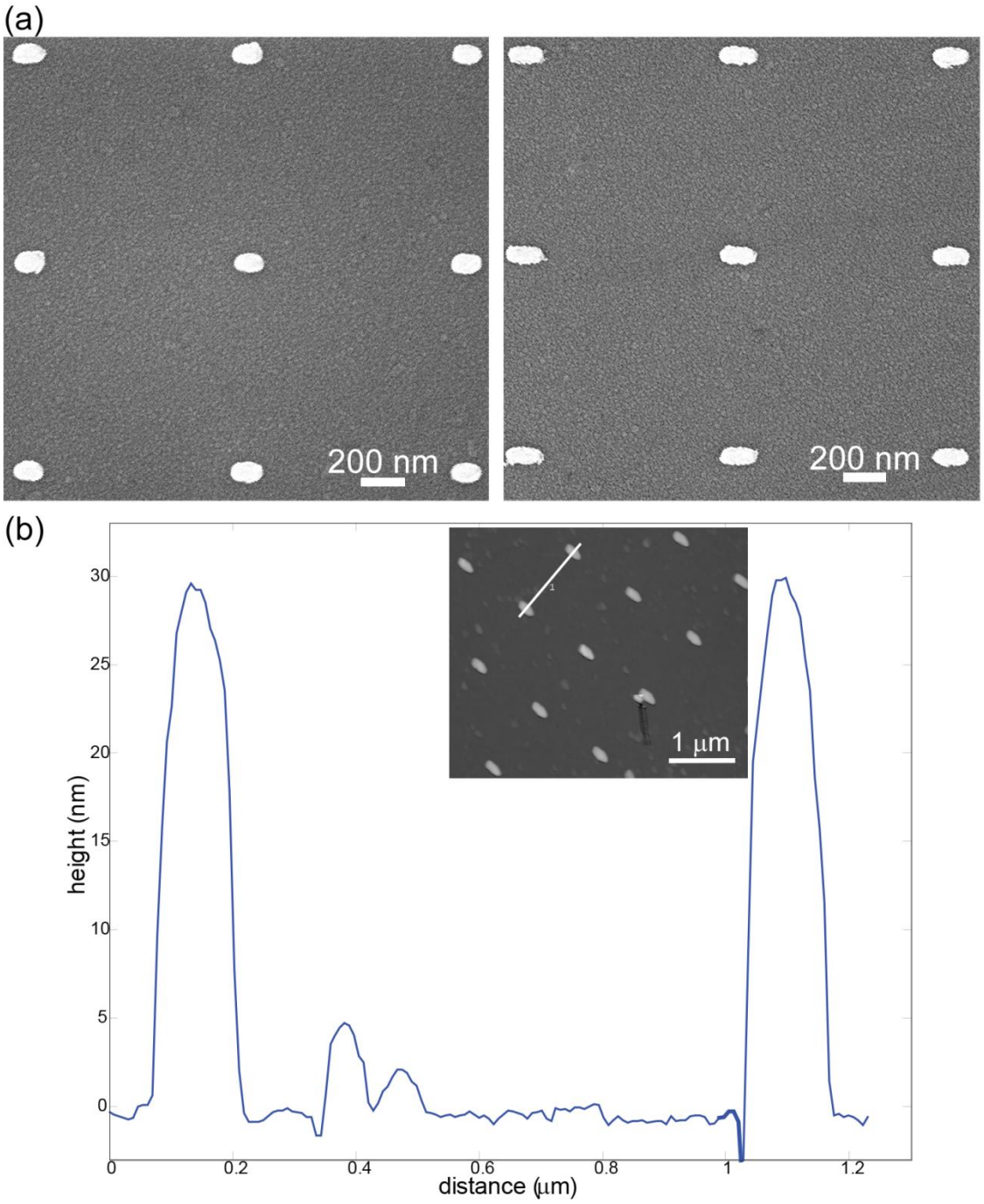

Figure 3.6 (a) SEM images of nanorod arrays of sizes 140nm by 85nm (left) and 180nm by 80nm (right) and a pitch size of 1µm fabricated using electron beam lithography, and, (b) AFM measurement displaying the height of the naorods to be approximately 30nm. Inset in (b) shows the area scanned for measurement.

Spectral profile of the fabricated gold nanorods were measured using the optical spectra. The corresponding normalized visible-NIR scattering spectra of nanorods of size 141 nm by 67 nm is shown in Figure 3.7(a). Figure 3.7(b) shows the longitudinal scattering spectrum of the nanorods obtained when the electric field is polarized along its long axis. Similarly, the transverse spectrum, seen in Figure 3.7(c) is measured when the field is polarized along the short axis of the nanorods. The dependence of the transverse and longitudinal resonance wavelengths to the surrounding medium can be seen in Figure 3.8(a,b). Both the transverse and longitudinal resonances red shifts with increase in the medium refractive index (n_{med}) from air (n_{med}=1) to water (n_{med}=1.33). Scattered light was collected from an area containing approximately 80 nanorods. Similarly, Figure 3.8(c) shows the dependence of the plasmon resonances to change in the size of gold nanorods. The unpolarized scattering spectrum clearly shows that the longitudinal mode strongly depends on the size of the nanorod, red shifting with increasing nanorod size, while the transverse mode only shows a slight increase in its scattering intensity [135].

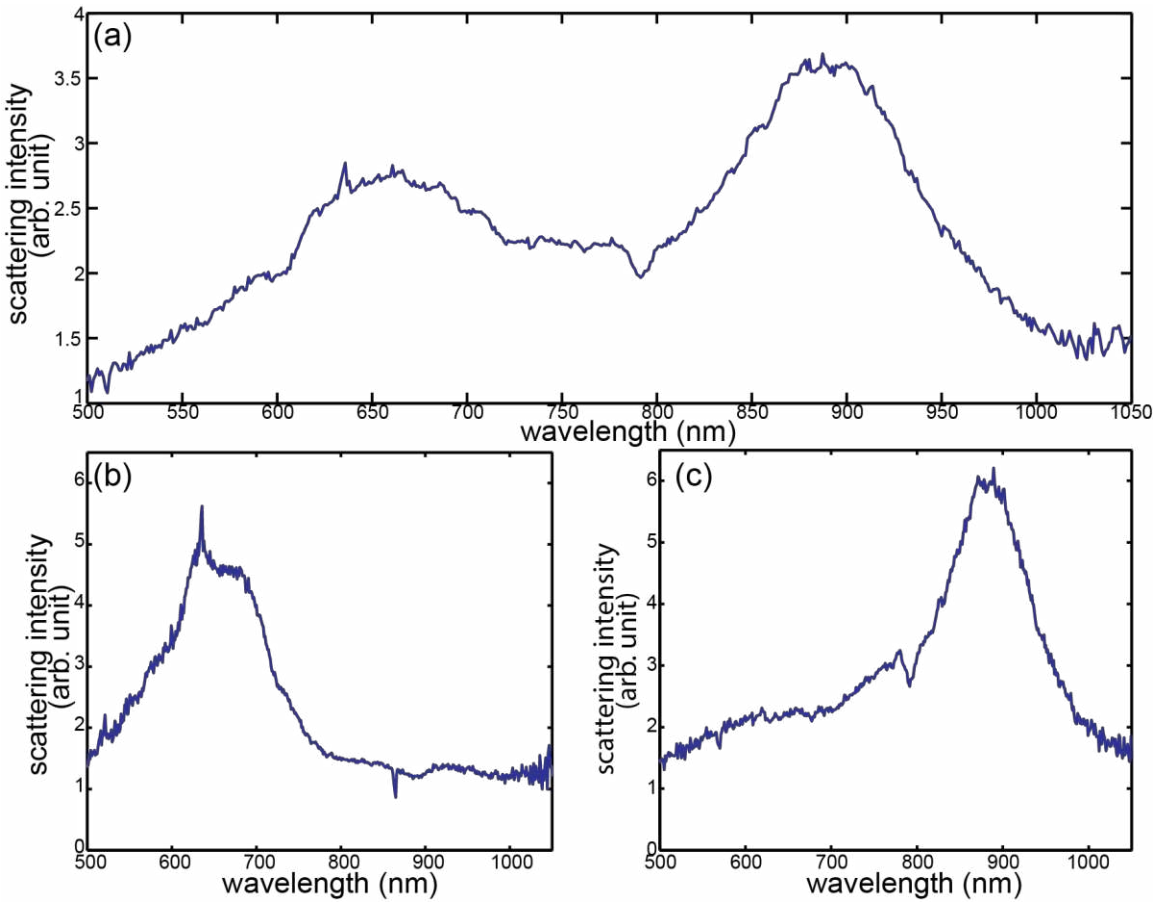

Figure 3.7 Normalized scattering spectra of an array of gold nanorods of size 141 nm by 67 nm under the following conditions (a) when light is unpolarized, (b) when light is polarized along the short axis of the rods, and (iii) when light is polarized along the long axis of the rods.

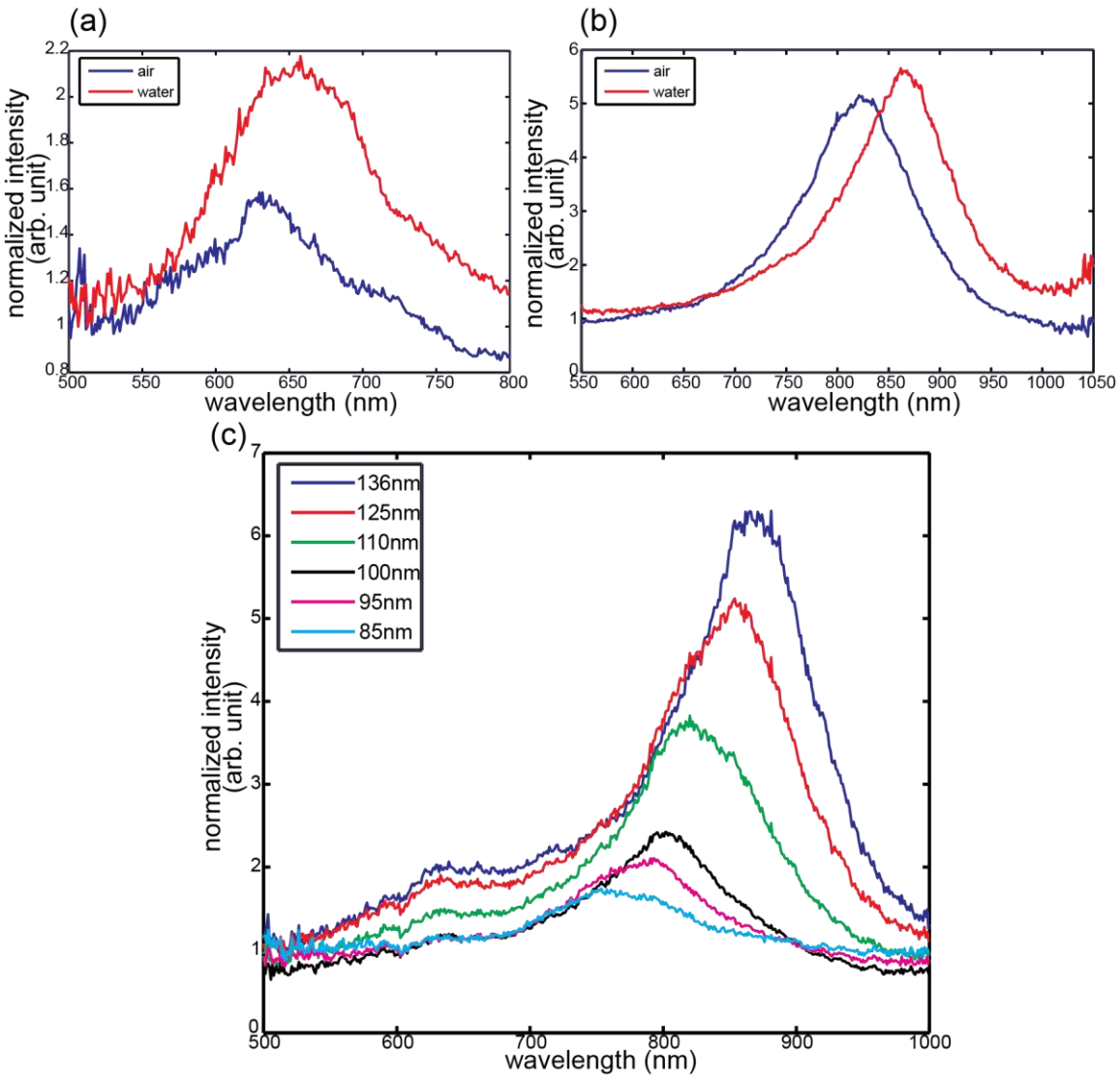

Figure 3.8 Shift in (a) transverse and (b) longitudinal plasmon resonances for an array of gold nanorods of size 110 nm by 54 nm with a change in surrounding refractive index from air (n_d = 1) to water (n_d = 1.33) and, (c) unpolarized scattering spectra for nanorod arrays with increasing size of its long axis.

3.4.1 Bulk interference compensation

To prepare the plasmon resonance based sensor for biosensing interaction, the surface of the gold nanorod arrays was functionalized with Biotin-HPDP. Figure 3.9(a) shows the chemical structure of the molecule labeled with biotin. The disulfide group in Biotin-HPDP reduces to sulfhydryl groups that binds to the gold nanorod surface resulting in a biotin terminated self-assembled monolayer [140]. Figure 3.9(b) gives a schematic illustration of the functionalized gold nanorod sensor.

The functionalized gold nanorod sensor was clamped inside a flow cell and then placed on the microscope stage as shown in Figure 3.9(c). Solutions containing glycerol and streptavidin were then introduced onto the sensor surface through the flow cell. Figure 3.10(a) and (b) display the response of the longitudinal and transverse modes of the sensor through such a process. Buffer solution was first introduced into the flow cell to stabilize the resonance wavelengths as well as to provide a baseline for the experiment. Exposure of the gold nanorods to the glycerol solution produces an expected red shift in its longitudinal and transverse resonances. As seen in the figure, the resonances blue shift back to their baseline values as soon as buffer solution is reintroduced onto the sensor surface. Exposure to 0.2 mg/ml streptavidin solution causes the resonances to red shift as streptavidin binds to the biotin coated sensor surface. This is followed by reintroducing the buffer solution to remove any unbound or physisorbed streptavidin. The plots clearly show that the longitudinal and transverse resonances shift by different amounts with surface and bulk interactions and thus can help differentiate the two effects.

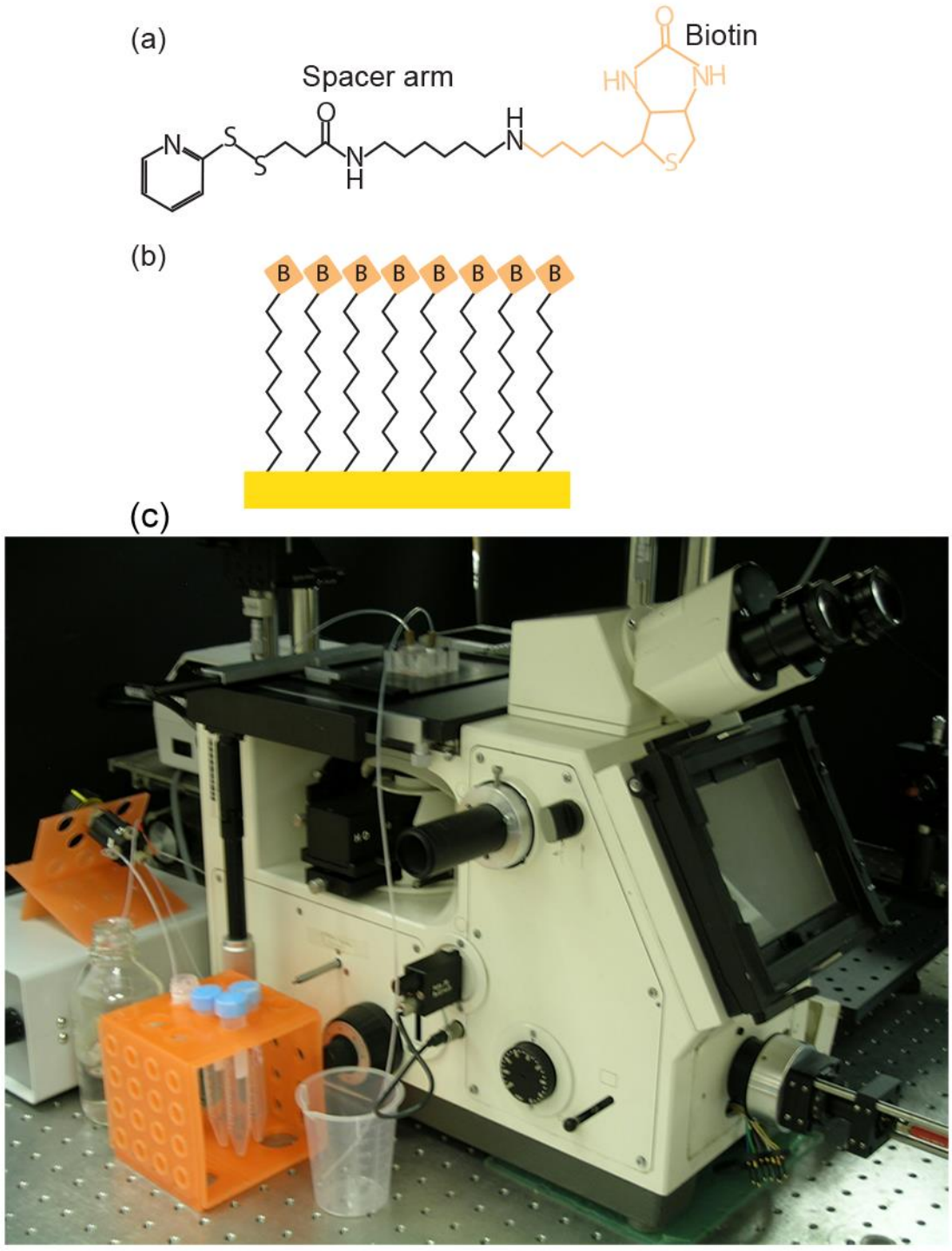

Figure 3.9 (a) Structure of Biotin-HPDP, (b) Schematic of gold surface labeled with biotin through its spacer arm, and (c) Image of the optical setup modified for biosensing experiment. Notice the flow cell containing the sample sitting on the microscope stage.

Figure 3.10 (c) and (d) show the bulk refractive index change and relative surface layer thickness as functions of time calculated using the model described in (3.5). There is a small amount of crosstalk between the two modes that leads to a small bulk index error for times greater than 2500 s, as shown in Figure 3.10(c). This can likely be attributed to the calibration errors, small baseline drift, or nonlinearity in the sensor response. More interestingly, there are dynamic effects which lead to large spikes in the surface coverage estimates during solution index changes as can be seen in Figure 3.10(d), when the solution is switched from pure buffer to buffer with glycerol. These dynamic effects were also observed with a similar gold nanorod array sensor (Figure 3.11). It should be noted that in both sets of data, this effect is only present when there is an abrupt shift in the resonance wavelengths as witnessed in Figure 3.10(a) and (b) when the solution is changed from buffer to buffer with glycerol. No such effect is observed when the resonance wavelengths shifts gradually which occurs during the introduction of streptavidin with buffer solution. From a practical standpoint, these dynamic errors may or may not be acceptable depending upon the rate of change of the bulk index.

The bulk sensitivities for the longitudinal and transverse modes of the nanorod sensor were calculated using the linear model and found to be 145 nm/RIU and 55nm/RIU respectively. Although it is difficult to quantify the surface concentration of streptavidin, we can evaluate the ratio of the surface sensitivities for the longitudinal and transverse mode. The ratios of bulk and surface sensitivities and the figure of merit for the nanorod sensor were calculated to be $S_{BL}/S_{BT} = 2.6$, $S_{SL}/S_{ST} = 3.5$ and $\chi = 0.88$.

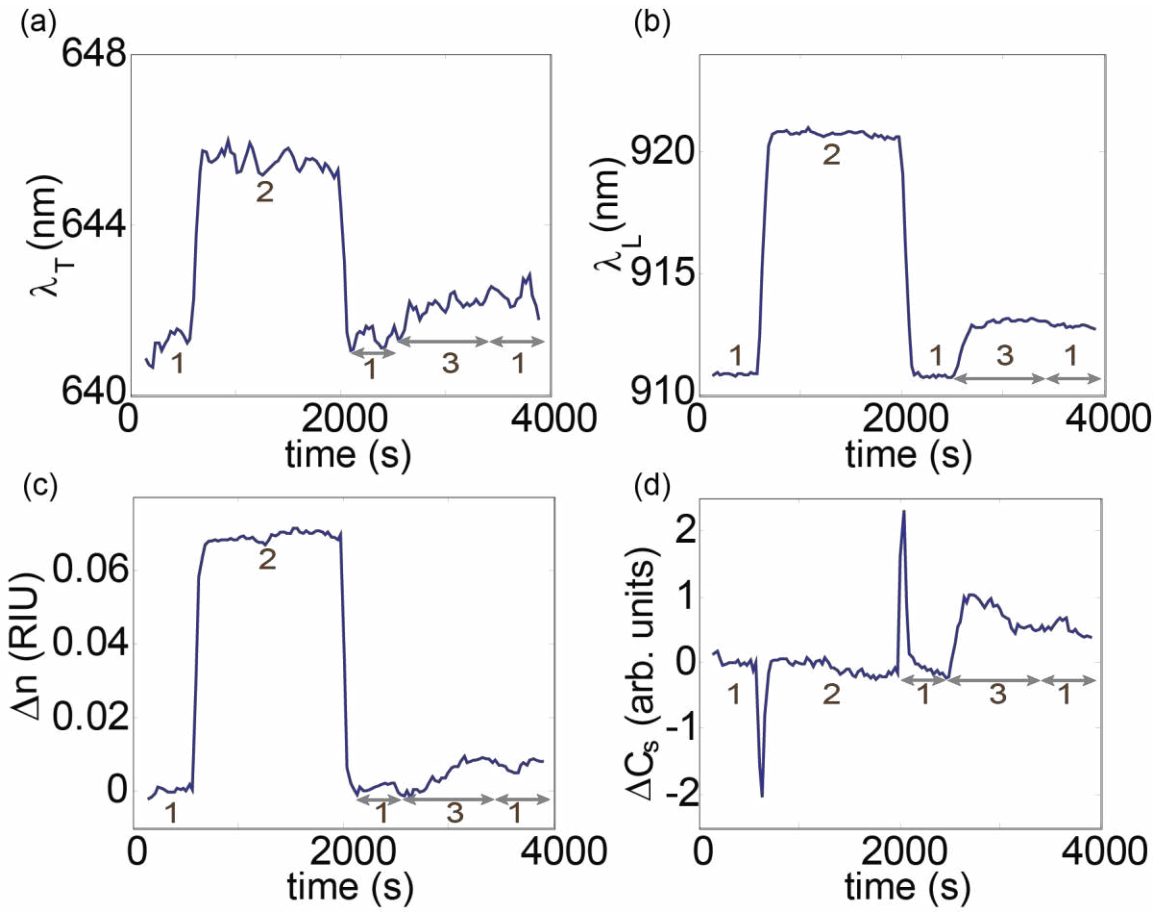

Figure 3.10 Sensor response of biotin functionalized gold nanorod array to streptavidin binding. (a,b) Shift in transverse and longitudinal resonance wavelength versus time. (c,d) Bulk refractive index and relative surface layer coverage calculated from (a,b). The solutions were introduced through the flowcell in the following order: (1) buffer, (2) buffer with 50%(w/v) glycerol, and (3) buffer with streptavidin. Adapted from [141]

To further validate the response of gold nanorods to bulk and surface interactions we conducted the same sensing experiment on similar sized nanorod array also fabricated using electron beam lithography. Figure 3.11(a) and (b) displays changes in the transverse and longitudinal resonance wavelength while Figure 3.11(c) and (d) shows the calculated bulk refractive index and surface changes. As expected, we see large spikes in Figure 3.11(d) when the solution is changed from buffer to buffer with glycerol. The bulk sensitivities calculated using the linear model for this sensor are 240 nm/RIU and 150

nm/RIU for longitudinal and transverse resonance modes respectively. The ratio of bulk and surface sensitivities along with the figure of merit was found to be 1.6, 1.3 and 0.25 respectively. The disparity in the sensitivities and figure of merit values measured for the two nanorod arrays could be the result of different end shape geometries as the second array exhibited a more rectangular shape and poorer quality liftoff.

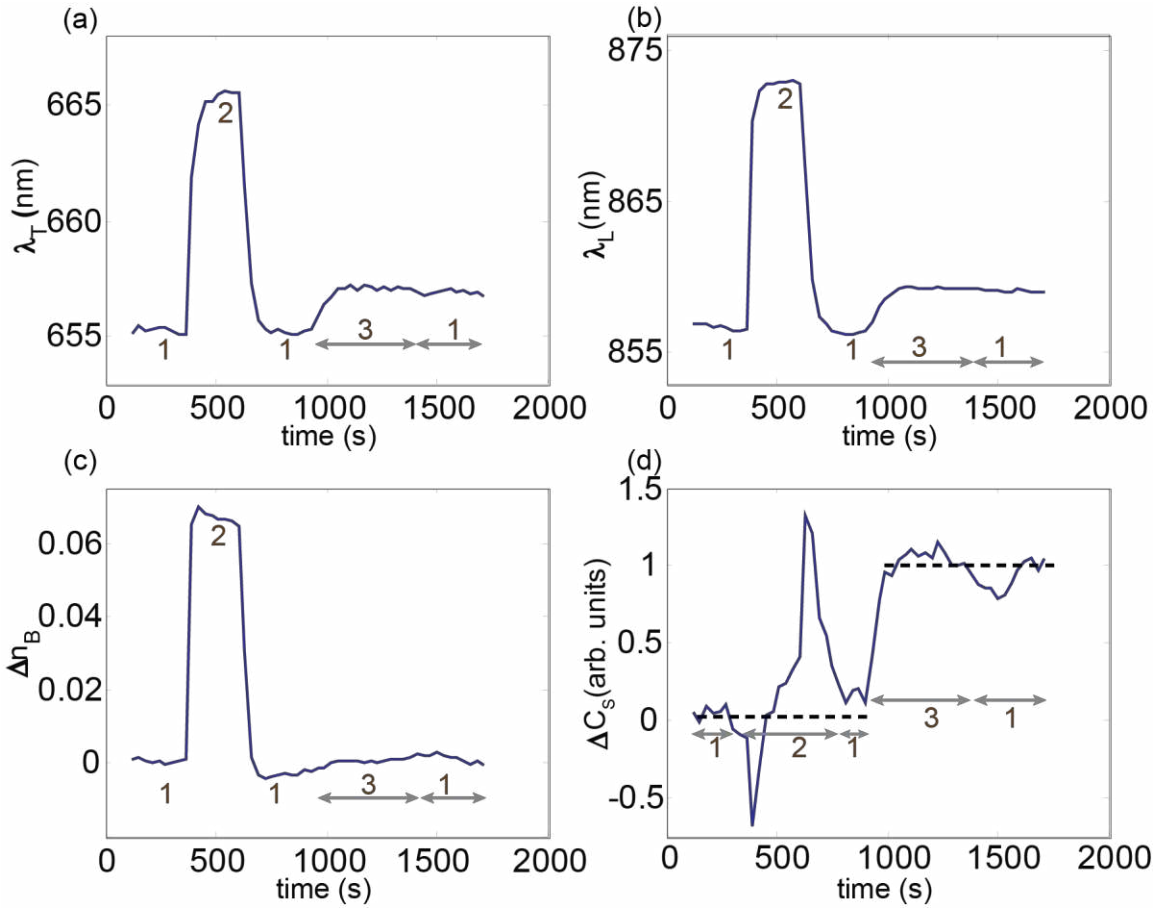

Figure 3.11 Sensor response of biotin functionalized gold nanorod array to streptavidin binding. (a,b) Shift in transverse and longitudinal resonance wavelength versus time. (c,d) Bulk refractive index and relative surface layer coverage calculated from (a,b). The solutions were introduced through the flowcell in the following order: (1) buffer, (2) buffer with 50%(w/v) glycerol, and (3) buffer with streptavidin. Adapted from [141]

The surface limit of detection (LOD) at three standard deviations for the nanorod array sensor, in terms of fractional surface coverage of streptavidin, was calculated to be 0.1595. This value is considerably higher than that of a traditional dual mode SPR sensor [133], but the sensing volume is dramatically smaller. The ratio of sensitivity to the full width at half maximum (FWHM) of the resonance, which is a common figure of merit for single mode sensors and is indirectly related to LOD, was determined to be 1.9.

The longitudinal mode bulk sensitivity for the sensor is somewhat lower than those measured by Mayer et al. [65] and Chen et al. [32] for chemically synthesized gold nanorods. On the other hand, FOM of the sensor is higher than the value reported by Mayer et al. In each case, the aspect ratio of the rods varied from the gold nanorods described here, a factor which can significantly impact the sensitivity. It should be noted that the structures used in these experiments have not yet been optimized to obtain the lowest limits of detection, but still clearly demonstrate that a nanorod array based sensor can differentiate surface interactions from bulk index changes.

3.5 Conclusions

This chapter demonstrates that the two localized surface-plasmon resonances of a gold nanorod can compensate for changes in the background refractive index and allow surface binding of the target analyte to be measured separately. These sensors exhibit comparable performance to other nanorod LSPR sensors with the added benefit of bulk index compensation. When compared to traditional SPR sensors based on propagating surface plasmons, these sensors offer dramatically reduced sensing volume, but will require further optimization to achieve similar figures of merit and limits of detection.

Chapter 4

Interference Compensation using Multi-mode LSPR Sensors

4.1 Background

As shown in the previous chapter, nanostructures with two surface plasmon modes may be utilized to distinguish the refractive index changes in the bulk solution from the surface target binding interaction. The various surface plasmon modes are the result of the collective oscillation of conduction electrons within anisotropic metal nanostrucutres [138]. The longitudinal and transverse modes of the nanorod, with electric field profiles localized at different regions on the sensor surface allows one to separate the bulk solution changes from the surface binding interactions. However, a fully self-referencing sensor should be also be able to distinguish a target binding interaction from non-specific interfering binding interactions. Interference due to non-specific adsorption of non-target molecules is a very prominent problem in immunoassays [142]. These non-specific molecules can adsorb on the sensor surface resulting in reduced sensitivities as well as an erroneous analysis of the molecule of interest.

Various techniques have been examined to reduce the effect of non-specific adsorption in immunoassays, especially in complex solutions like serum and blood plasma. Choi *et al.* suggested several methods to reduce non-specific binding in microfluidic biosensors. The authors displayed experimentally that using a short chain as opposed to a long-chain thiol linker molecule on a polycrystalline gold surface helps reduce non-specific adsorption [143]. Various other parameters like the surface roughness and crystal

orientation of the metal were also shown to affect the amount of non-specific binding on the sensor surface. A different method employed by Uludag *et al.* [144] made use of sandwich assay technique as opposed to a direct assay technique to detect target analyte in undiluted serum solution. This technique allowed the authors to detect very low concentrations (8.5pM) of prostate specific antigen (PSA) using antibody-modified 40 nm gold nanoparticle.as the secondary antibodies in high serum concentrations. But perhaps the most widely employed method to prevent non-specific binding in SPR sensors involve the use of molecules like bovine serum albumin (BSA), casein, polyethylene glycol (PEG) etc. to block the non-specific binding sites on the sensor [145, 146]. These blocking molecules physically adsorb on the sensor surface regions that are not coated with receptor molecules, as shown in Figure 4.1. However, the presence of such molecules results in a reduction in the sensitivity of the sensor and may not be the best way to deal with non-specific binding. These and various other pre-processing steps do not completely eliminate the sensor's response to interfering molecules. Multi-mode sensors seek to circumvent blocking steps by optically addressing the problem using the multiple modes of a complex structure to compensate for non-specific binding as well as bulk solution interference.

A fully self-referencing optical sensor requires at least three surface plasmon modes to simultaneously measure refractive index of the sensing solution, specific binding of target molecules and non-specific binding of interfering molecules. The three modes should exhibit localized electric field profiles at different regions of the sensor surface as well as different field decay lengths to be able to differentiate between the various effects. A U-

shaped nanostructure is one such structure that exhibits the above mentioned characteristics.

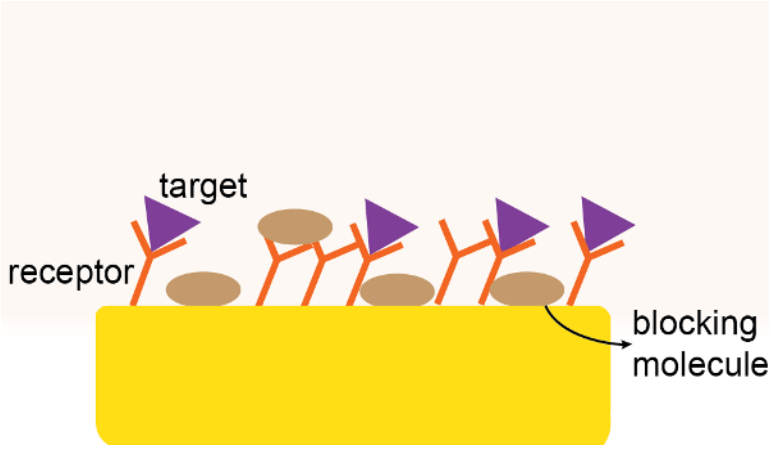

Figure 4.1 Schematic illustrating the use of blocking molecules to avoid non-specific adsorption on the sensor surface.

U-shaped structures are inspired from the widely used split-ring resonator (SRR) based structures. These structures have been extensively studied for use as metamaterials [147, 148] and to a somewhat lesser extent as refractive index sensors [149, 150]. Due to its anisotropic shape, the structures exhibits different resonance modes for different incident field polarization [151-153]. A typical U-shaped structure, as shown in Figure 4.2(a), supports at least three surface plasmon modes depending on the electric field polarization either parallel to or perpendicular to the gap of the nanostructure. Figure 4.2(b) illustrates a typical scattering spectra obtained from U-shaped gold nanostructures.

Various groups have investigated the different modes associated with U-shaped nanostructure through both experiments and numerical analysis. Enkrich *et al.* [154] and Rockstuhl *et al.* [152] provide a thorough analysis on the dependence of the resonance modes of the structure to its various structural parameters including among others, gap

width, arm length & thickness and base length & thickness. However, most of the U-shaped structures investigated have been micron-scale particles with resonance wavelengths ranging from low to mid-IR range. Klein *et al.* [155] were among the first group to experimentally design and analyze a scaled down version of U-shaped structures with resonance wavelength in the near-IR range. Rockstuhl *et al.* [153] numerically explained the various resonances associated with the U-shaped structures in terms of plasmonic resonances of increasing order of the whole structure instead of the magnetic resonance of an LC resonant circuit as had been the case previously [148, 156]. Zhang *et al.* numerically compared a silver U-shaped nanostructure to a parallel nanorod based structure using DDA [157]. The authors observed that even though the two structures are horizontally symmetric, the extinction spectra of a U-shaped structure displays a higher number of resonant peak with larger electric field enhancements for the same incident electric field polarization. The presence of a large number of hot spots in the U-shaped nanostructure make them extremely useful for applications in sensing and SERS.

Chang *et al.* [158] were among the first group to study SRR based structures for sensing applications. The authors investigated, both numerically and experimentally, the sensing characteristics of the various modes of the SRR structure. They measured the reflectance spectra after applying dielectric layers of various thicknesses over the sensor surface to measure the sensitivity and detection range of the various modes of the structure. Pryce *et al.* [150] further designed coupled SRRs with resonance wavelengths in the near-IR to IR wavelength range on a PDMS substrate to investigate its sensitivities and figures of merit Liu *et al.* [159] were the first group to study the transmission and

sensing properties of a complementary SRR based nanoscale structure with resonances in the visible wavelength range.

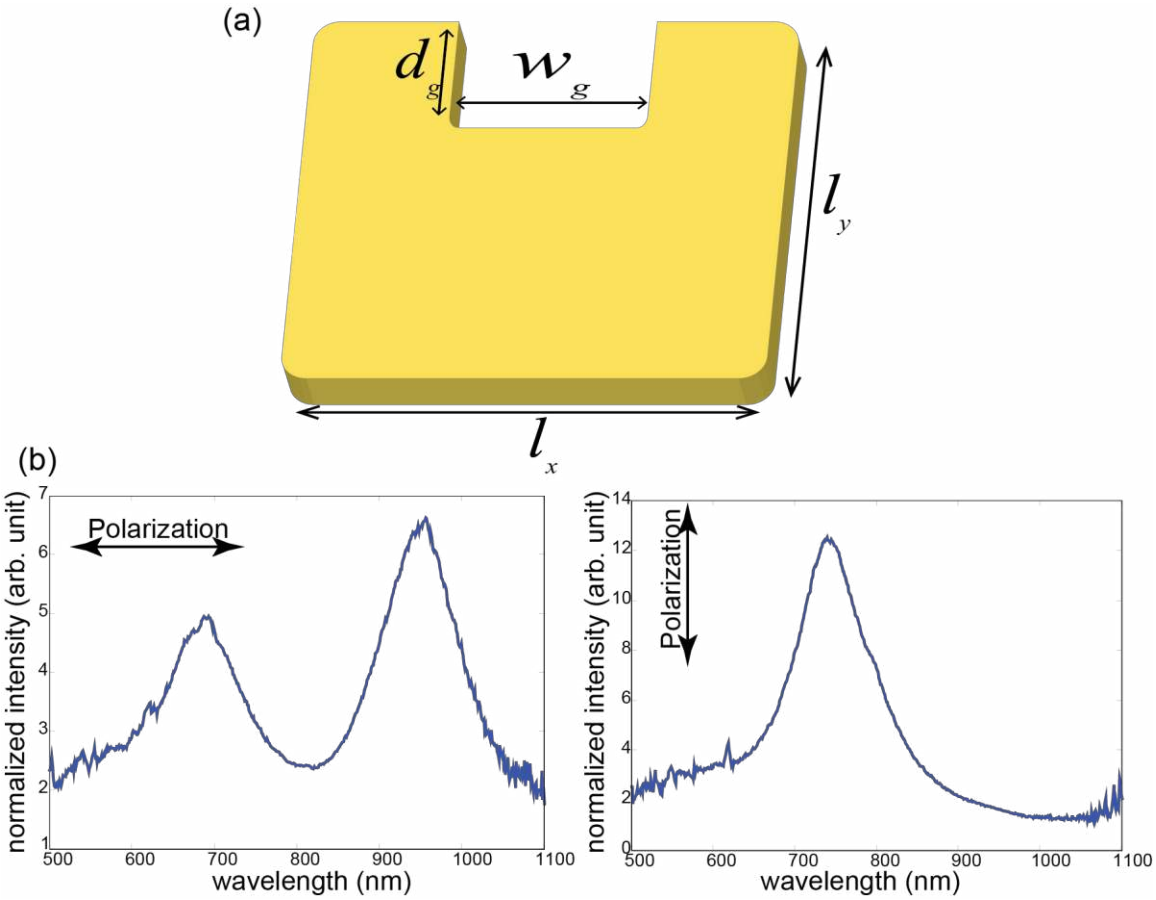

Figure 4.2 (a) Schematic of a U-shaped structure. The parameters ℓ_x and ℓ_y represent the horizontal and vertical lengths of the nanostructure and w_g and d_g define its gap width and height respectively, and, (b) Typical scattering spectrum obtained from U-shaped gold nanostructures with ℓ_x = 125nm, ℓ_y = 125nm, w_g = 45nm and d_g = 40nm.

As seen in Figure 4.2(b), a typical U-shaped structure supports atleast three plasmon modes depending upon the polarization of the incident light. The different plasmon modes have localized electric field profiles at separate regions on the sensor surface, the

details of which will be discussed in Chapter 5. Therefore, the overlap of the electric field with the gold surface and the sensor substrate will be different for the various modes of the nanostructure. This, along with the differences in the decay lengths, will allow the three plasmon modes to respond differently for the bulk and surface interference as well as the target interaction. This chapter provides a detailed analysis of the operation of such a sensor, describe the dependence of its resonances on geometry, and characterize its performance by differentiating specific streptavidin-biotin binding from non-specific bovine serum albumin (BSA) adsorption and bulk index changes.

4.1.1 Working Principle

If it is assumed that the multiple plasmon resonances of a metal nanostructure are linearly related to the changes in the surface coverage due to specific and non-specific surface effects as well as refractive index of the background solution, the shift in the resonances can be expressed using the following system of equations –

$$\Delta\lambda_i = S_{B-i}\Delta n_B + S_{S-i}\Delta C_S + S_{NS-i}\Delta C_{NS} \tag{4.1}$$

where $\Delta\lambda_i$ is the shift in the i^{th} resonance; $S_{S\text{-}i}$, $S_{NS\text{-}i}$ and $S_{B\text{-}i}$ are the specific surface sensitivities, the non-specific surface sensitivities and the bulk sensitivities for each resonance; and ΔC_S, ΔC_{NS} and Δn_B represent the specific surface coverage change, the non-specific surface coverage change and the bulk refractive index change respectively. Changes in specific and non-specific surface coverage as well as the index of the background solution can be calculated from above equation provided the sensitivities and wavelength shifts are known.

The sensitivities described above can be sufficiently different to distinguish these effects because of the different electric field distributions associated with each resonance.

Specifically, each resonance has different field strengths at the surface of the gold nanostructure and along the surface of the substrate, and each decays at a different rate into the bulk solution. Considering all of the possible interactions as perturbations and using the perturbation theory developed by Raman *et al.* (neglecting system loses), one can approximate the sensitivities as [160] –

$$S_{X-i} = \partial\lambda_i/\partial X \approx \lambda_{0i}\left(\int d\boldsymbol{r}\frac{\partial\epsilon(\boldsymbol{r})}{\partial X}|\boldsymbol{E_i}(\boldsymbol{r})|^2 \Big/ \int d\boldsymbol{r}W_{0i}\right) \tag{4.2}$$

where λ_{0i} is the unperturbed i^{th} resonance wavelength, X is one of C_{S}, C_{NS}, and n_{B}, and $\partial\epsilon/\partial\text{X}$ is the change in dielectric constant for the associated perturbation. Finally, E_{i} is the electric field and $W_{0\text{i}}$ the total energy density associated with the i^{th} resonance. In fact, this is often an acceptable approximation for perturbed plasmonic systems.

Often the dielectric perturbation takes the form of a change in permittivity over a specific volume as shown in Figure 4.3. For example, the effect of nonspecific binding on the i^{th} resonance can be simplified to –

$$\begin{aligned} S_{NS-i} = \frac{\partial\lambda_i}{\partial C_{NS}} \approx \frac{\lambda_{0i}}{\int d\boldsymbol{r}W_{0i}}\left[\frac{\partial\epsilon_{NS,m}}{\partial C_{NS}}\int_m^{m+h} d\boldsymbol{r}|\boldsymbol{E_i}(\boldsymbol{r})|^2\right. \\ \left. + \frac{\partial\epsilon_{NS,sub}}{\partial C_{NS}}\int_{sub}^{sub+h} d\boldsymbol{r}|\boldsymbol{E_i}(\boldsymbol{r})|^2\right] \end{aligned} \tag{4.3}$$

where $\partial\epsilon_{\text{NS,m}}/\partial C_{\text{NS}}$ represents the change in refractive index induced by nonspecific binding to the metallic nanostructure or its functionalized surface. The limits of integration are written to indicate that the perturbation extends from the metal's surface, m, to a distance h above it. Likewise, $\partial\epsilon_{\text{NS,sub}}/\partial C_{\text{NS}}$ represents the change in refractive index induced by nonspecific binding to the substrate. In general, different affinities for the substrate and the metallic surfaces will give rise to significantly different values for

$\partial\epsilon_{\mathrm{NS,m}}/\partial C_{\mathrm{NS}}$ and $\partial\epsilon_{\mathrm{NS,sub}}/\partial C_{\mathrm{NS}}$. Of course, functionalization of these surfaces alters the affinities from those of the original materials. Similar expressions can be written for the effects associated with specific binding and bulk index changes. For specific binding the effective thickness, *h*, of the layer will be different giving rise to additional differentiation of the sensitivities. In the case of a bulk index perturbation, *h* goes to infinity and there is no need to differentiate between the metal and the substrate.

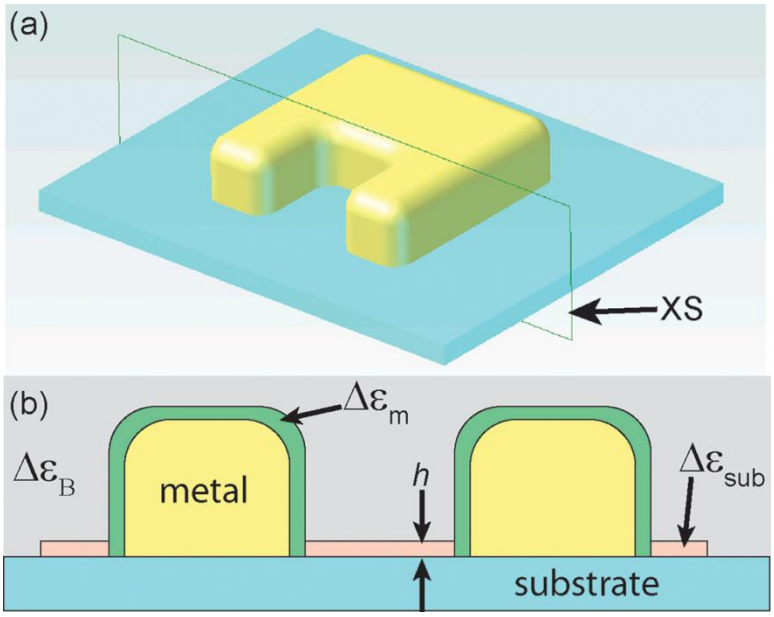

Figure 4.3 (a) 3D schematic of a U-shaped LSPR sensor. XS indicates cross-sectional plane shown in (b), (b) Dielectric perturbations associated with binding (specific or nonspecific) to the metal and substrate are indicated by $\Delta\epsilon_m$ and $\Delta\epsilon_{sub}$ respectively. The effective thickness of the bound layers is labeled *h*. A perturbation to the bulk permittivity is indicated by $\Delta\epsilon_B$. The difference in the perturbation, and thus resonce wavelength, of the modes by bulk changes, as well as binding of a target analyte or an interfering species, leads to the sensor's ability to differentiate the various effects.

4.2 Experimental Methods

4.2.1 Materials

Indium Tin Oxide (ITO) coated glass substrates with resistivity of 15-30 Ω/m^2 were purchased from SPI supplies (West Chester, PA). Gold pellets (99.99% pure) were purchased from Kurt J. Lesker (Jefferson Hills, PA). Polymethyl methaacrylate (PMMA) was obtained from MicroChem (Newton, MA). Methyl IsoButyl Ketone (MIBK), N-methyl pyrrolidone (NMP), acetone, isopropyl alcohol (IPA), ethanol, glycerol and bovine serum albumin (BSA) were obtained from Fisher Scientific (Pittsburg, PA). Streptavidin and N-(6-[biotinamido]hexyl)-3′-(2’-pyridyldithio)propionamide (Biotin-HPDP) were purchased from Pierce Biotechnology (Rockford, IL). Tris-buffer saline solution (TBS) was generously provided by Dr. Yinan Wei’s laboratory at University of Kentucky.

4.2.2 Substrate Preparation

Gold nanorods were fabricated on an indium tin oxide (ITO) coated glass substrate. The ITO coating mitigated charging during electron beam exposure and also improved adhesion of the gold compared to uncoated BK7 glass substrates. The substrate was pretreated by sonicating in acetone, ethanol, and isopropyl alcohol (IPA) for 5 minutes each. This was followed by plasma etching the substrate for 5 minutes under oxygen to remove any organic contaminants. Finally, the substrate was sonicated in DI water for another 5 minutes before prebaking it at 150 °C for 3-5 minutes on a hot plate. After letting the sample cool down, the substrate was spin coated with 950K PMMA dissolved in 2% anisole at 4000rpm for 45 seconds. The substrate was then soft-baked at a temperature of 200°C for another 3-5 minutes before exposure to electrons.

4.2.3 Sensor Fabrication

The sensors were fabricated using a Raith E-LiNE electron beam lithography system on the PMMA coated ITO/glass substrate. Table 4.1 displays the various electron beam lithography exposure parameters used to pattern arrays of U-shaped nanostructures. This was followed by the development of the exposed PMMA in a 1:3 ratio of MIBK to IPA for 60 seconds. The sample was then washed in IPA for another 30 seconds and air dried. A 20-nm thick gold layer was evaporated on the developed sample using a thermal evaporator with deposition rate of 0.8 Å/sec. The unexposed PMMA was removed, and the gold lifted off, by immersing the sample in N-methyl pyrrolidone (NMP) heated to a temperature of 70ºC. Finally, the sample was washed under ethanol and air dried.

Table 4.1 Electron beam lithography exposure parameters for writing U-shaped nanostructures.

Primary Beam Energy	30keV
Aperture	20 µm
Area Dose	300 µC/cm^2
Area Step-size	4 nm
Dose Range	1 to 4 in intervals of 0.5
Working Distance	7 mm

4.2.4 Optical Measurements

The scattering properties of the U-shaped gold nanostructures were measured using Zeiss Axiovert 405M inverted microscope equipped with a 100W halogen lamp as well as a cube polarizer (Thorlabs Inc) fitted to one of its output port. A 20X dark-field objective with an imaging numerical aperture (N.A.) of 0.5 was used to illuminate the sensor surface as well as collect the scattered light from the gold nanostructures. After passing through the polarizer, the scattered light was directed to a grating spectrograph (Acton Instruments, SP-150) fitted with 150 lines/mm grating and a thermoelectric cooled CCD camera (Princeton Instruments) using two multimode optical fibers (Thorlabs Inc). Each fiber carried one polarization of scattered light and the spectra were separately resolved by the imaging spectrograph. The scattering spectrum from the nanostructures was normalized to the spectrum from the bare ITO substrate.

4.2.5 Biosensing Experiment

The self-referencing capability of the sensor was tested by using biotin-streptavidin binding as a target interaction along with bovine serum albumin (BSA) adsorption for non-specific interaction. Prior to functionalization, the sensor surface was cleaned by washing in acetone, IPA and DI water followed by an oxygen plasma etch for 3-5 minutes. The sensor was functionalized by incubating it overnight in a 10 mM phosphate buffer solution (pH 7.2) containing 200 μM of N-(6-[biotinamido]hexyl)-3'(2'-pyridyldithio)propionamide at room temperature for biotin labeling. The sensor, clamped inside a custom made acrylic flow cell, was placed on the microscope stage and the scattering spectra for the two polarizations were recorded simultaneously using Labview.

In addition, the Labview code tracked the peak positions of the three resonances in real time.

Different solutions were introduced on the surface of the sensor through polytetrafluoroethylene (PTFE) tubing at a constant flow rate of 650µl/min with the help of a peristaltic pump (Ismatec). A 50 mM Tris buffer solution with a pH value of 8 was used as the reference sensing solution. The sensor surface was exposed to (a) 25% (w/v) Glycerol in buffer to provide bulk refractive index change, (b) 0.2 mg/ml Streptavidin in buffer to provide specific surface interaction and (c) 5 mg/ml bovine serum albumin in buffer to provide a non-specific binding interaction.

4.3 Results and Discussions

Figure 4.4 illustrates the process utilized for the fabrication of U-shaped gold nanostructures on an indium tin oxide (ITO) coated BK7 glass substrate using electron beam lithography. The ITO coating was added to avoid charging during exposure to electron beam. A representative scanning electron micrograph (SEM) of an array of U-shaped nanostructures can be seen in Figure 4.5. The average geometrical parameters of the U-shaped nanostructures are ℓ_x =225nm, ℓ_y =195nm, w_g =80nm, d_g =110nm and ℓ_x =134nm, ℓ_y =103nm, w_g=48nm and d_g=50nm for the top and bottom nanostructures respectively. The gap between the structures is measured to be 1 µm.

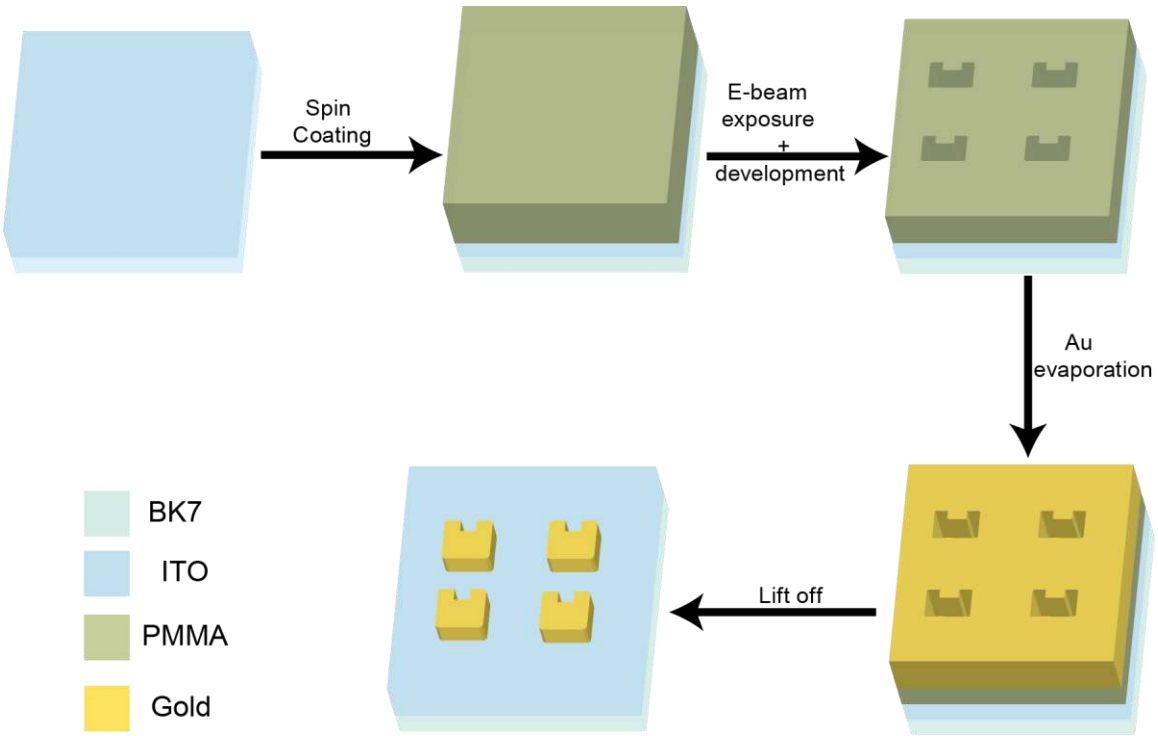

Figure 4.4 Schematic of the process used in the fabrication of U-shaped gold nanostructures through electron-beam lithography.

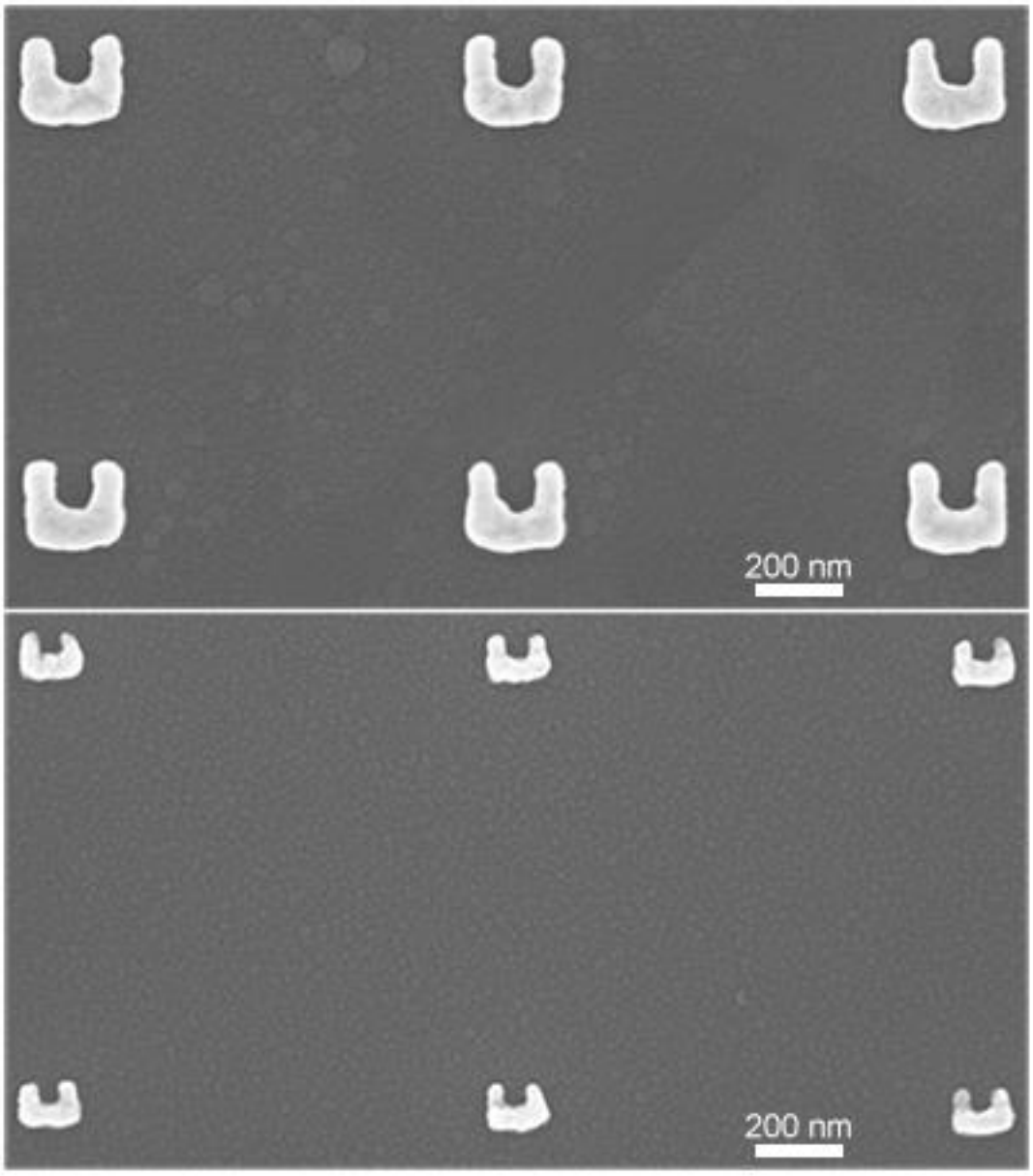

Figure 4.5 SEM images of U-shaped gold nanostructures arrays fabricated using electron-beam lithography. Dimensions of the structure are (top) ℓ_x = 225nm, ℓ_y = 195nm, w_g = 80nm and d_g = 110nm; (bottom) ℓ_x = 134nm, ℓ_y = 103nm, w_g = 48nm and d_g = 50nm. Pitch size in both images is 1 μm.

The fabricated nanostructures were optically characterized using the schematic described in Figure 4.6. Figure 4.7 displays the normalized horizontally and vertically polarized scattering spectra of the nanostructures collected from a spot size of approximately 10 µm. To further characterize the nanostructures, scattering spectra were also collected for arrays with varying gap depth (d_g). Figure 4.8 shows the comparison of the horizontally and vertically polarized scattering spectra of U-shaped nanostructures with different gap height values. As can be seen in the figure, the long-wavelength plasmon resonance of the horizontally polarized spectrum shows a red-shift with increasing value of d_g. These observations are in accordance with the results published by various research groups on split ring resonators (SRR) and U-shaped nanostructures [154, 155, 161].

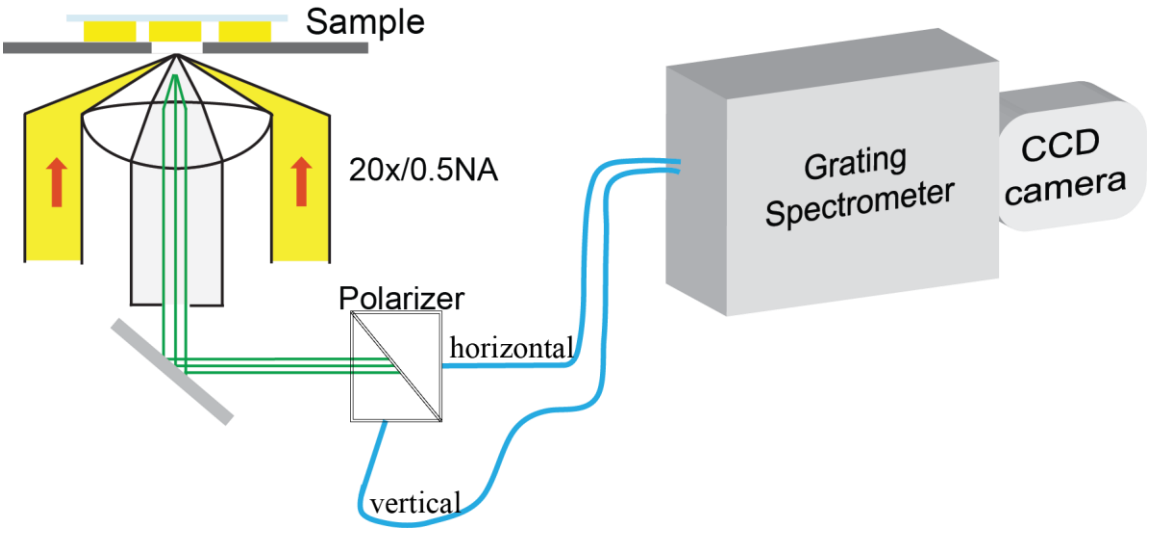

Figure 4.6 Schematic of the optical setup used for dark-field scattering measurements of U-shaped gold nanostructures.

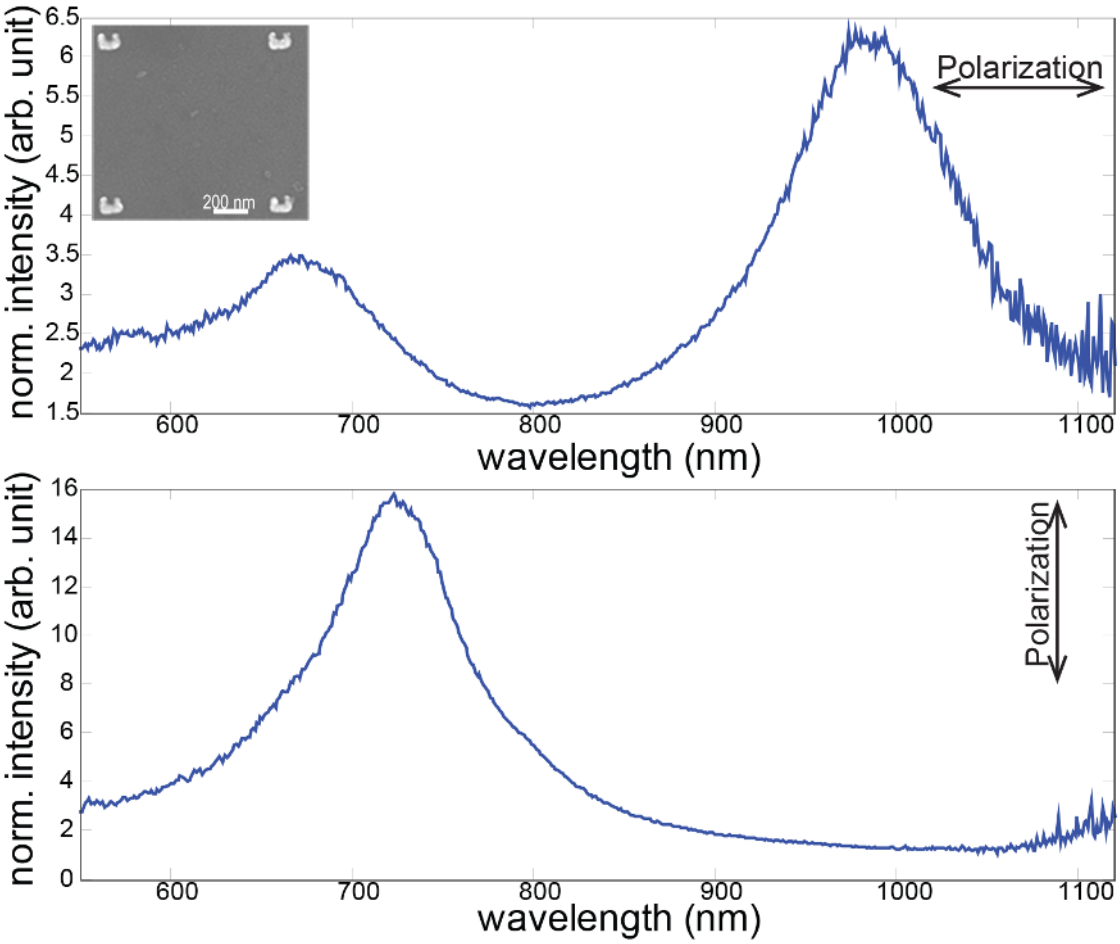

Figure 4.7 Optical scattering spectrum from an array of U-shaped nanostructures with the electric field polarized along its horizontal axis (top) and along the vertical axis (bottom). Inset shows the SEM image of the nanostructure array with sizes ℓ = 128nm, ℓ_y = 106nm, w_g = 47nm and d_g = 45nm.

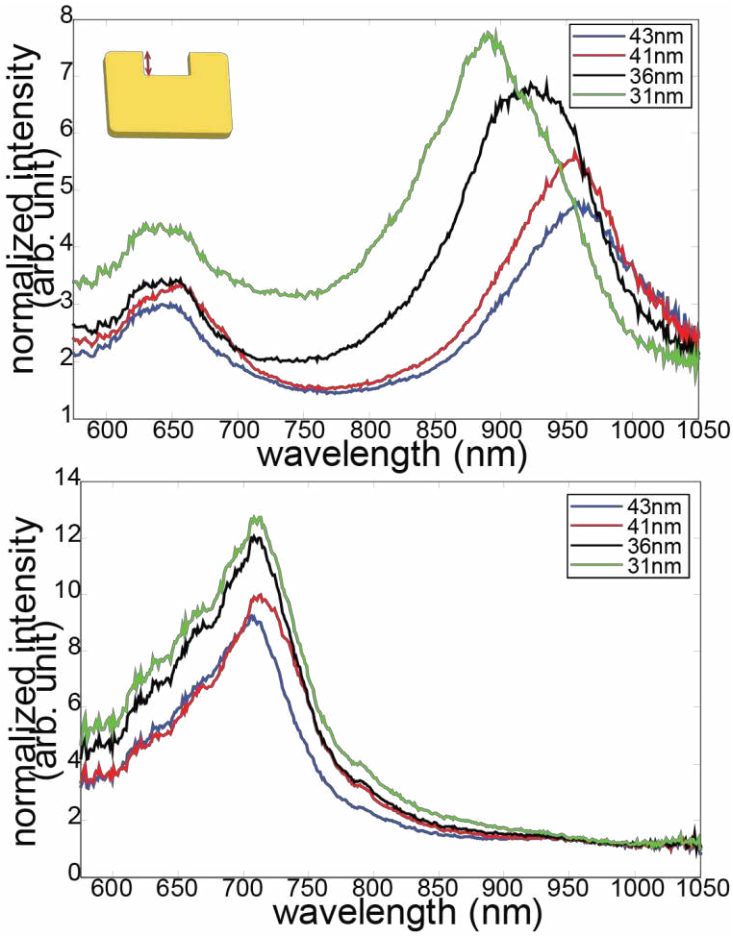

Figure 4.8 Normalized scattering spectra from arrays of U-shaped nanostructure with varying gap heights d_g.

4.3.1 Reference Compensation using U-shaped nanostructures

The U-shaped nanostructure based sensor was tested for its self-referencing capability by functionalizing the gold nanostructure surface with biotin-HPDP. Figure 4.9 shows the schematic of the biotin labeled gold nanostructure clamped inside the acrylic flow cell as well as an image of the optical setup modified for the biosensing experiment. Glycerol, streptavidin and bovine serum albumin (BSA) were added to tris-buffer solution to induce a bulk refractive index change, a specific target interaction, and a non-specific surface effect respectively. Figure 4.10 displays the relative peak shifts in the three

localized surface-plasmon resonance wavelengths versus time for the U-shaped nanostructure as different solutions are introduced on the sensor surface using a flow cell. A 50mM buffer solution was first introduced to stabilize the peak wavelength and to provide a baseline for the experiment. Exposure to Glycerol (25% w/v) causes the three wavelengths to red-shift due to a change in background refractive index by Δn_B=0.034 refractive index units (RIU). As expected, the three resonance wavelengths shift back to their base values after the reintroduction of the pure buffer solution. Introduction of 0.2 mg/ml streptavidin solution produces an expected red-shift resulting from the binding of streptavidin molecules to the biotin labeled gold nanostructures. Buffer was then reintroduced to remove any unbound streptavidin from the sensor surface. Finally, exposure to 5 mg/ml bovine serum albumin (BSA) produces a further red-shift in the three wavelengths as the BSA binds non-specifically on the sensor surface. As seen in Figure 4.10, the three resonance wavelengths shift by different amounts for the various surface and bulk interactions and thus can differentiate the various effects. Even though the decay lengths associated with the various modes of the sensor are smaller than those of a traditional SPR sensor [162], they are still substantially larger than the dimensions of the streptavidin and BSA molecules. This explains the smaller red-shift observed due to binding of streptavidin and BSA as compared to when the 25% glycerol solution is introduced to the sensor surface. This difference in the surface and bulk sensitivities is also consistent with the difference in sensitivities predicted by Mie theory for gold spheres whose dipole resonances fall in this wavelength range.

The bulk refractive index change as well as the fractional specific and non-specific surface binding change with respect to time is shown in Figure 4.11. These shifts were

calculated using the linear model for a self-referencing sensor described in (4.1). Small amounts of cross talk observed between the three resonance modes of the sensor can be attributed to small baseline drifts or small nonlinearities in the sensor response. The linear bulk sensitivities for the three resonance modes of the U-shaped nanostructure, measured as the shift in the resonance wavelengths with respect to the change in the refractive index of the background solution, were calculated to be $S_{B\text{-}1}=\Delta\lambda_1/\Delta n_B$ = 70 nm/RIU, $S_{B\text{-}2}=\Delta\lambda_2/\Delta n_B$ = 170 nm/RIU, $S_{B\text{-}3}=\Delta\lambda_3/\Delta n_B$ = 120 nm/RIU.

Table 4.2 summarizes the bulk as well as the specific and non-specific surface sensitivities calculated for the U-shaped nanostructure based sensor. The specific and non-specific surface sensitivities were calculated as the ratio of the shift in resonance wavelengths to unit change in the surface coverage of the adsorbed target analyte and interfering molecule respectively. It is notable that the non-specific response for λ_2 is larger than its specific binding response. This may be possible due to the electric field profile for λ_2 which is localized around the gap of the U-shaped nanostructure where the probability of non-specific binding of BSA is higher than the specific binding of the streptavidin. Of course, incomplete surface coverage of streptavidin on the biotin coated sensor surface could also contribute to this. Table 4.2 also provides the figure of merit (FOM) for the horizontal and vertical polarized resonances of the sensor. The FOM defines the ability of LSPR sensors to resolve small refractive index changes and is obtained by dividing the bulk sensitivity to the full width at half-maximum (FWHM) of the resonance peak [52]. If one considers the possibility of incomplete surface coverage for streptavidin and/or BSA, then the sensitivities and FOM set a lower bound on the sensor's performance.

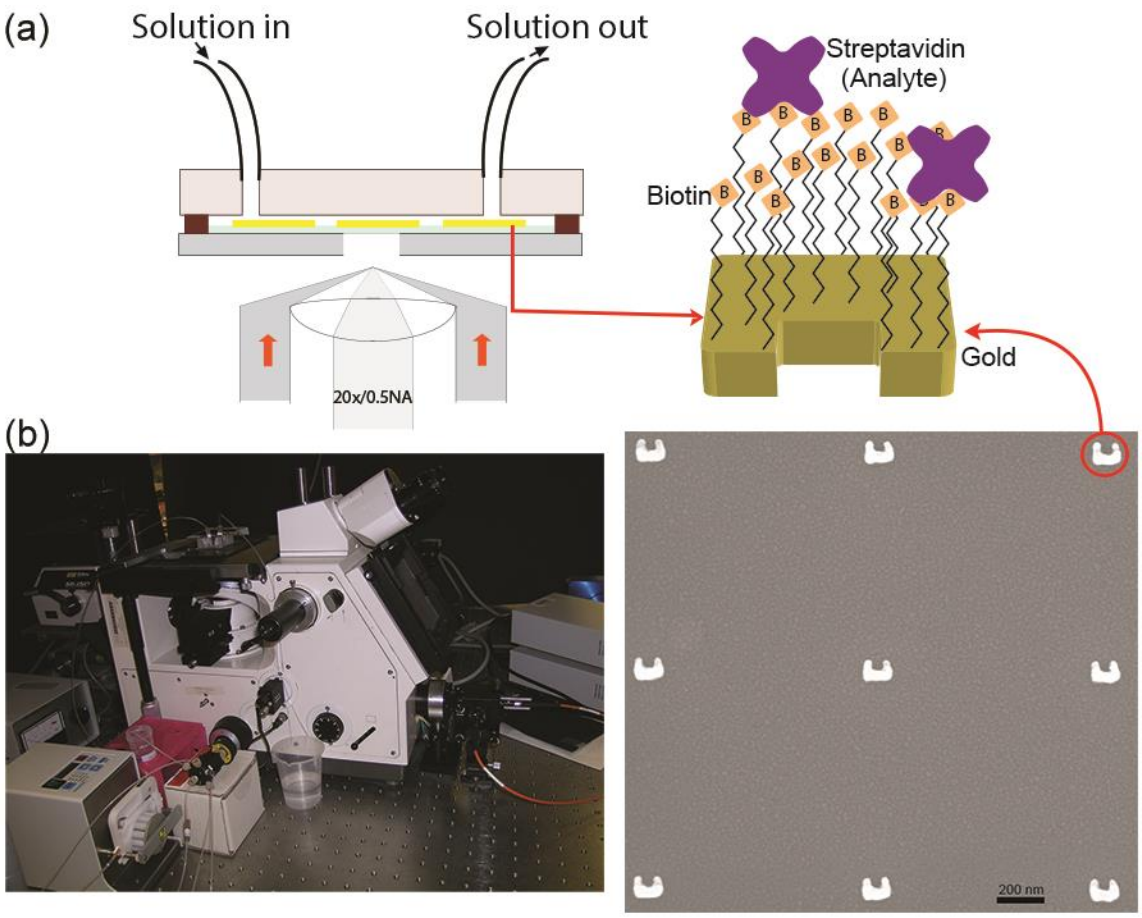

Figure 4.9 (a) Schematic of the custom made acrylic flow cell used for bio-sensing measurements. The biotin labeled sensor is clamped inside the flow cell and place on the microscope stage for measurements, and, (b) Image of the optical setup. SEM image in (a) consists of U-shaped nanostructure of size 125nm by 95nm with a gap size of 45 nm by 40nm. Pitch size of the array is 1μm.

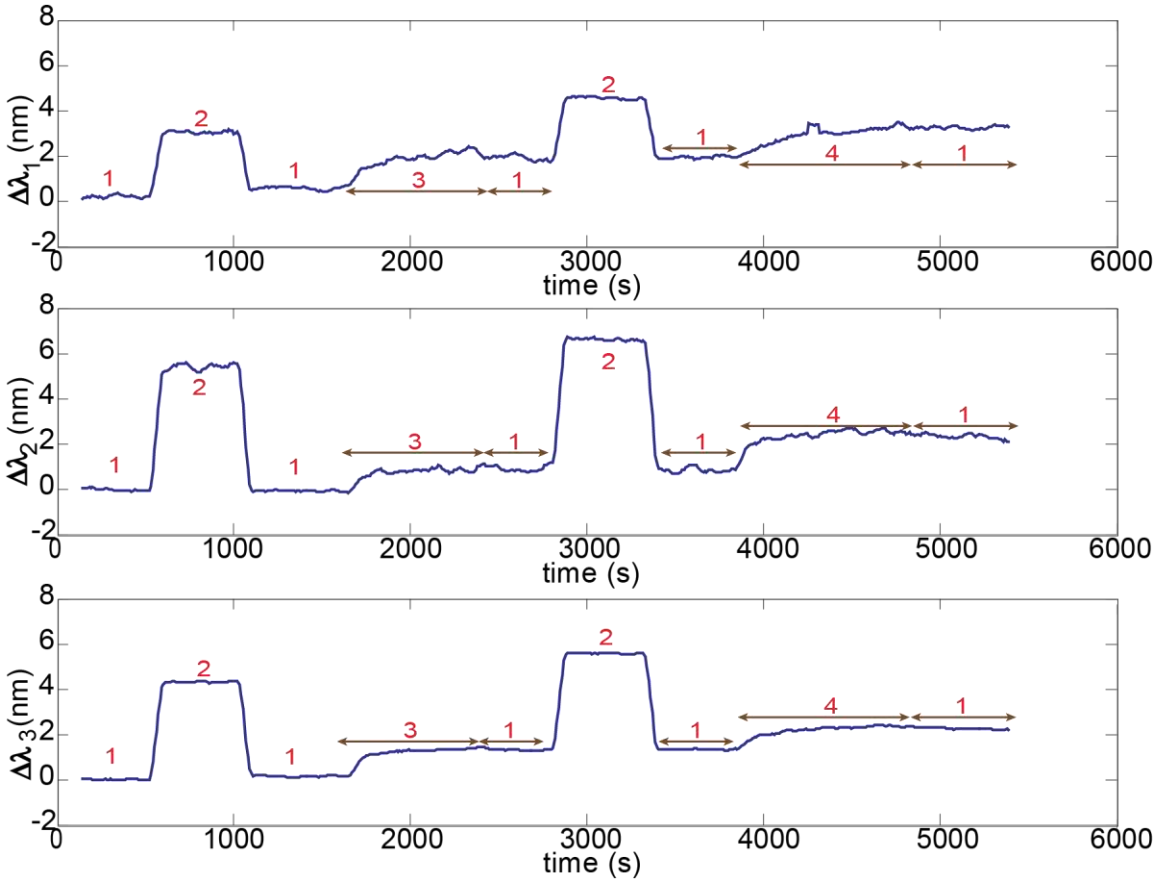

Figure 4.10 Relative shift in the three localized surface plasmon resonance modes of biotin functionalized U-shaped gold nanostructure to various specific and non-specific interactions. The solutions were introduced on the sensor surface in the following order – (1) 50mM Tris buffer, (2) buffer with 25% (w/v) glycerol, (3) buffer with 0.2 mg/ml streptavidin and (4) buffer with 5 mg/ml bovine serum albumin. Adapted from [163]

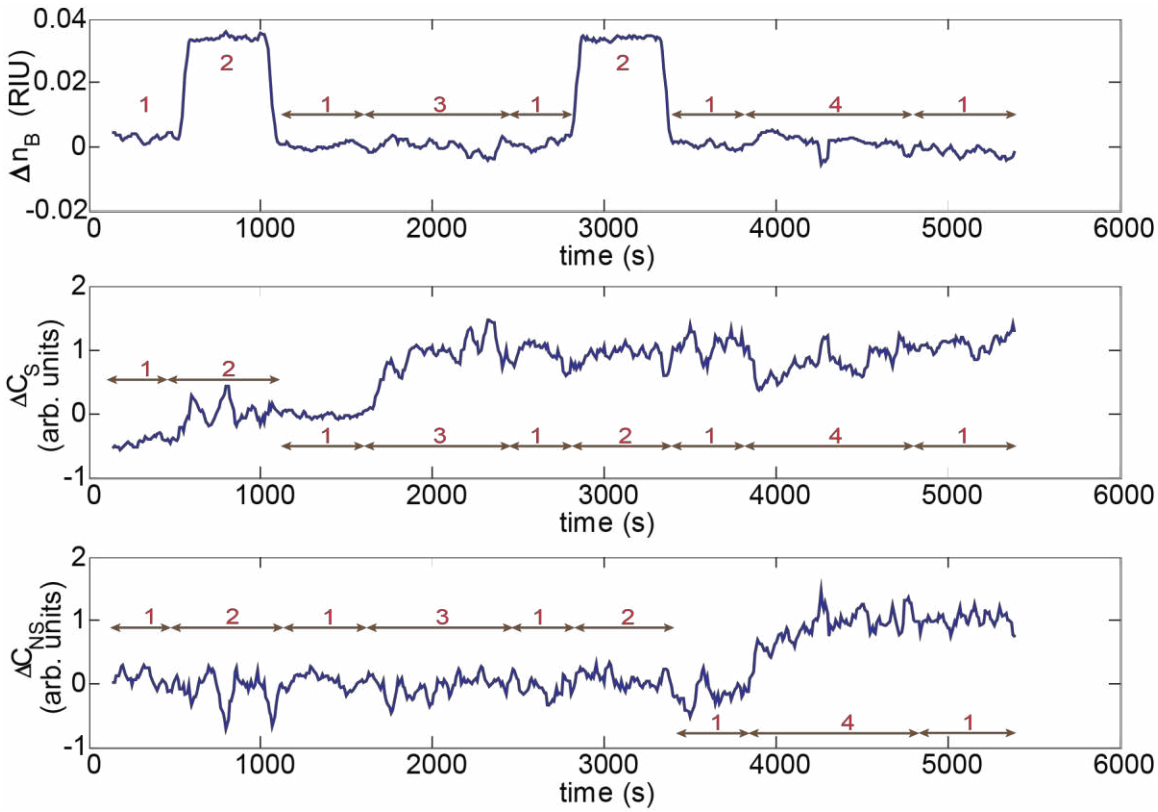

Figure 4.11 Calculated changes in (a) background refractive index, (b) specific surface concentration and (c) non-specific surface concentration with respect to time for U-shaped nanostructure sensor using the linear model described in (4.1). Solutions are indicated as follows – (1) buffer solution, (2) buffer with 25% (w/v) glycerol, (3) buffer with 0.2 mg/ml streptavidin and (4) buffer with 5 mg/ml bovine serum albumin. Adapted from [163]

Table 4.2 Sensing characteristics for the three resonances of a U-shaped gold nanostructure based sensor. Surface sensitivities are given in nm for complete surface coverage. Figure of merit (FOM) is the ratio of bulk sensitivity to resonance FWHM.

λ_{res}	Sensitivities			FOM
	Bulk (nm/RIU)	Surface: specific	Surface: non-specific	
λ_1 (670 nm)	70	1.5	1.2	2.3
λ_2(950 nm)	170	1.0	1.5	1.1
λ_3(770 nm)	120	1.2	1.0	1.5

The bulk refractive index sensitivity values for the U-shaped nanostructure based sensor are higher than those measured by Chen *et al.* [32] for a spherical nanoparticle (S_B=44 nm/RIU for a 15nm diameter particle) and nanocube (S_B=83 nm/RIU for a 44 nm edge length cube) based refractive index sensors. The FOM values of this sensor is comparable to the FOM value for a chemically synthesized single gold nanorod with an aspect ratio of ~3 (FOM=1.3) as reported by Mayer *et al*. [65]. The sensitivity values were also found to be similar to the recently reported values by Liu *et al*. [159] for their similarly sized complimentary split ring resonator (SRR) based sensor (S_B=210 nm/RIU) but lower than the sensitivity and figures of merit measured by Lai *et al*. [149] and Pryce *et al*. [150]. The marked difference in sensitivities and figures of merit between the similar shaped structures can be attributed to the difference in the size, and thus the resonance wavelengths, of the structures [50, 164]. The U-shaped nanostructures used in this experiments were scaled down in size to confine the three plasmon-resonance modes within the operating region of a typical visible to near-infrared grating spectrograph and

silicon CCD detector. As a result, they do not exploit the enhanced sensitivity at longer wavelengths that has been observed by Lai *et al*. and Pryce *et al*. for their SRR sensors.

4.4 Conclusion

In conclusion, arrays of U-shaped nanostructures that exhibit at least three resonances in the visible to near-infrared spectral region were fabricated using electron-beam lithography and optically characterized. The multi-mode sensor was tested for its self-referencing capability by simultaneously measuring shifts in the three resonances as different solutions, simulating a target interaction along with bulk and surface interference, were introduced. The three modes can compensate for changes due to interfering bulk and surface effects, allowing the target molecule to be detected separately. These multi-mode sensors were found to provide comparable sensitivities to other similar sized split ring resonator based refractive-index sensors along with the added benefit of complete separation of interfering effects.

Chapter 5

Numerical Analysis of Dual and Multi-mode sensors

5.1 Introduction

Finite element method is one of the many useful techniques to analyze arbitrary shaped structures in non-homogeneous media. This method involves the discretization of the total simulation volume into finite elements. It is often the method of choice to simulate large volumes that contain small feature sizes due to its ability to generate finer meshes in such regions [26]. FEM solves the scattering problem in frequency domain by discretizing the Helmholtz wave equation and solving numerically for fields that satisfy a set of boundary conditions [27, 28]. The discretized elements are generally made of non-Cartesian components (e.g., tetrahedral or triangular prism) that are chosen based on which element better approximates the scattering structure's boundary [165]. The size of each element is kept much smaller than the wavelength of incident light, typically less than $\lambda/5$ where λ denotes the wavelength of light in a particular medium. The size and shape of the mesh elements plays a very important role in the numerical modeling process [166]. The simulation domain is surrounded by a bounding box known as the perfectly matched layer (PML). This layer serves two purposes – to truncate the simulation domain and to prevent any spurious reflections from the boundary [27]. This is accomplished by ensuring that the wave incident on the PML layer experiences a zero reflection coefficient. COMSOL Multiphysics is one of the most widely used commercial software packages available for modeling complex two- and three-dimensional

electromagnetic problems. This chapter provides a simulation based analysis of the dual- and multi-mode sensing techniques examined previously through bio-sensing experiments.

The optical features as well as the sensing properties of complex nanoscale structures described in the following sections were calculated using the scattered field formulation available in the RF module of COMSOL 3.5a. The scattered field is calculated as the difference between a volume source field defined in the absence of a scatterer and the total field in the presence of the scatterer [23]. This method allows calculating the optical properties of nanostructures in one simulation step as opposed to two-step solution technique employed by other groups [22].

5.2 Dual mode sensor

As demonstrated in Chapter 3, one can utilize both the transverse and longitudinal modes of a gold nanorod to compensate for bulk interference and allow for an accurate measurement of the target analyte. To further test this theory, this section uses finite element modeling to study the effect of bulk and surface changes on a gold nanorod supported on a substrate.

5.2.1 Geometry & Field Formulation

A 1200 nm diameter spherical simulation domain was used to model the scattering from a gold nanorod on a 60 nm thick ITO coating supported by a glass substrate as shown in Figure 5.1(a). The simulation domain was subdivided into two halves to represent the substrate and the surrounding medium. The nanorod was modeled as a two dimensional elliptic cylinder with maximum lateral dimensions of 133 nm by 73nm extruded to a height of 30 nm into the simulation domain. This geometry matched the actual geometry

fabricated by lithography and liftoff, but neglected any slope in the sidewalls of the structure. The nanorod was placed such that the entire long axis is resting on the substrate. The substrate was defined using a constant refractive index for glass (n=1.5) while the spectral dependent refractive index of ITO was taken from the manufacturer's website [167]. Optical constants for gold were obtained from Johnson and Christy [33]. The entire simulation space was surrounded by a perfectly matched layer (PML) tailored to the refractive index of the adjacent sub-domain.

The source field is defined analytically as an infinite plane wave incident at an angle of θ_1 = 37° (the average angle of illumination of a Zeiss 20X dark-field objective) from within the substrate. Simple Fresnel coefficients for reflection and transmission are used to define fields everywhere within the domain (except the PML layer). Separate formulations and simulations were performed for both TE and TM polarized incident waves.

For a TE polarized wave incident on the substrate, the electric fields for each of the sub-domains in Figure 5.1 were defined in terms of its z-component. The following equation defines the incident field inside the 1st sub-domain, i.e., glass layer –

$$E_{z1} = A_1 e^{-jk_x x - jk_{y1}(y+l)} + A_{1r} e^{-jk_x x + jk_{y1}(y+l)} \tag{5.1}$$

where A_1 and A_{1r} are the amplitudes of the incident and reflected waves in sub-domain 1, k_x and k_{y1} are the wave vector components in the x- and y- direction and l is the thickness of the ITO layer (i.e., the 2nd medium). Similarly, E-fields in V/m for the other two mediums can be described as –

$$E_{z2} = A_2 e^{-jk_x x - jk_{y2}(y+l)} + A_{2r} e^{-jk_x x + jk_{y2}(y+l)} \tag{5.2}$$

$$E_{z3} = A_3 e^{-jk_x x - jk_{y3} y} \tag{5.3}$$

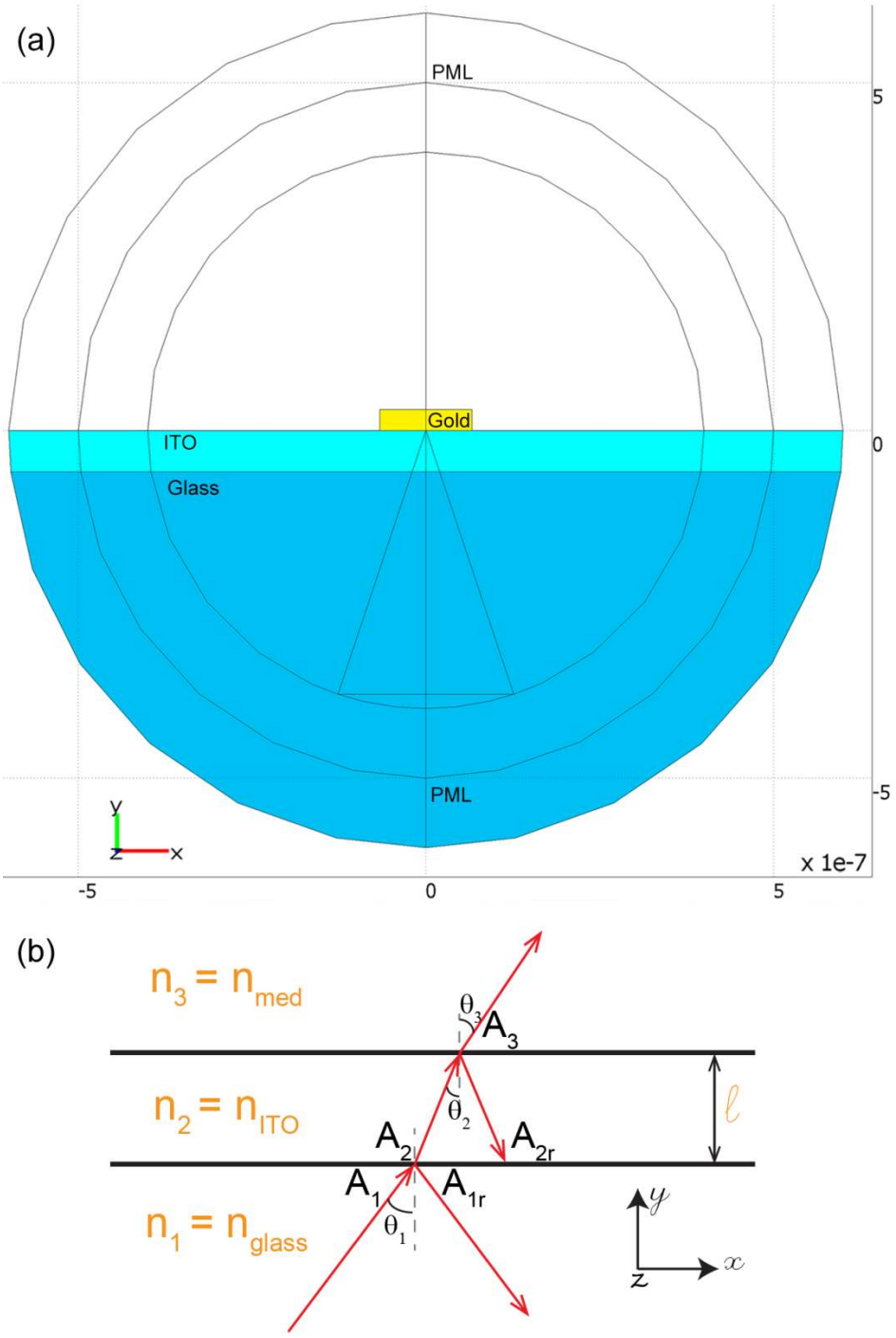

Figure 5.1 (a) Schematic of the spherical simulation domain used for the analysis of gold nanorods on ITO coated gold substrate, and, (b) a simplified 3-layer model used for calculation of various E-field amplitudes using Fresnel's equations and transmission matrix method.

Figure 5.1(b) displays the basic 3-layer schematic including the reflection and transmission amplitudes in each layer for simplified analysis. The various amplitudes in each of the three sub-domains for this multi-layer problem can be calculated using Fresnel's coefficients combined with transmission matrix analysis as follows [168] –

$$\begin{bmatrix} A_1 \\ A_{1r} \end{bmatrix} = \begin{bmatrix} \frac{1}{t_{12}} & \frac{r_{12}}{t_{12}} \\ \frac{r_{12}}{t_{12}} & \frac{1}{t_{12}} \end{bmatrix} \begin{bmatrix} A_2 \\ A_{2r} \end{bmatrix}$$

$$\begin{bmatrix} A_1 \\ A_{1r} \end{bmatrix} = \begin{bmatrix} \frac{1}{t_{12}} & \frac{r_{12}}{t_{12}} \\ \frac{r_{12}}{t_{12}} & \frac{1}{t_{12}} \end{bmatrix} \begin{bmatrix} e^{jk_{y2}l} & 0 \\ 0 & e^{-jk_{y2}l} \end{bmatrix} \begin{bmatrix} \frac{1}{t_{23}} & \frac{r_{23}}{t_{23}} \\ \frac{r_{12}}{t_{23}} & \frac{1}{t_{23}} \end{bmatrix} \begin{bmatrix} A_3 \\ A_{3r} \end{bmatrix} \quad (5.4)$$

Solving the above matrices results in the following amplitude values –

$$A_{1r} = A_3 \left(\frac{r_{12} e^{jk_{y2}l}}{t_{12} t_{23}} + \frac{r_{23} e^{-jk_{y2}l}}{t_{12} t_{23}} \right) \quad (5.5)$$

$$A_2 = \left(\frac{A_1 - r_{12} A_{1r}}{1 - r_{12}^2} \right) t_{12} \quad (5.6)$$

$$A_{2r} = \left(\frac{r_{12} A_1 - A_{1r}}{r_{12}^2 - 1} \right) t_{12} \quad (5.7)$$

$$A_3 = \left(\frac{A_1}{e^{jk_{y2}l} + r_{12} r_{23} e^{-jk_{y2}l}} \right) t_{12} t_{23} \quad (5.8)$$

The incident amplitude at the glass/ITO interface, A_1 is assumed to be 1 V/m. The amplitude of the reflected wave in the third medium will be zero, i.e., $A_{3r} = 0$, due to the absence of any interface beyond that sub-domain. r_{12} and t_{12} are the reflection and

transmission coefficients at the interface between 1st and 2nd mediums (glass and ITO here), r_{23} and t_{23} are the respective coefficients for interface between 2nd and 3rd domains (ITO and dielectric media). These coefficients can be calculated using Fresnel equations-

$$r_{12} = \frac{n_1 cos\theta_1 - n_2 cos\theta_2}{n_1 cos\theta_1 + n_2 cos\theta_2} \tag{5.9}$$

$$t_{12} = \frac{2n_1 cos\theta_1}{n_1 cos\theta_1 + n_2 cos\theta_2} \tag{5.10}$$

where n_1 and n_2 are the refractive indices of the 1st and 2nd medium and θ_1 and θ_2 are the angle of incidence within medium 1 and 2 respectively. Replacing 1&2 with 2&3 in (5.9) and (5.10) will generate formulations for r_{23} and t_{23} respectively. The angle of incidences in medium 2&3 can be easily calculated using Snell's Law –

$$\theta_2 = \sin^{-1}\left(\frac{n_1 sin\theta_1}{n_2}\right)$$
$$\theta_3 = \sin^{-1}\left(\frac{n_2 sin\theta_2}{n_3}\right) \tag{5.11}$$

The tangential components of wave-vector defined as $k_x = k_0 n_1 sin\theta_1$ where k_0 is the wave-vector in free space, is continuous across the interface and therefore, will be same in all the three layers. The y-component, on the other hand, varies between the layers and is calculated as $k_{yi} = k_0 n_i cos\theta_i$, where i = 1,2 or 3.

It should be noted that the field formulations defined above are only valid for a TE polarized wave. For the case of TM (transverse magnetic) wave analysis, in-plane components of the electric field are utilized to define the source fields inside each medium. For the model described in Figure 5.1, the source field for TM mode is defined

using both the E_x (V/m) and E_y (V/m) components. E-fields inside the 1st medium are defined as–

$$E_{x1} = cos\theta_1\left(A_1 e^{-jk_x x - jk_{y1}(y+l)} - A_{1r} e^{-jk_x x + jk_{y1}(y+l)}\right)$$
$$E_{y1} = -sin\theta_1\left(A_1 e^{-jk_x x - jk_{y1}(y+l)} - A_{1r} e^{-jk_x x + jk_{y1}(y+l)}\right) \quad (5.12)$$

Here θ_1 is still the angle of incidence, l the thickness of the ITO layer and A_1 and A_{1r} are the incident and reflected field amplitudes in 1st medium as defined in (5.5). However, the reflection and transmission coefficients are altered for TM polarization to –

$$r_{12} = \frac{n_2 cos\theta_1 - n_1 cos\theta_2}{n_1 cos\theta_2 - n_2 cos\theta_1}$$
$$t_{12} = \frac{2n_1 cos\theta_1}{n_1 cos\theta_2 - n_2 cos\theta_1} \quad (5.13)$$

Similarly, the E-fields for medium 2 and 3 are defined as –

$$E_{x2} = cos\theta_2\left(A_2 e^{-jk_x x - jk_{y2}(y+l)} - A_{2r} e^{-jk_x x + jk_{y2}(y+l)}\right)$$
$$E_{y2} = -sin\theta_2\left(A_2 e^{-jk_x x - jk_{y1}(y+l)} - A_{2r} e^{-jk_x x + jk_{y2}(y+l)}\right) \quad (5.14)$$

$$E_{x3} = cos\theta_3\left(A_3 e^{-jk_x x - jk_{y3} y}\right)$$
$$E_{y3} = -sin\theta_3\left(A_3 e^{-jk_x x - jk_{y3} y}\right) \quad (5.15)$$

After defining fields everywhere except the PML layer, the next step in the computational analysis involves the discretization of the simulation domain into smaller elements. Different mesh sizes were used for different sub-domains with the smallest element size and densest mesh around the volume of the nanorod (i.e., around the region of high field gradient). Figure 5.2 shows the relative meshing density of the simulation domain used in the analysis. The number as well as the size of the mesh used in the analysis was tested against a set of higher and lower parameters and chosen based on

convergence and reduced computational time. Further details regarding this process can be found in [169].

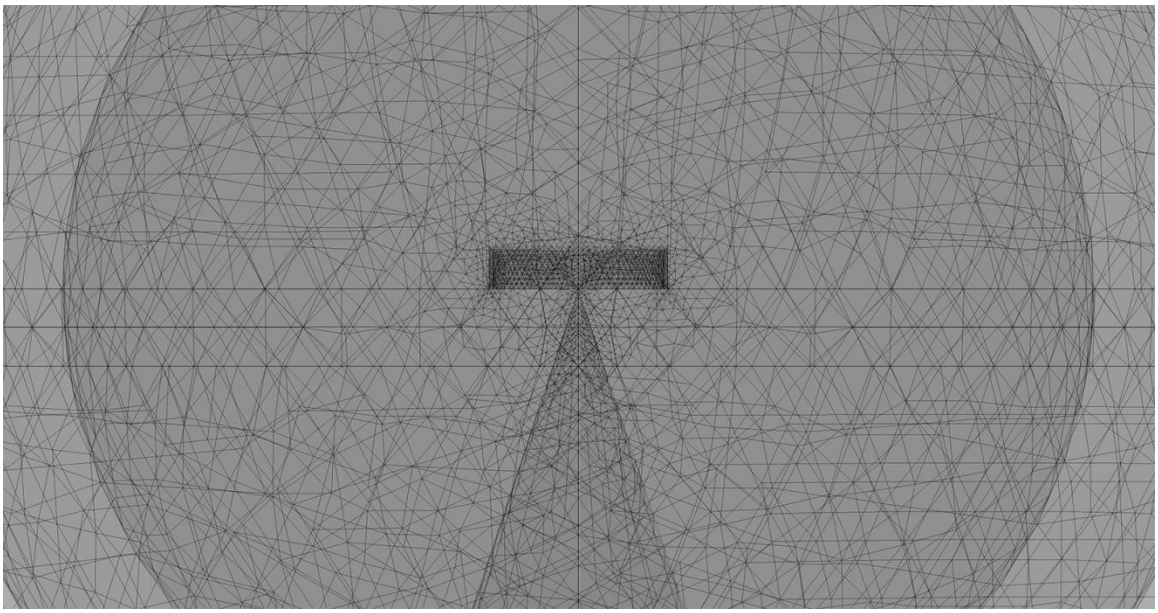

Figure 5.2 Zoomed in view of the spherical simulation domain exhibiting distinct mesh sizes in different regions of the model.

The scattering cross-section, C_{sca} (m^2) is obtained by integrating the Poynting vector for the scattered field over the boundary of the glass substrate defined by the numerical aperture of a 20X dark-field objective with a collection half angle (θ_{col}) of 19° ($n\sin\theta$ = N.A., where n=refractive index of glass) –

$$C_{sca} = 2 * nscPoav/P_0 \tag{5.16}$$

where P_0 (W/m^2) is the incident flux defined as $P_0 = 0.5A_1^2 c\varepsilon_0 n_1$, A_1 and n_1 are the amplitude of the incident electric field and the refractive index of the incident medium respectively, c is the speed of light in vacuum and ε_0 is permittivity of free space. The *nscPoav* in the above equation is the scattered normal flux defined as –

$$nscPoav = onx * scPoxav + ony * scPoyav + onz * scPozav \quad (5.17)$$

scPoxav, *scPoyav* and *scPozav* are the x, y and z-components of the scattered flux. They can be calculated as $scPoxav = 0.5 * Re(scE_y \times scH_z^* - scE_z \times scH_y^*)$ and so on for the other terms. The *onx*, *ony* and *onz* in the equation are intrinsic COMSOL variables used to calculate the direction of vector for each component of the scatter flux.

These simulations were validated against Mie theory and by confirming that the scattered field is approximately zero in the absence of a nanorod. References [23, 169] provide a more detailed analysis of the validation techniques employed to assess the accuracy of the numerical model. Figure 5.3 displays the scattering spectra of 133nm by 73nm gold nanorod in TE and TM mode obtained using the simulation domain described above. Based on its position on the substrate, the TE mode represents the transverse resonance of the nanorod while the TM mode represents its longitudinal mode.

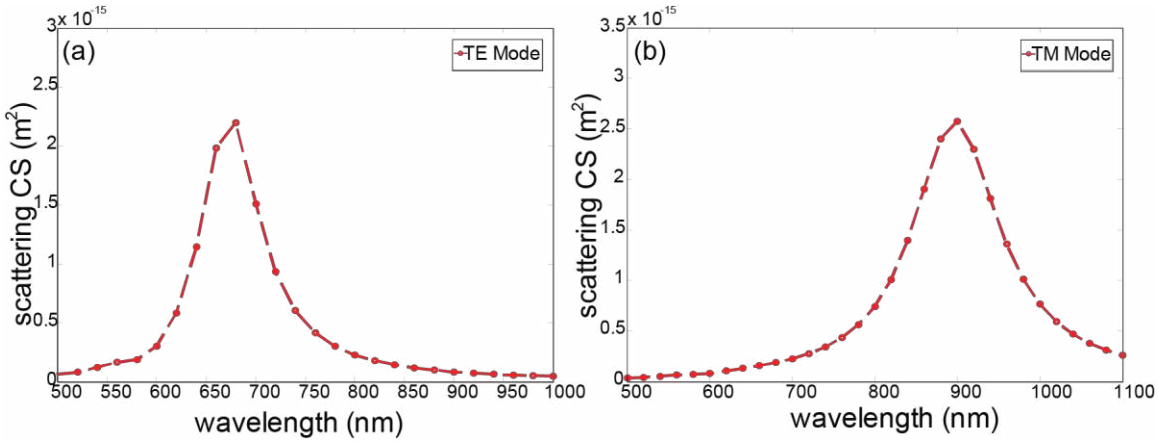

Figure 5.3 Calculated scattering cross-section for the (a) TE mode, and, (b) TM mode of the incident electric field from gold nanorod of size 133nm by 73nm on ITO coated glass substrate with n_{med} =1.33.

5.2.2 Biosensing Simulation Setup

For bio-sensing simulations, the refractive index of the medium was set to match the refractive index value of a typical buffer solution (n=1.33), the most widely used background solution for biological experiments. The gold nanostructure surface was functionalized by a adding a 3 nm thin layer over its surface. The thickness and refractive index value of the functionalized layer was matched to the value of an alkanethiol functionalized with biotin, a very common recognition element used for the detection of streptavidin [170]. To model the change in the background solution index, the refractive index of buffer solution was increased by a factor of 0.068 RIU (refractive index units) and the scattering spectrum was recalculated. To determine the specific surface sensitivity, a thin layer (thickness = 5 nm and n = 1.45) simulating the widely used protein streptavidin was added over the gold nanostructure surface. Figure 5.4 demonstrates the regions around the sensor altered in order to simulate the bulk as well as the specific effects.

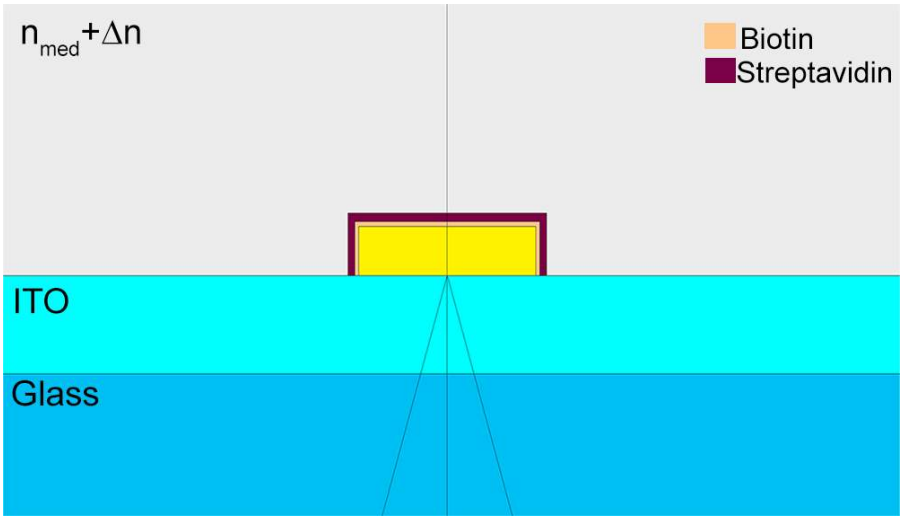

Figure 5.4 Schematic displaying the different areas modified to calculate the effect of bulk and surface changes on the gold nanorod based dual-mode sensor.

Figure 5.5 shows the calculated scattering spectra obtained due to changes in bulk refractive index and surface coverage using the gold nanorod sensor. The longitudinal and transverse resonances shift by different amounts with surface and bulk interactions and thus can help differentiate the two effects. Table 5.1 shows the bulk and surface sensitivities (assuming complete surface coverage) for the two modes calculated using the above model. The shifts were estimated by fitting a 2nd degree polynomial to the scattering spectra. A figure of merit (χ) for a dual mode sensor is proportional to the difference between the ratios of bulk and surface sensitivities, where $\chi \equiv |S_{BL}/S_{BT} - S_{SL}/S_{ST}|$ [134]. A larger figure of merit indicates lower cross-sensitivity, and better differentiation between the two effects. The bulk and surface sensitivity ratios and figure of merit for the nanorod based dual mode sensor were calculated to be 3.7, 2.6 and 1.0 respectively.

Table 5.1 Calculated bulk and surface sensitivities for the longitudinal and transverse modes of gold nanorod.

	Bulk Sensitivity (nm/RIU)	Surface Sensitivity (nm for complete coverage)
Transverse Mode (TEmode)	54	2.2
Longitudinal Mode (TM mode)	200	5.8

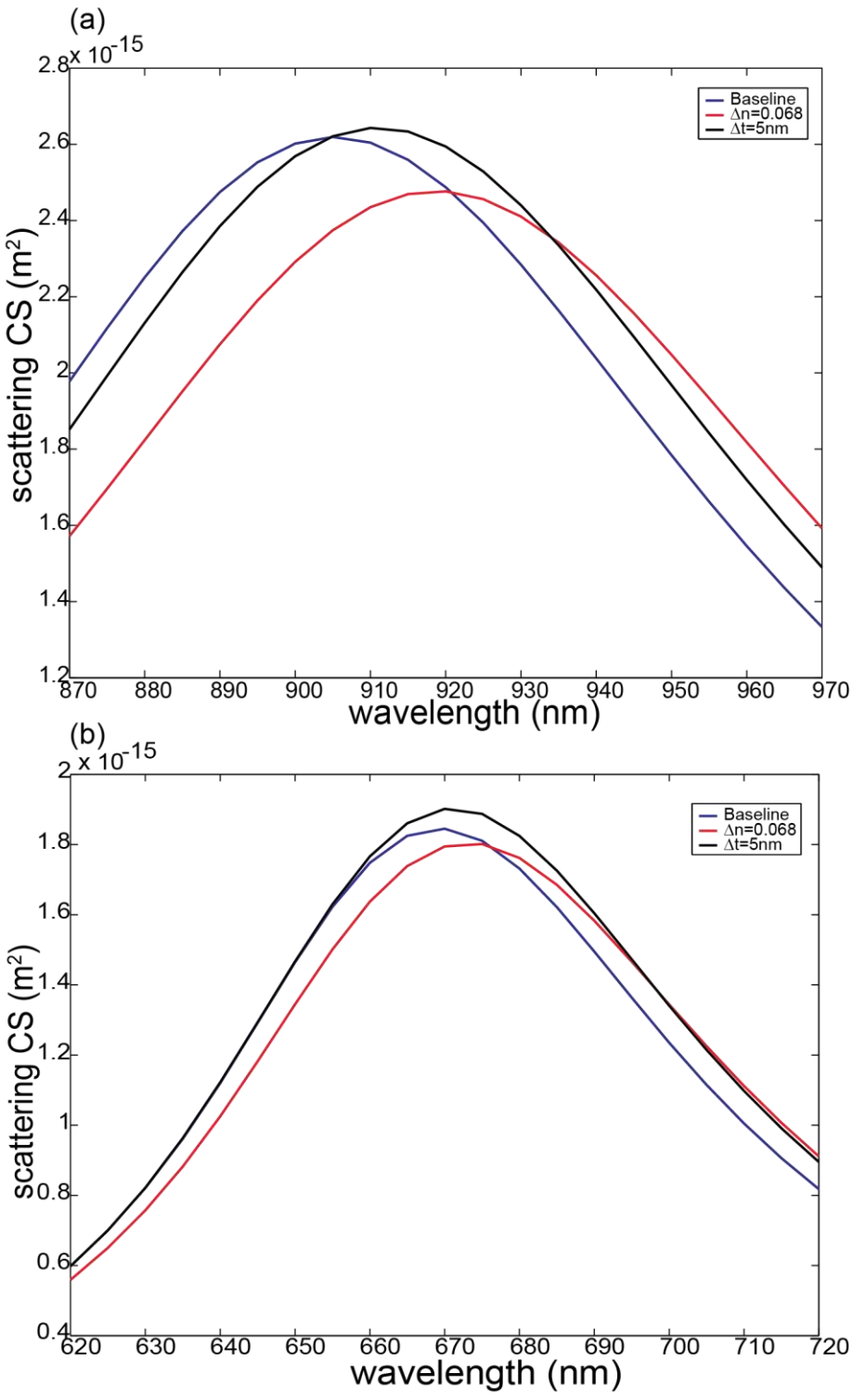

Figure 5.5 Calculated shifts in the (a) transverse or TE mode, and, (b) longitudinal or TM mode for a gold nanorod based sensor due to either a change in solution index of 0.068 or adsorption of a 5nm thick layer.

The results obtained from the above simulation are in close approximation to the sensitivities and figure of merit values obtained from the biosensing experiment in Chapter 3. The minor difference (within 35%) between the two can likely be attributed to various experimental details not accounted for in the simulation, including the surface roughness and optical absorption of the ITO coating on the glass substrate, the non-ellipsoidal cross-section and vertically tapered sidewalls of the gold nanorod, and possibly non-uniform coating of the biotin and streptavidin layers on the surface of the sensor.

5.3 Multi-mode sensor

Following the experimentally reported findings on the multi-mode sensing capability of the U-shaped nanostructure based sensor in Chapter 4, this section provides a numerical study of the nanostructure, evaluates its electric field profiles and assesses its sensitivities to specific and non-specific surface and bulk effects.

5.3.1 Geometry and Field formulation

The scattering from the U-shaped gold nanostructure on an indium tin oxide (ITO) coated glass substrate was modeled using an 800 nm Cartesian computational simulation domain as illustrated in Figure 5.6. The domain was further subdivided into two halves to represent the substrate and the surrounding medium. The U-shaped nanostructure of dimension ℓ_x =107nm, ℓ_y =94nm, w_g =40nm, d_g =38nm was modeled in 2-D and then extruded to a height of 20 nm into the 3-D domain. The entire simulation domain was truncated using a 150 nm absorbing perfectly matched layer (PML) to prevent back reflections. The design and dimensions of the nanostructure was chosen to closely match the values obtained experimentally through electron beam lithography.

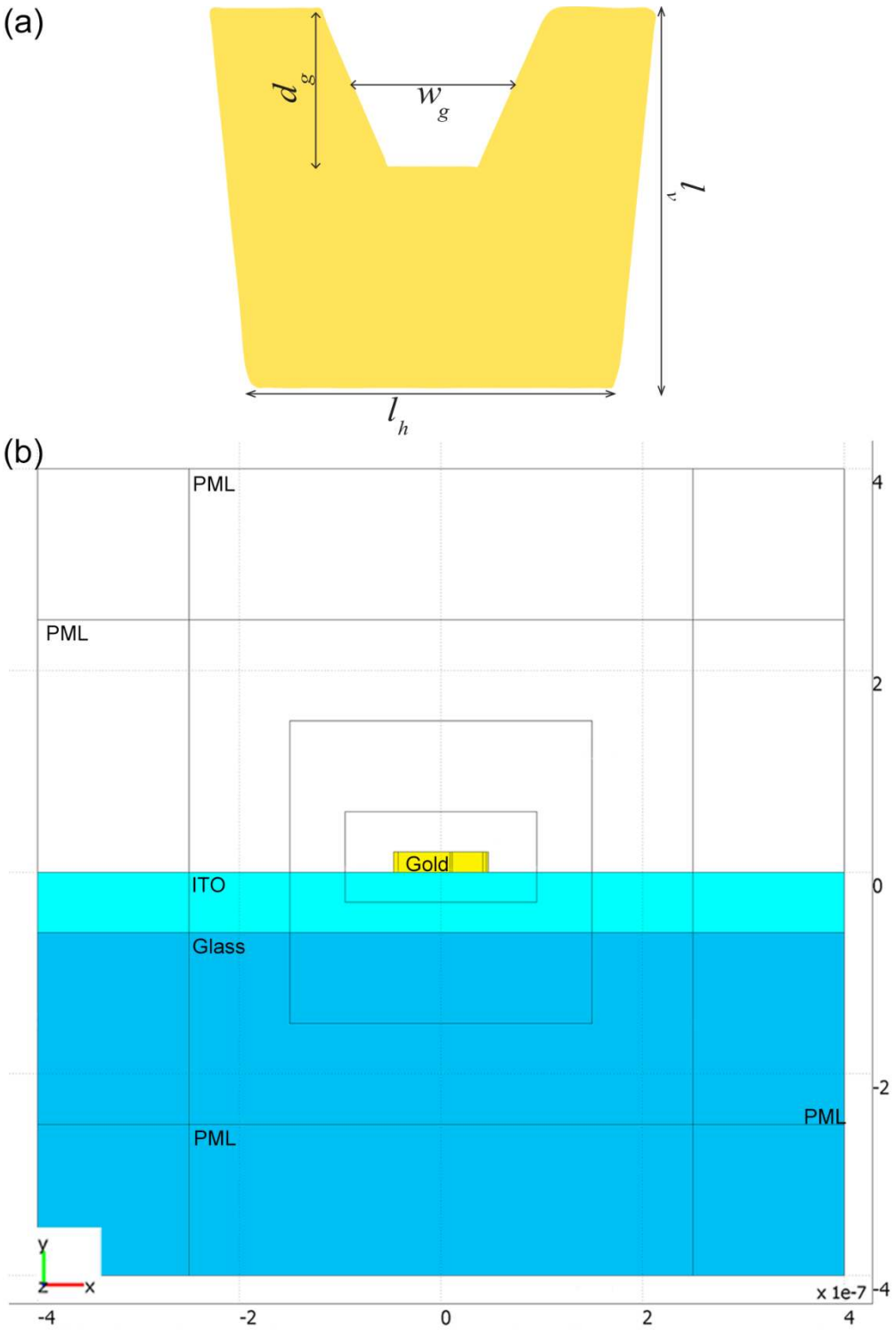

Figure 5.6 (a) Schematic of the U-shaped gold nanostructure, and, (b) Cartesian simulation domain used for numerical analysis of U-shaped gold nanostructures on ITO coated glass substrate.

Refractive index values of the different materials were taken from a variety of sources. The gold nanostructure was modeled using the refractive index values obtained from Johnson and Christy [33]. Optical constants for the ITO layer were obtained from SPI Supplies website [167]. The refractive index values for BK7 glass was kept constant at n=1.5 throughout the entire spectral wavelength range. Once again, the refractive index values for the PML layer were chosen to match the refractive index of its adjacent subdomain.

The U-shaped gold nanostructure was excited using a plane wave incident at an angle of θ_1=37° from within the substrate. The source fields were defined analytically throughout the volume of the simulation domain (except the PML layer) using the same equations as described in 5.3.1 for both the TE and TM polarization modes. The TE mode was defined using equations (5.1), (5.2) and (5.3) for the three sub-domains; while the TM mode was defined using equations (5.12), (5.14) and (5.15) respectively. The scattering spectrum was similarly obtained by integrating the Poynting vector (5.16) for the scattered field over the boundary of the glass substrate defined by θ_{col} = 19°. The angles for light incidence and collection were once again chosen to include the effect of a realistic 20X dark-field microscope objective with a N.A. of 0.5. The simulations were validated by confirming that the scattered field is approximately zero in the absence of the gold nanostructure. The same validation methods described previously were used to confirm the validity of the Cartesian simulation domain [169].

Figure 5.7 displays the TE and TM polarized scattering spectra obtained from a U-shaped gold nanostructure on an ITO coated glass substrate with buffer solution (n_{med}=1.33) as the surrounding medium. Based on the position of the nanostructure within

the simulation domain, the incident electric field in the TE mode is parallel to the gap (w_g) within the nanostructure and exhibits two surface plasmon modes.

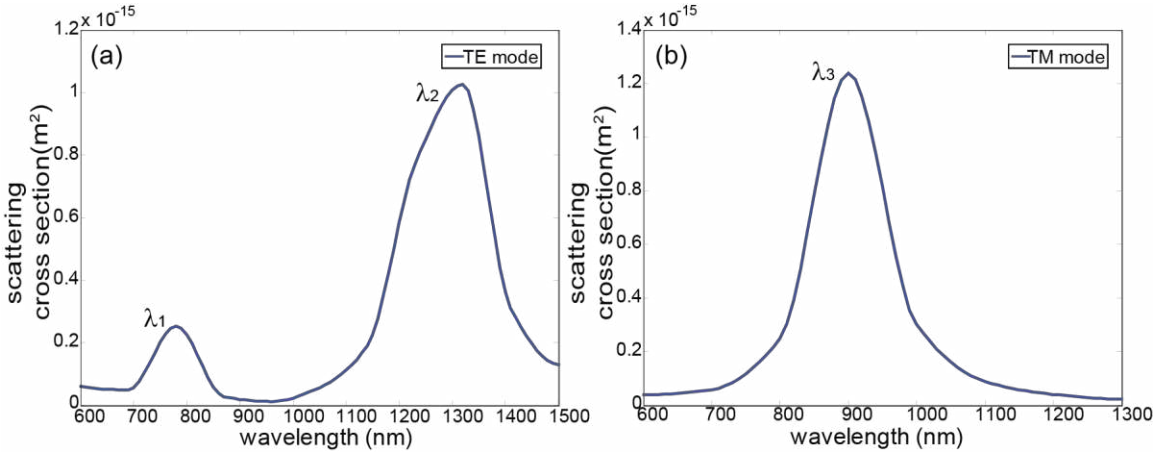

Figure 5.7 (a) TE mode, and (b) TM mode scattering spectrum from a U-shaped gold nanostructure on an ITO coated glass substrate calculated using COMSOL with n_{med}=1.33.

The normalized electric field intensity ($\sqrt{E_x E_x^* + E_y E_y^* + E_z E_z^*}$) for the three localized surface plasmon resonance modes of the U-shaped nanostructure was also calculated using COMSOL. Figure 5.8 shows the cross-sectional plot of the E-fields taken 10 nm above the gold surface through the x-z plane. It can be clearly seen that the three plasmon modes of the U-shaped nanostructure on an ITO substrate separately localize the E-fields at different regions on the sensor surface. This allows the specific and non-specific effects, that occur at different regions on the sensor surface, to be easily distinguished.

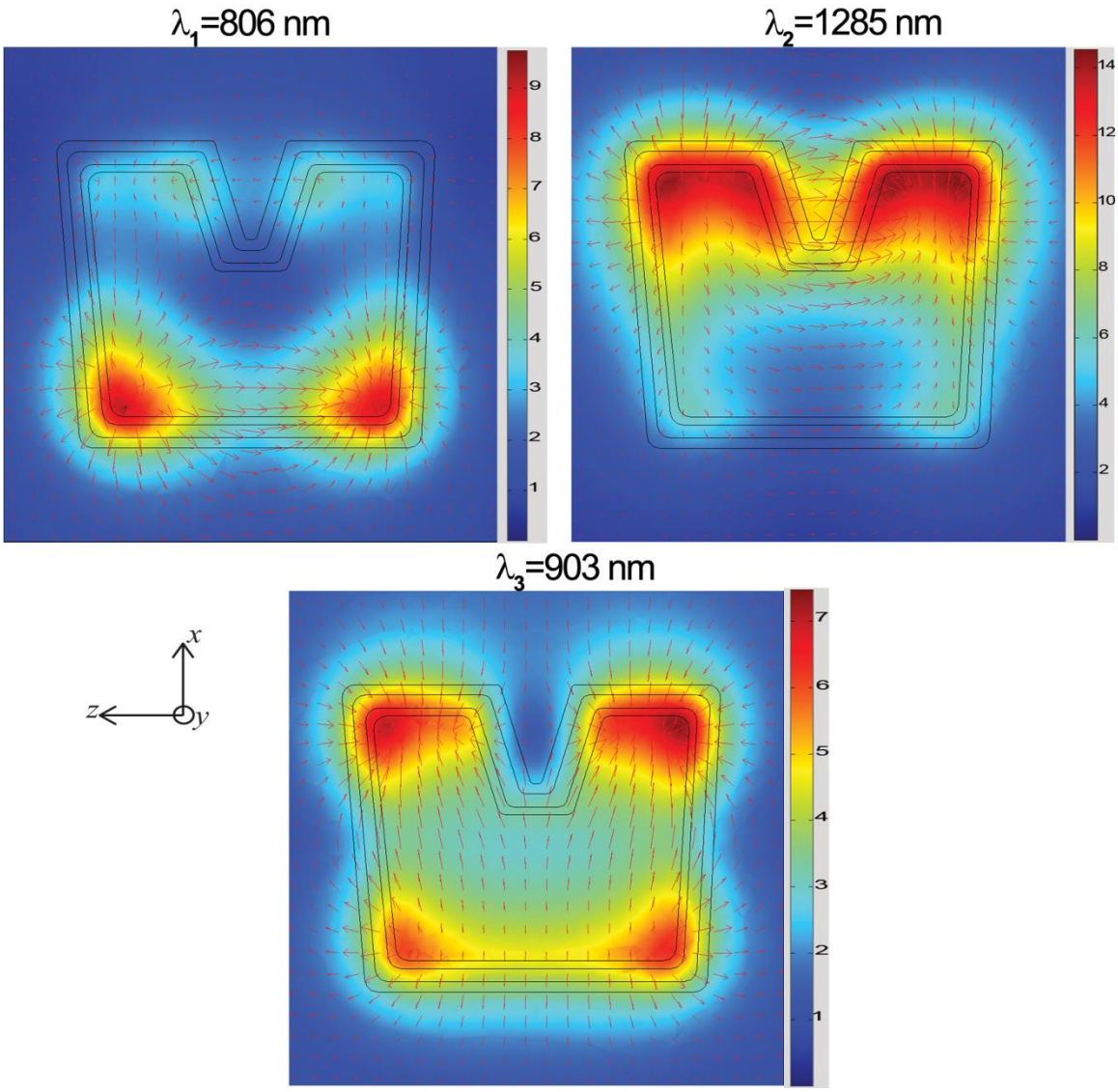

Figure 5.8 Cross sectional plot of the normalized electric field for the three surface plasmon modes of the U-shaped nanostructure based sensor. The slice is taken from x-z plane at 10 nm above the gold surface. The arrows show the normalized electric field at a particular point in time. The colors show the norm of the electric field (with a scale of V/m). Since the incident wave has an amplitude of 1V/m, the norm of the electric field directly corresponds to the field enhancement.

5.3.2 Biosensing Simulation Setup

The simulation model was further altered to study the multi-mode biosensing characteristics for the U-shaped structure by modeling the well-studied biotin-streptavidin binding interaction. Similar modifications, as described in Section 5.2.2, were made to model bulk and specific surface binding characteristics of the U-shaped sensor. To reiterate, first the gold surface was functionalized by adding a 3 nm thin layer simulating an alkanethiol functionalized with biotin over its surface. To study the bulk effects of the sensor, the refractive index of the medium was increased by a factor of 0.03404 RIU (due to the addition of 25% (w/v) glycerol to buffer). The specific surface binding effects were determined by adding a 5 nm thin layer with a refractive index of 1.45 (simulating streptavidin) over the sensor surface. Similarly, to determine the non-specific surface sensitivity, a 4 nm thin layer imitating bovine serum albumin (BSA, n=1.45) was added over the entire sensor surface (including both gold and the ITO).

Figure 5.9(d) demonstrates the regions around the sensor altered in order to simulate the bulk as well as the specific and non-specific surface effects. As streptavidin strongly binds to the biotin coated gold surface, the effect of specific surface interaction was simulated by adding a thin layer only around the functionalized gold nanostructure surface [170]. Similarly, an interfering molecule like BSA will bind non-specifically to both the gold and ITO surfaces; thus, to simulate the effect of such an interaction, a thin layer was added all over the gold as well as the ITO surface. The scattering cross-section was recalculated for each change made in the simulation domain.

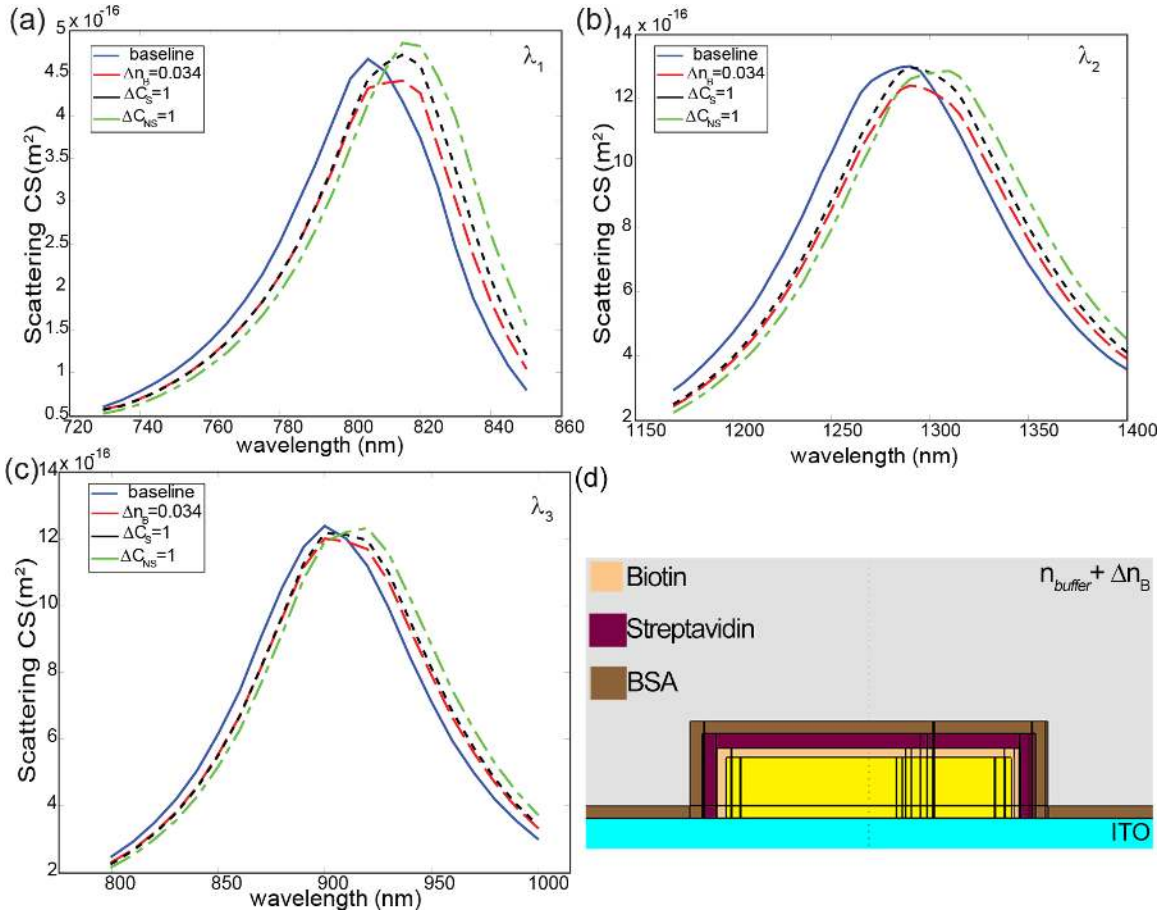

Figure 5.9 (a), (b), (c) Shifts in the three localized surface plasmon resonances of the U-shaped nanostructure to bulk index change (Δn_B), specific surface binding (ΔC_S) and non-specific surface binding (ΔC_{NS}), and, (d) zoomed in view of the simulation domain showing the perturbed regions for sensitivity analysis.

Figure 5.9 displays the calculated scattering spectra obtained from the TE and TM polarized modes of the U-shaped nanostructure based sensor to changes in the bulk refractive index of the surrounding medium, specific binding of the target analyte and non-specific binding of interfering molecule. As seen in the figure, the three resonances shift by different amounts with various surface and bulk effects and thus can help resolve the three effects. The U-shaped gold nanostructure sensor was characterized by calculating its bulk sensitivity as well as specific and non-specific surface sensitivities.

The linear bulk sensitivity of a sensor is defined as the ratio of shift in the resonance wavelength ($\Delta\lambda_i$) to the change in the refractive index of the bulk solution (Δn_B). The specific and non-specific surface sensitivities are defined as the change in resonance wavelength to a unit change in the surface coverage of the adsorbed target analyte and interfering molecule respectively. Table 5.2 lists the various bulk and surface sensitivities for the three surface plasmon modes of the U-shaped structure based sensor. The bulk sensitivities calculated using the simulation model were found to be slightly higher than the values obtained from the experiments. This difference in sensitivity values can be attributed to the various experimental details not accounted for in the simulation including the surface roughness of the ITO and gold surface and vertically tapered sidewalls of the gold nanostructure.

Table 5.2 Sensing characteristics of the U-shaped nanostructure based sensor. Surface sensitivities are given in nm for complete surface coverage.

	λ_1(~806nm) (nm)	λ_2(~1285nm) (nm)	λ_3(~903nm) (nm)
Bulk (S_B) (nm/RIU)	150	260	180
Specific Surface (S_S)	6.8	9.6	7
Non-specific Surface (S_{NS})	10	17	11

5.4 Conclusions

This chapter presented a numerical study on the spectral response of both gold nanorod and U-shaped gold nanostructure on an indium tin oxide coated glass substrate. In particular, the ability of these nanostructures as reference compensated dual- and multi-mode sensors was studied. It was observed that the various localized surface plasmon

modes of the nanorod and U-shaped nanostructure exhibit different sensitivities to bulk as well as specific and non-specific surface effects. This allows the sensor to compensate for changes due to interfering interactions and allow the surface binding of the target analyte to be measured separately

Chapter 6

Sensing Characteristics of U-shaped Nanostructure based Biosensor

6.1 Background

Chapter 4 provided a proof-of-concept analysis on the multi-modal sensing capabilities of a U-shaped gold nanostructure based sensor. Known concentrations of target and interfering species were introduced onto the sensor surface and the shifts induced due to each interaction were recorded in real-time. The three surface plasmon modes of the gold nanosensor displayed different sensitivities towards the various specific and non-specific effects allowing the differentiation between the various interactions. However, a complete characterization of the various plasmon modes of the sensor to the bulk and surface effects is necessary in order to measure unknown concentrations of target analyte in complex solutions. This chapter outlines our work done to date in characterizing the various resonances of the multi-mode sensor for bulk as well as specific and non-specific surface sensitivities.

Figure 6.1 displays a standard SPR sensorgram that plots the response of a sensor to the target molecules in real time. A typical sensogram for an antigen-antibody interaction process consists of three major steps – association, disassociation and regeneration [171, 172]. The first two steps, i.e., association and disassociation, together define the response of a sensor to target molecules in solution. The regeneration step prepares the sensor for further bio-sensing interactions by removing any bound target molecule from the ligand coated sensor surface. A good regeneration solution is an important part of the biosensing

experiment as it defines the life cycle of a particular sensor. An efficient regeneration solution should be able to remove the target molecules while avoiding any loss in ligand activity for future antigen interactions [173]. Consequently, figuring out an optimized regeneration solution is an important part of the sensor design and characterization process.

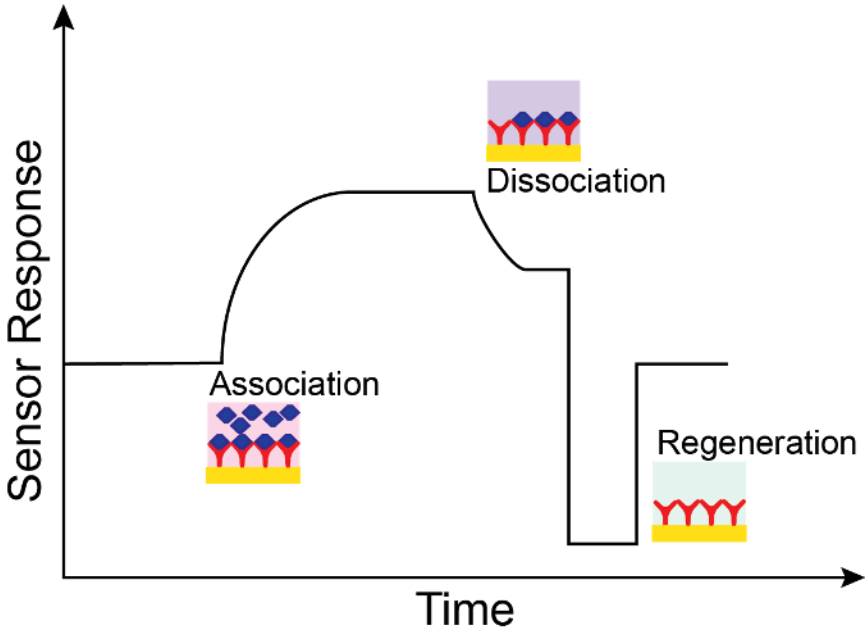

Figure 6.1 An example sensogram displaying a typical response of an SPR sensor with time.

The biosensing experiments described in the previous chapters utilize the well-known biotin-streptavidin binding interaction as a model to test the self-referencing capability of the U-shaped gold nanosensors. However, the extremely high binding affinity of streptavidin to biotin molecule makes it almost impossible to elute from the sensor surface using any of the recommended regeneration conditions [174]. The high rate of association ($\sim 10^{15}$ M^{-1}) would also make any possible regeneration process a very time

consuming one [175]. Therefore, a more extensive investigation of the sensor characteristics would warrant a change from the current assay to a different biochemical interaction that allows easy regeneration. Immunoglobulins are one such protein molecule that are as widely used instead of the biotin-streptavidin system to study the affinity characteristics of a sensor [65].

Immunoglobulins (Ig) are glycoprotein molecules that bind specifically to certain antigens through a lock-and-key mechanism. Of all the different Igs, Immunoglobulin G (IgG) is the smallest, most common antibody present in high concentrations in human serum. Figure 6.2 illustrates the Y-shaped structures of an IgG molecule. It consists of two light chain and two heavy polypeptide chains joined together through disulfide bonds [176]. Each IgG antibody molecule contains two antigen binding sites in its Fab portion. Depending on its orientation, an IgG antibody can utilize one or both sites for antigen binding interaction. The binding characteristics of IgG antibody-antigen interaction have been widely reported through the SPR sensing technique [65, 177, 178]. The binding affinities of IgG are not as strong as the biotin-streptavidin molecule and hence, are a perfect replacement for when a kinetic analysis of the sensor is required. The biosensing experiment in this chapter utilizes the binding capabilities of IgG molecules to study the sensing characteristics of the U-shaped nanostructure.

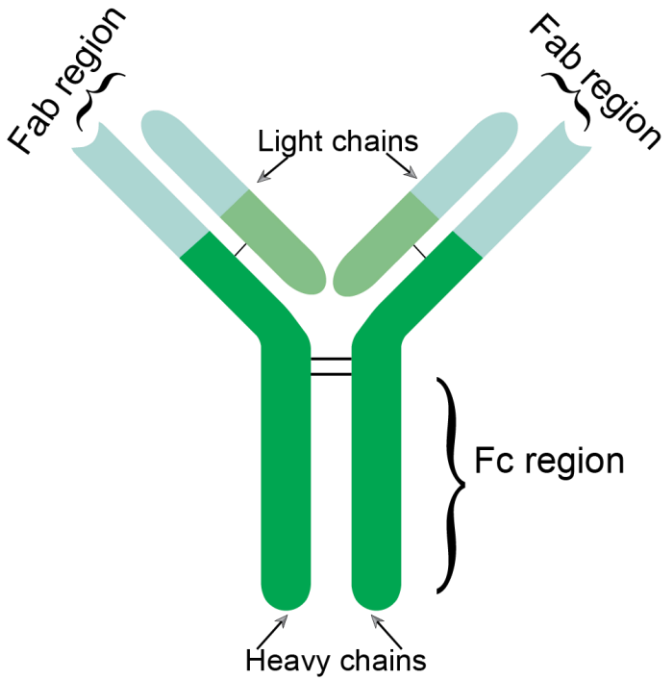

Figure 6.2 Schematic of an IgG molecule.

6.2 Sensor Fabrication

The steps utilized in the fabrication of U-shaped gold nanostructure based sensor are the same as described in the Section 4.2. ITO coated glass substrate spin coated with a positive electron beam resist (PMMA) was exposed to a high energy (30keV) beam of electrons. The developed sample was coated with a thermally evaporated 20 nm thin gold layer followed by removal of any undeveloped PMMA by soaking the substrate in a hot NMP solution for 2-6 minutes. Figure 6.3(a) displays an SEM image of the sensor.

Similarly, the previously described optical setup was used for characterizing the U-shaped gold nanostructures. Briefly, a 20X dark-field objective fitted within an inverted microscope was used for both illuminating the sensor surface as well as collecting light scattered from the gold nanostructures. The unpolarized scattered light was polarized

with the help of a cube polarizer and the two polarized beams were spectrally dispersed and measured individually using a grating spectrograph and a thermoelectric cooled CCD camera. The spectra from the nanostructures were normalized to scattering from the bare ITO substrate. Figure 6.3(b) shows the normalized scattering spectra of an array of U-shaped nanostructures.

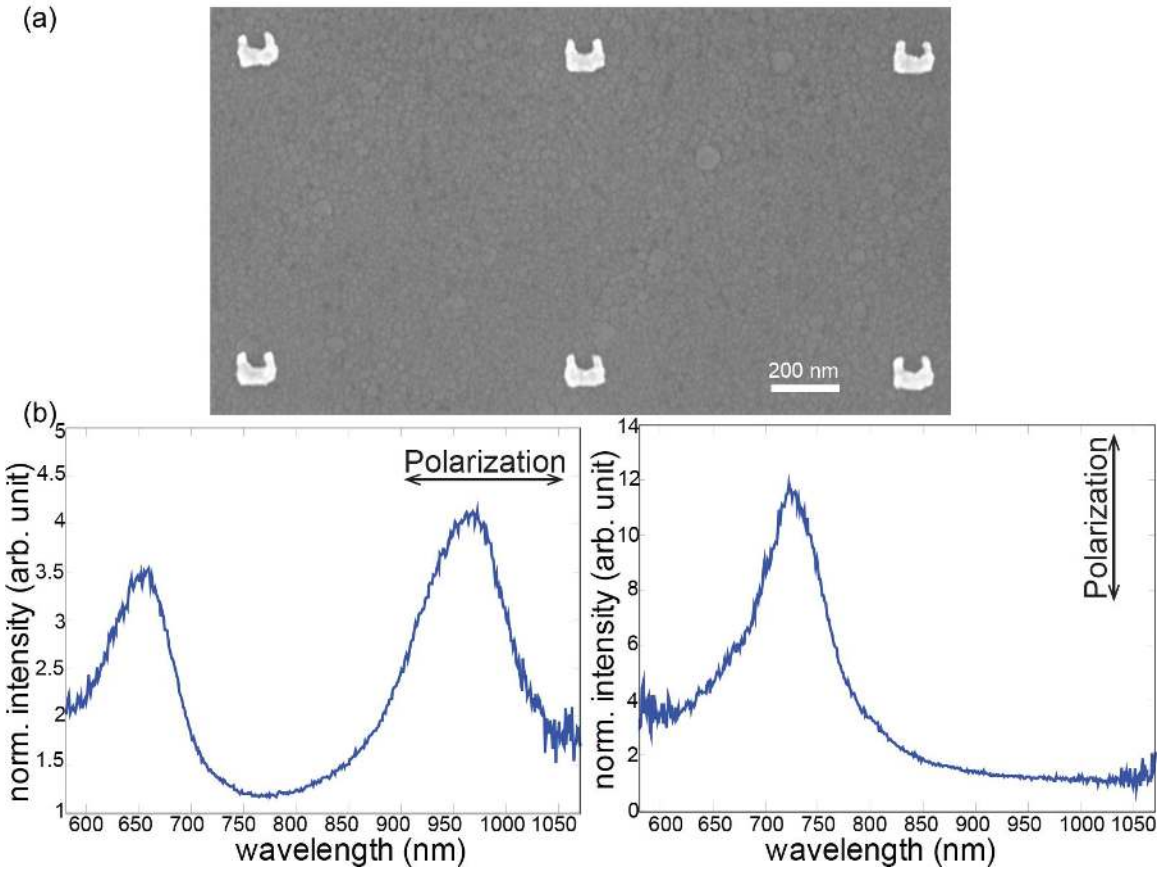

Figure 6.3 (a) SEM image of an array of U-shaped nanostructures on an ITO surface with dimensions ℓ = 115nm, ℓ_y = 97nm, w_g = 53nm and d_g = 48nm, and, (b) its corresponding scattering spectrum.

6.3 Biosensing Experiment

This section outlines, in chronological order, the steps taken to characterize the U-shaped gold nanostructure based sensor for bulk and surface interactions using IgG antibody-antigen binding interaction. All the steps in the following experiments, except SAM immobilization were performed inside the flow cell. Phosphate buffer saline (PBS) solution is used as a baseline for the entire biosensing experiment, except as otherwise stated.

6.3.1 Materials

11-Mercaptoundecanoic acid (MUA), 1-Ethyl-3-(3-dimethylaminopropyl)- carbodiimide (EDC), N-Hydroxysuccinimide (NHS), Ethanolamine hydrochloride and Glycine-hydrochloride were purchased from Sigma Aldrich (St. Louis, MO). Human IgG, Goat Anti-Human IgG (H+L) and Protein A were purchased from Pierce Biotechnology (Rockford, IL). Phosphate buffered saline (PBS) 10X buffer, 2-[n-morpholino] ethanesulfonic acid (MES) buffer, Glycerol, Sodium dodecyl sulfate (SDS), Hydrochloric acid (HCl) and sodium hydroxide pellets (NaOH) were obtained from Fisher Scientific (Pittsburg, PA).

6.3.2 Surface Preparation

Various methods exist to functionalize a metal nanoparticle based sensor surface with ligand molecules for biosensing applications. The most widely used technique involves the covalent binding of the antibody molecule to the gold surface thorough an intermediate SAM layer. This method produces a more stable functionalized surface that can withstand harsh regeneration conditions without the loss of any ligand activity. The

presence of a densely packed SAM molecule also reduces the effect of non-specific adsorption on the sensor surface [179].

Prior to any surface functionalization, the sensor was thoroughly cleaned by immersing the substrate in solutions of acetone, IPA and DI water for 5-10 minutes respectively, followed by an oxygen plasma clean for 3-5 minutes to remove any organic contaminants. The substrate was then immersed overnight in a 10mM solution of 11-MUA in ethanol to form self-assembled monolayer (SAM) on gold surface. The sensor is then washed with copious amounts of ethanol and DI water followed by drying under N_2 gas. MUA is a carboxylic acid terminated alkanethiol widely used as a linker molecule to attach biological molecules on the metal surface [180]. As seen in Figure 6.4(a), the thiol end of MUA binds to the sensor surface due to its strong affinity to gold, leaving the carboxylate groups free at the other end of the surface. To covalently bind the anti-hIgG molecules, the carboxylate groups were first activated using a freshly prepared mixture (1:1 volume ratio) of 200mM EDC and 100mM NHS in MES buffer. The solution was allowed to sit on the sensor surface for approximately 30 minutes before washing the surface with PBS buffer. As seen in the figure, the EDC molecule reacts with the carboxylate group to form an unstable reactive ester that further reacts with N-hydroxysuccinimide to form partially stable NHS ester groups. The primary amine groups present in ligand molecules react with NHS ester to form a partially stable covalent amide bond [181]. Post activation, the sensor is exposed to anti-hIgG antibodies in PBS buffer for another 30 minutes before washing the surface with buffer solution.

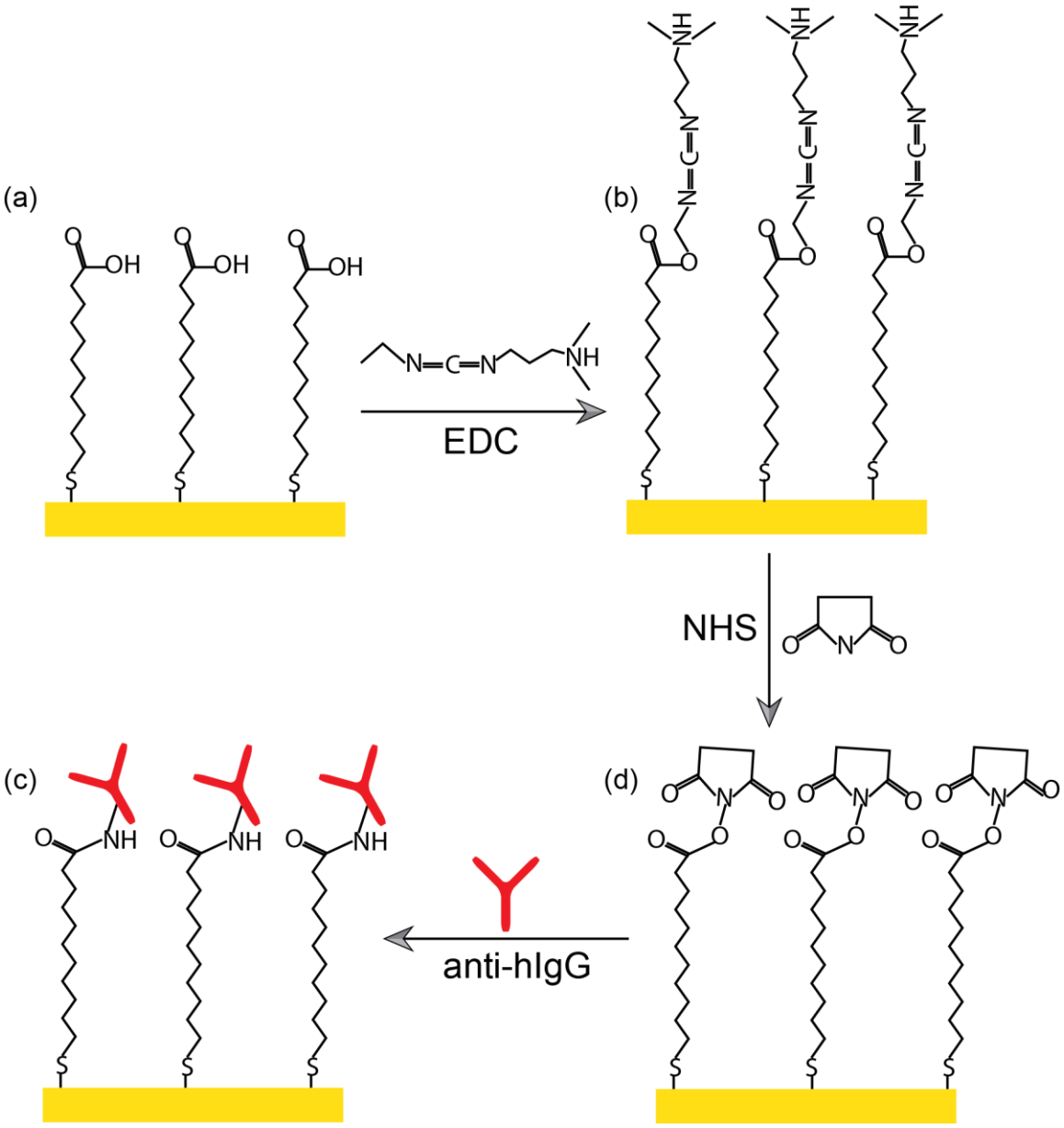

Figure 6.4 EDC/NHS coupling chemistry for the covalent binding of ligand molecules on the sensor surface.

6.3.3 Bulk RI sensitivity

The sensitivity of the plasmon modes of U-shaped gold nanostructure to changes in bulk refractive index was measured by introducing solutions with different refractive index values on the sensor surface and measuring the shifts in its resonances. The buffer solution was modified by adding glycerol in various concentrations to change the background refractive index from 1.33 (no glycerol) to 1.38 (40% glycerol). Figure 6.5 plots the shifts in the resonances versus time with changing bulk RI values. The buffer solution is used as the baseline for the experiment and introduction of increasing refractive index solution results in increasing red-shifts of the resonance wavelengths. Figure 6.6 shows the linear shift in the three resonances over a range of RI bulk changes.

6.3.4 Regeneration Scouting

As explained earlier, a regeneration step is performed to remove analytes from the sensor surface and prepare the sensor for further measurements. This step is usually performed with solutions that are harsh enough to break the antigen-antibody bond including, among other, acidic, ionic and basic solutions. This section outlines the results of the various regeneration solutions examined for the U-shaped nanostructure assembled on an ITO coated glass substrate. Table 6.1 also provides a summarized version of all the regeneration conditions tested for the U-shaped nano-biosensor.

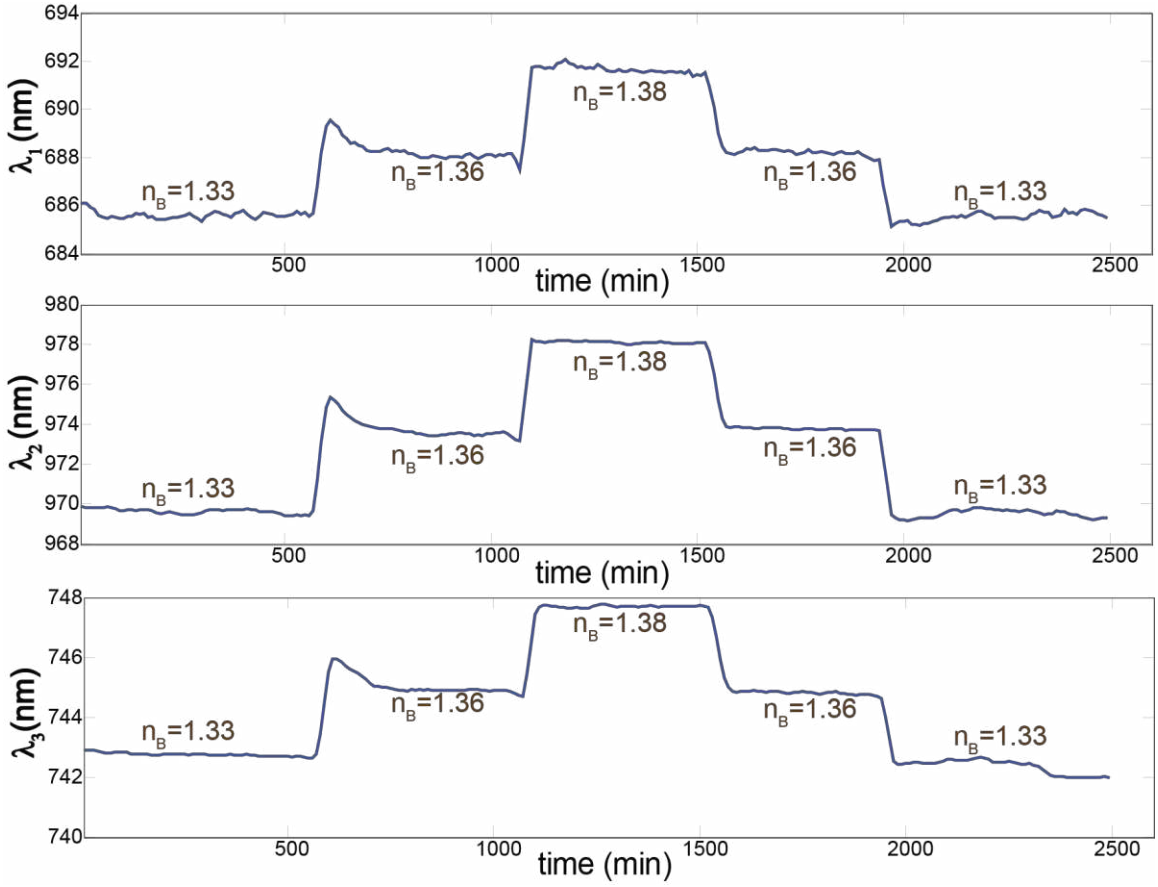

Figure 6.5 Shift in plasmon resonances of U-shaped gold nanostructure measured in increasing concentrations of glycerol in buffer solution.

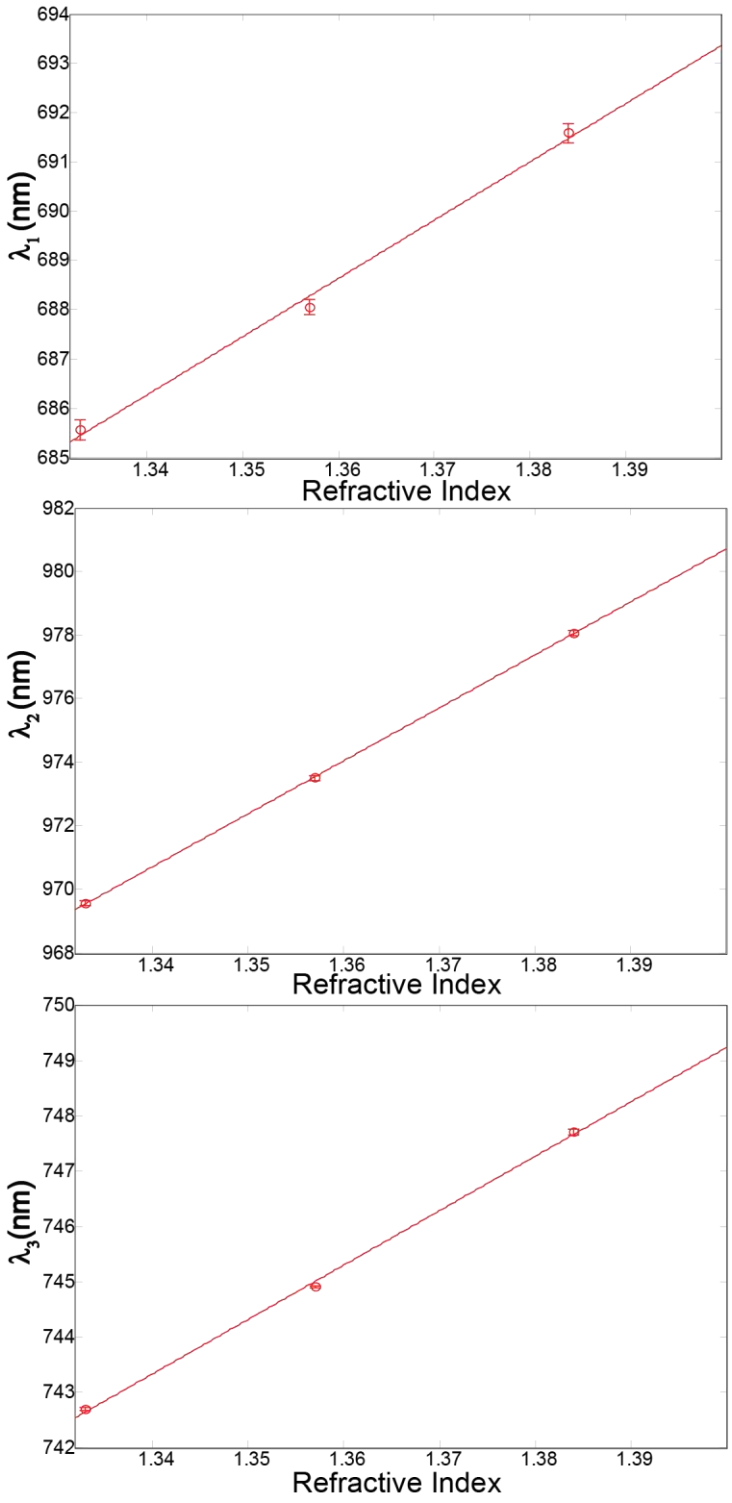

Figure 6.6 Bulk sensitivity characterization for the three resonances of the nanosensor with error bars indicating one standard deviation.

6.3.4.1 Acidic Solution

Acidic solutions are the most widely used regeneration assays for nearly every ligand-target interaction [182]. Therefore, a glycine-HCl solution was first used as the regeneration solution to test for its efficacy with the U-shaped nanostructure based sensor. Figure 6.7 plots the plasmon resonance (λ_2) as a function of time as 10mM glycine-HCl solutions with varying pH values are entered into the flow cell post the antigen-antibody interaction process. As seen in the figure, point labeled *a* denotes the introduction of EDC/NHS mixture into the flow cell. Point labeled *b* indicate the addition of anti-hIgG as the ligand molecule and *c* denotes the addition of ethanolamine to block any unused ester sites. Point *d* denotes the arrival of target antigen solution on the sensor surface and the shift in the resonance indicates the binding interaction. After washing the surface with PBS, 10mM glycine-HCl with a pH value of 5 and 4 are introduced onto the sensor surface at steps *e* and *f* respectively. Reintroduction of the buffer post pH 4 solution causes the resonance to shift back its base position before the introduction of target analyte. However, reintroduction of target hIgG at point labeled *g* did not induce the same shift as seen previously. Furthermore, introducing glycine-HCl solution at pH=3 results in a sharp drop in the resonance to values even below the baseline as seen in *h*. Reintroduction of target molecules beyond this point (not shown in the figure) induced no changes in the resonance. Similar drops in wavelength positions were observed for all the other plasmon resonances as well. Repeating the same experiment with different concentrations and pH values of glycine-HCl solution had the same effect on the resonances of the sensor.

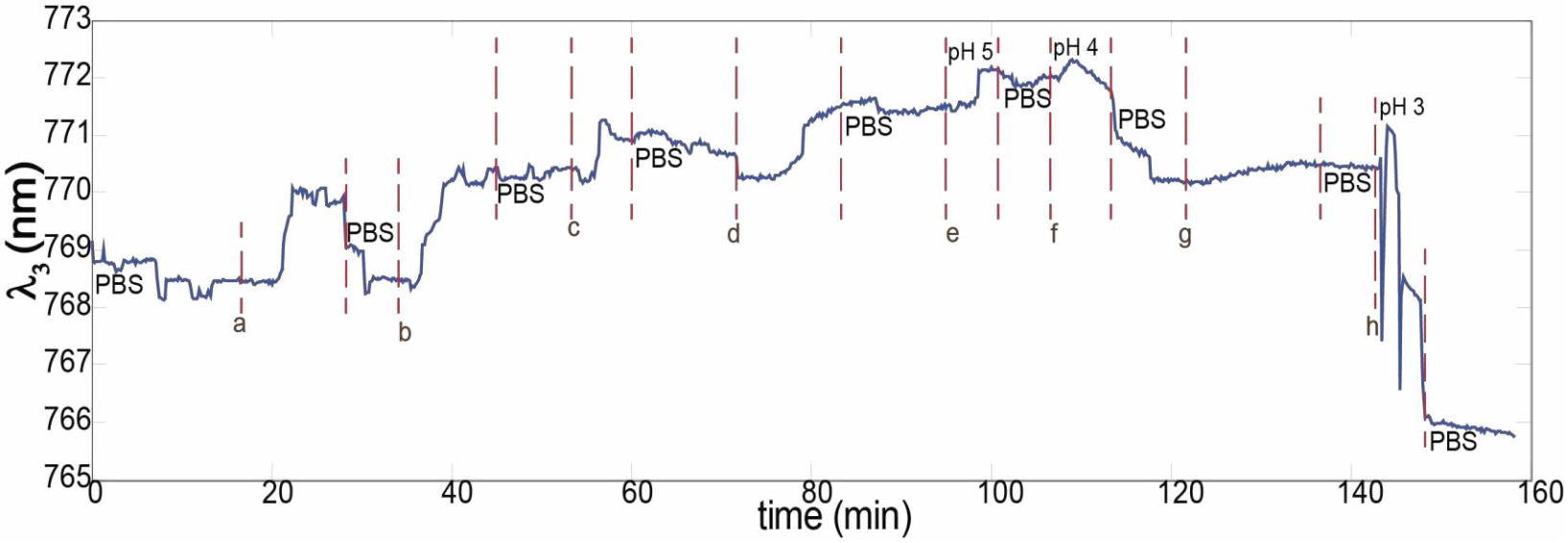

Figure 6.7 Shifts in λ_3 versus time showing the effect of acidic solutions as regeneration assay for the biosensor.

As the presence of acidic solutions on the sensor surface ruin the sensing analysis by causing the resonances to shift to unknown positions, it was postulated that the low pH conditions were somehow negatively affecting the sensor. Figure 6.8 shows the SEM image of the sensor after an HCl based solution was placed on its surface for a couple of hours. Compared to the SEM shown in Figure 6.3(a), it can be clearly seen that the presence of HCl has completely removed the ITO layer from the glass surface. A thorough literature review revealed that HCl based solutions act as an etchant for the ITO layer causing it to etch at a rate of 8 Å/sec [183]. Therefore, acidic based regeneration solutions were found to be incompatible for sensors built on ITO substrates.

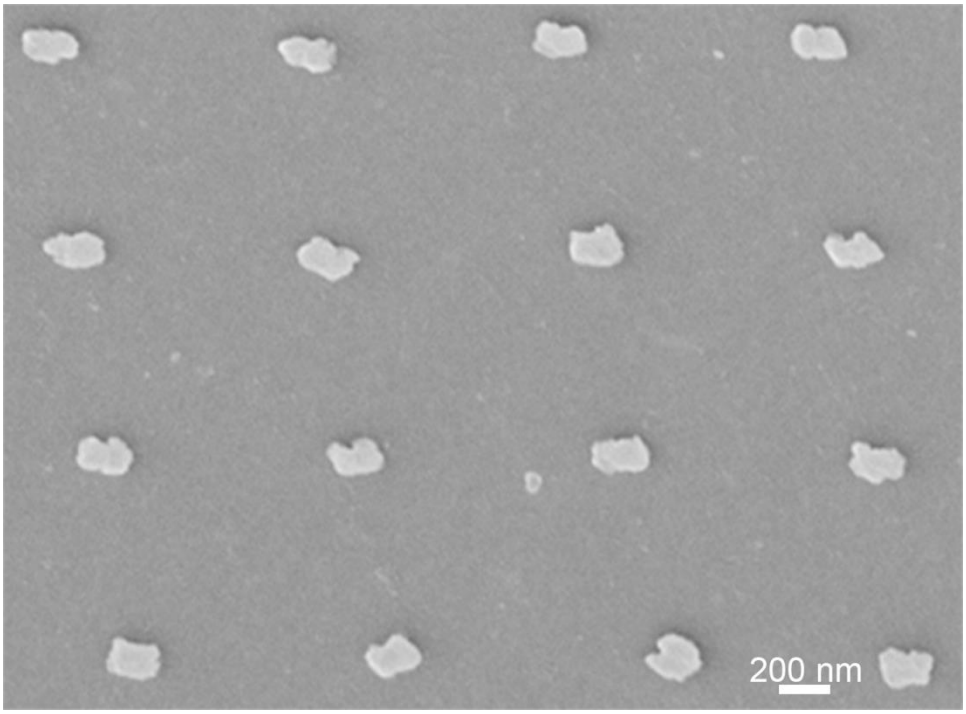

Figure 6.8 SEM image showing the effect of acidic solutions on the sensor surface. The presence of low pH assay caused a complete etch of the ITO surface as seen by the absence of any grainy structure in the image.

6.3.4.2 Ionic solution & Detergents

After demonstrating that low pH solutions are not ideal for regenerating sensors built on ITO substrates, other combination of solutions were tested to provide an optimal regeneration assay. Ionic solutions like KCl and glycine at high concentrations have also been known to regenerate sensor surfaces used for antigen-antibody interaction analysis [127]. However, as seen in Figure 6.9, introducing increasing concentration of KCl solutions at steps *d, e* and *f* did not remove any antigen from the sensor surface, as evidenced by almost no change in the resonance wavelength position. A slight blue-shift in the resonance after the introduction of 3M KCl solution could be a result of drift in the measurement. This was also confirmed in steps *g* and *h* when a reintroduction of target molecules caused no appreciable shift in the resonance position. Introduction of 3M KCl solution at step *i* again did not shift the resonance back to the baseline. Points *a, b* and *c* denote the introduction of EDC/NHS, ligand and target molecule respectively.

Detergent solutions were also tested for regeneration of the sensor. Figure 6.10 shows the SEM image of the array of U-shaped nanostructures on ITO substrate before and after adding SDS on its surface. As seen in the figure, the detergent causes the gold nanostructures to lift off from their position, causing a complete disintegration of the sensor itself. Therefore, both the ionic and detergent based solutions proved to be ineffective solutions for regenerating the sensor surface.

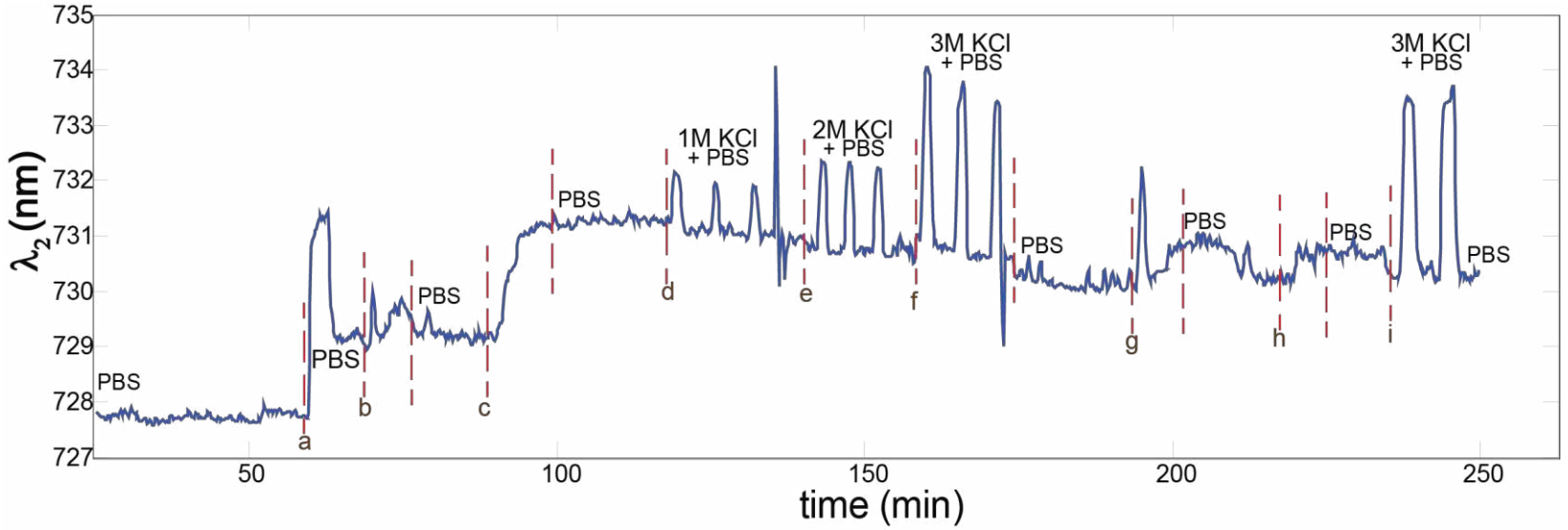

Figure 6.9 Plot showing shifts in λ_3 with respect to time as solutions with increasing concentration of KCl are introduced to the sensor surface.

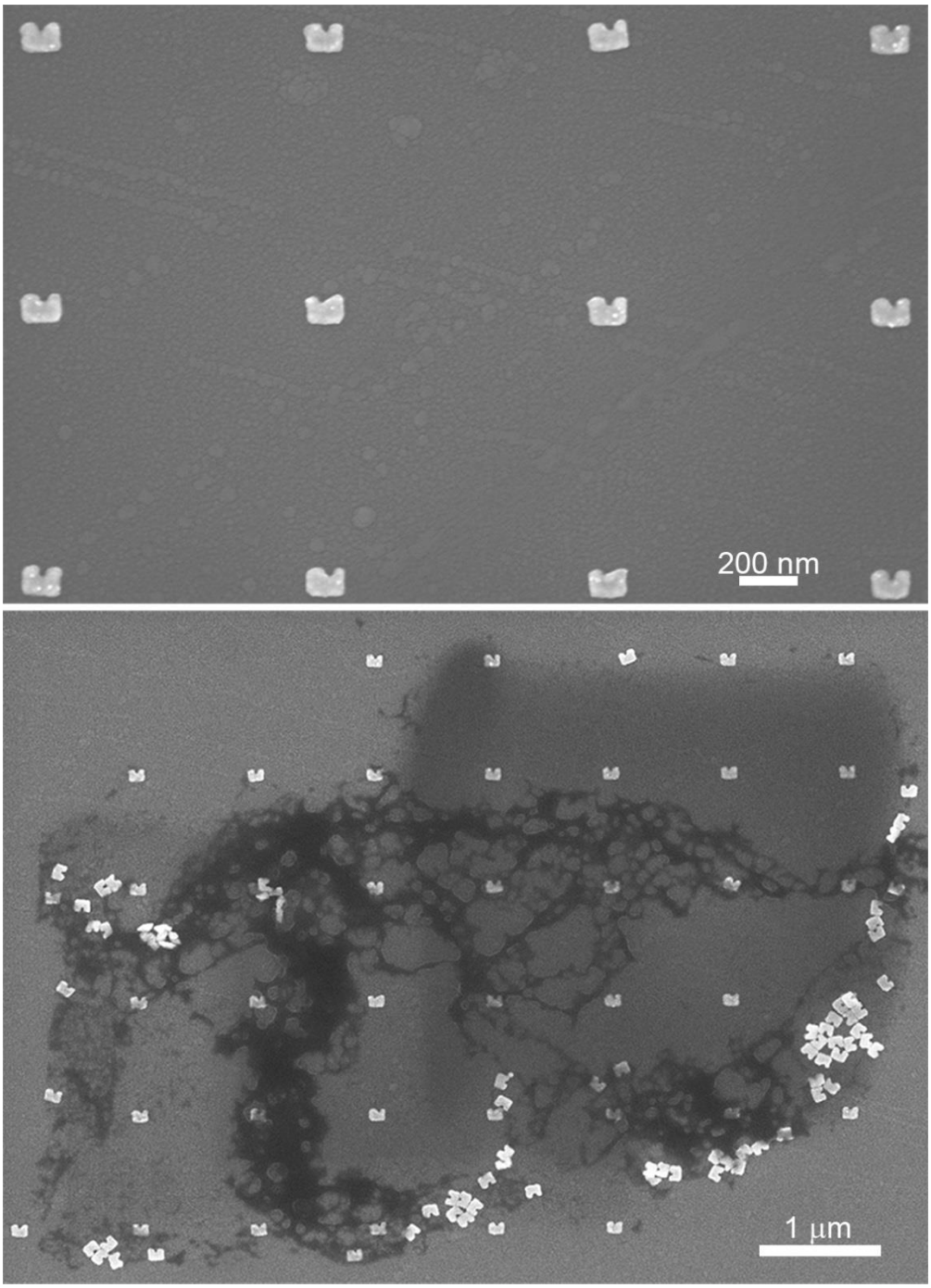

Figure 6.10 SEM images showing the before (top) and after (bottom) effects of adding SDS solution on the sensor surface.

6.3.4.3 Basic solution

After unsuccessfully testing acidic as well as ionic solutions, basic solutions were examined as a regeneration assay for the U-shaped nanostructure based biosensor. Figure 6.11 plots λ_2 versus time as NaOH solutions with varying concentrations (and pH values) are introduced on the sensor surface. Once again, steps *a, b* and *c* denote the introduction of EDC/NHS, ligand and the target molecule respectively. Introduction of 5mM NaOH solution at point labeled *d* causes a slight blue-shift in the wavelength position but does not completely bring it back to the baseline. This indicates that the regeneration solution did not completely clean the sensor surface form target antigens. However, further addition of target antigens and antibodies, as seen in steps *e* and *f* by the introduction of hIgG and anti-hIgG respectively, do not induce any further response from the sensor. Similar behavior was observed when the hIgG was used as the ligand molecule instead of the antibodies in a separate experiment. Further research into the stability of IgG molecules revealed its inability to handle harsh conditions, i.e., extremely high or low pH solutions. IgG molecules, especially around its Fc portion are very sensitive to changes in the pH of the solution [184]. This leads to a faster denaturation of IgG antibodies and antigens under harsh conditions making the sensor inoperable for further use. These experiments led to the conclusion that addition of a high pH solution onto the sensor surface was not only removing the target molecules but also denaturing the ligand attached onto the sensor surface.

Out of all the solutions tested, NaOH based regeneration solutions were able to remove analyte molecules from the sensor surface, albeit with loss in ligand activity. To circumvent this problem, and still use NaOH for regeneration, anti-hIgG antibodies were

replaced by Protein A as ligand molecules. Protein A molecules are extensively used in affinity chromatography for the detection of IgG molecules. The molecule consists of four or five high affinity binding sites that bind to only the Fc portion of the IgG resulting in an oriented immobilization of hIgG molecules and leaving the two antigen binding sites available for further interactions [185]. Protein A is also known to be stable over a wide range of pH values and it has been reported to show almost no loss in activity when cleaned with high pH NaOH solutions [186].

Protein A molecules can covalently bind to the MUA coated gold surface through the previously described EDC/NHS mechanism [187]. Therefore, NaOH was tested once again as a regeneration solution for Protein A-IgG binding interaction on U-shaped nanostructure based sensor. Figure 6.12 plots the shifts in the resonance wavelength with time for such an interaction. Here following the EDC/NHS reaction in step *a*, protein A is introduced at step *b* causing a slight red-shift in the resonance position. Introduction of hIgG molecules at step *c* leads to further red shift as the target molecule binds to the protein A coated sensor surface. Introduction of NaOH solutions of increasing concentrations in step *d, e* and *f* lead to very small reduction in the wavelength indicating that most of the target molecules are still bound to the sensor surface. This could be indicative of the strong bond of the Protein A molecule with the Fc portion of hIgG [186].

Before adding higher concentrations of NaOH solution, hIgG as well as anti-hIgG molecules were reintroduced at steps *g* and *h* through the flow cell. hIgG was introduced to ensure complete saturation of the sensor surface and anti-hIgG was added to interact with the hIgG coated sensor surface. Introduction of 10mM NaOH solution at point *j*

blue-shifts the wavelength indicating the removal of anti-hIgG molecules from the hIgG surface. To remove the hIgG target molecules from protein A surface, a 50mM NaOH solution was introduced. As seen at *k*, it removes some of the target antigens from the surface but not enough to return to its initial baseline of point *c*. However, further introduction of hIgG molecules at points *l* elicit similar response as when it was introduced at point *g*. Similarly, introduction of 50mM NaOH solution at *m* removes some of the antigen molecules bringing the wavelength position back to what it was before *l* or *g*. The previous two steps were replicated once again to ensure the repeatability of the sensor response. These experiments confirmed the compatibility of high pH NaOH solution as regeneration assay for Protein A-hIgG based gold nanosensor.

To summarize, a 10mM NaOH solution removes bound hIgG target molecules from an anti-hIgG coated sensor surface but with a complete loss in ligand activity making the sensor unusable for further experiments. However, this problem can be worked around by using Protein A as the recognition element instead of anti-hIgG along with using 50mM NaOH as regeneration solution.

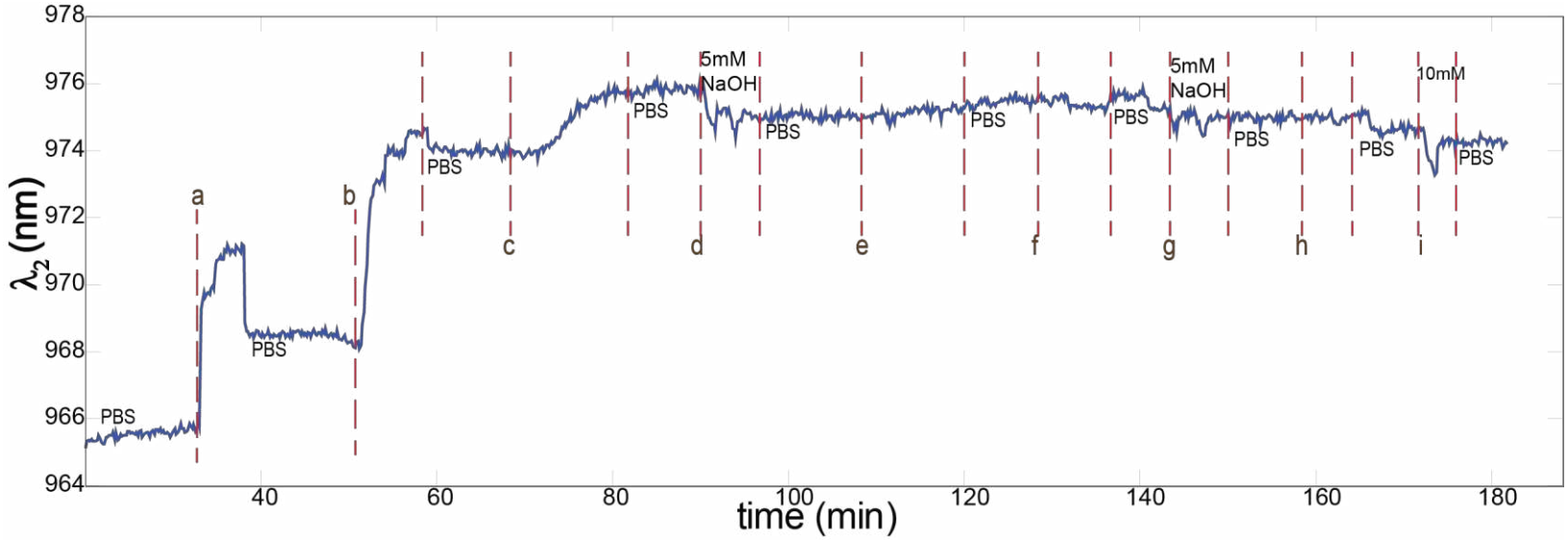

Figure 6.11 Evaluation of high pH regeneration solutions on the U-shaped nanostructure based biosensor. Different concentrations of NaOH solution are introduced on the sensor surface and the shifts in resonance wavelength recorded in time.

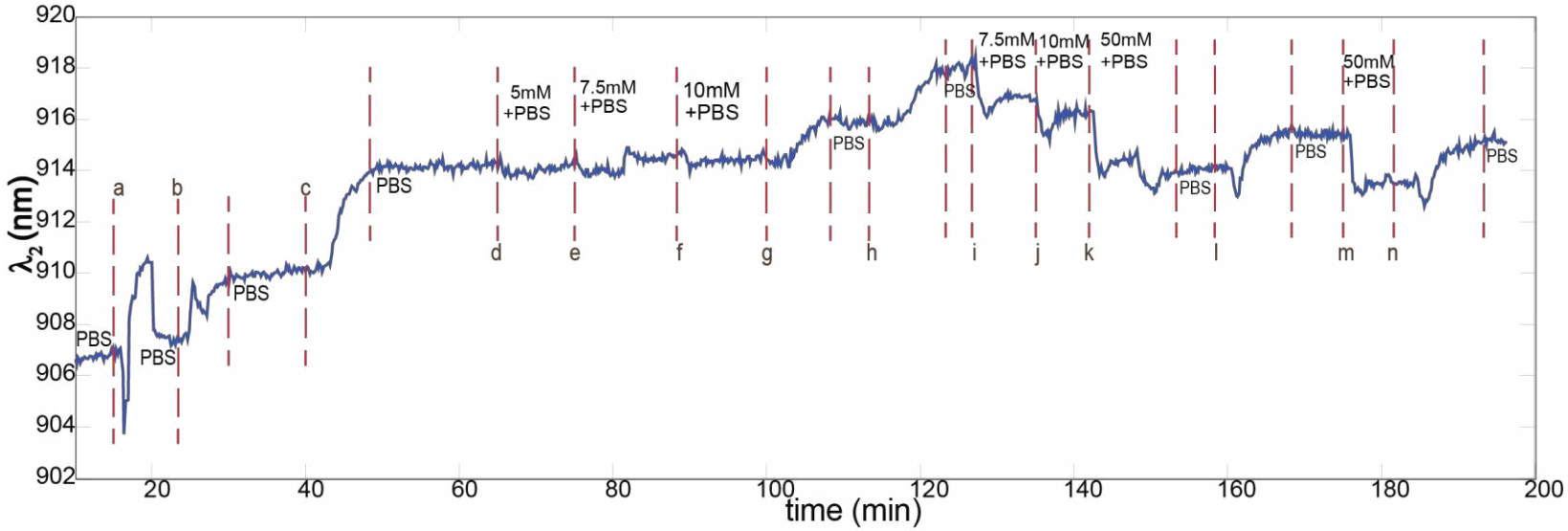

Figure 6.12 Plot of λ_2 versus time showing the effectiveness of using Protein A as the ligand molecule for the regeneration and repeatability of the sensor surface.

Table 6.1 Summary of regeneration conditions tested for U-shaped nanostructure based sensor for the analysis of IgG molecules.

Condition	Solution	Effect
Acidic	10mM glycine-HCl in PBS pH range from 2 -5	Acidic solutions attack the underlying ITO layer causing the resonances to jump around
Ionic	1-3mM KCl in DI water, 100mM glycine in PBS	No appreciable shift observed
Detergent	1% (w/v) SDS in PBS	Complete disintegration of the gold nanostructures
Basic	5-50mM NaOH (pH range from 11 to 12.5) in PBS	Regenerates the sensor surface

6.4 Conclusions

This chapter provided an overview of the various experiments performed for the optimization of the U-shaped nanostructure based sensor for the detection of hIgG target antigens. It was established that acidic solutions that are widely used for regeneration of antigen-antibody interactions are not compatible for sensors built on ITO surfaces. The use of basic solution for regeneration was successfully able to remove a portion of target antigens from the sensor surface, but it also affected the binding ability of immobilized ligand molecules, making the sensor inoperative for further experiments. However, replacing hIgG antibodies with Protein A as ligand molecules in conjugation with using high pH NaOH solution for regeneration, provides the most optimal condition for the repeated functioning of the sensor. It should be noted that these conditions are only optimized for this particular sensor and antigen-antibody interaction. Any change in the sensor or the biosensing interaction may warrant a complete change in the regeneration parameters.

Chapter 7

Conclusions and Future Directions

7.1 Conclusions

Biosensing using LSPR nanostructures has received a great deal of attention over the last decade. The ability of nanoscale metallic particles to detect refractive index changes through shifts in its plasmon resonances has allowed for label free detection of biological and chemical interactions. Compared to the traditional propagating sensors, LSPR sensors exhibit improved surface limits of detection in extremely low volume solutions. Other advantages include extensive wavelength tunability based on size, shape, material and dielectric environment as well as simpler optical setup for plasmon excitation.

Despite the substantial body of work on label free sensing with metallic nanostructures, a fundamental problem facing any sensor, i.e., compensation for interfering effects, has been mostly neglected. Until this is accomplished, LSPR sensors will be severely limited in their applicability, especially in point-of-care applications. These interfering interactions include changes in refractive index of the solution as well as non-specific adsorption of non-target molecules on the sensor surface. As these LSPR nanostructures respond similarly to both specific as well as non-specific effects, other means of differentiation between these effects is essential for the use of LSPR sensors, especially outside the laboratory environment.

The work presented here exploited the multiple surface plasmon modes of complex shaped nanostructures to optically compensate for interfering bulk and surface effects.

This technique utilized the inherent differences in the properties of surface plasmon modes of a particular nanostructure, including localized electric field profile at different regions on the particle surface. Separating solution refractive index changes from surface binding of target analyte was demonstrated both numerically and experimentally by exploiting the longitudinal and transverse modes of arrays of gold nanorods on an ITO coated glass substrate. The two modes with different penetration depths and separately localized field profiles were able to compensate for changes in the background refractive index and allow surface binding of the target analyte to be measured separately.

Similarly, to differentiate specific target interaction from both non-specific bulk and surface effects, arrays of U-shaped gold nanostructures exhibiting three resonances in the visible to near-IR region were fabricated on ITO coated glass substrate. The nanostructures were tested for their self-referencing capability by simultaneously measuring the shifts in the three resonances as different solutions, simulating a target interaction along with bulk and surface interference, were introduced. The three modes compensated for changes due to interfering bulk and surface effects, allowing the target molecule to be detected separately. These multi-mode sensors were also found to provide comparable sensitivities to various other LSPR based refractive-index sensors along with the added benefit of complete separation of interfering effects.

Finally, a series of experiments were conducted to characterize the various surface plasmon modes of the U-shaped gold nanostructure for the purpose of measuring unknown target concentrations in biological solutions. In particular, scouting for an optimal regeneration assay for the nanoscale biosensor was described in detail. It was discovered that the widely used low pH glycine-HCl solution was not suitable for

regenerating sensors built on ITO layers. Moreover, the use of a harsh solution, including acidic, basic or ionic, also resulted in a sharp reduction in ligand activity, thereby restricting the sensor for further use. It was finally shown experimentally that a high pH NaOH solution in combination with Protein A as the immobilized molecule provided an optimal regeneration assay for the repeated detection of IgG molecules.

7.2 Future Work

This work showed, both experimentally and numerically, the use of multiple plasmon modes of a complex nanostructure for compensating interfering effects. Even though the sensitivities of these structures were found comparable to other LSPR sensors, certain changes can still be introduced to improve its biosensing properties.

Both nanorods and U-shaped nanostructures used for biomolecular sensing were fabricated using electron beam lithography followed by thin film deposition. Nanoparticles formed through thin film deposition techniques like evaporation or sputtering are polycrystalline in nature. The presence of a rough and polycrystalline gold surface negatively impacts the formation of a perfect SAM layer [180]. A uniform and dense self-assembled monolayer (SAM) is an important part of an effective biosensor as it helps reduce the effect of non-specific binding as well as allows the formation of a uniform ligand layer [143]. Besides forming a defective SAM monolayer, it also causes a stronger damping of the various plasmon modes resulting in broader linewidths. Future sensing experiments can reduce the effect of polycrystalline surfaces by adding a simple annealing step in between. It has been experimentally shown that annealing gold surfaces, either through flame or furnace annealing method, increases the average grain size, reduces surface roughness as well as improves the crystallinity of the structure [188].

The nanostructures utilized for the analysis of dual- and multi-mode sensors were lithographically fabricated on the ITO substrate. Another method that can also be considered for developing multi-mode biosensors involve the use of chemically synthesized nanoparticles immobilized on a substrate. Compared to fabricated structures, chemically synthesized nanoparticles exhibit reduced plasmon resonance linewidths and hence, improved figures of merit. These structures are also single crystalline, providing perfect surfaces for improved SAM formation. Advancement in the area of colloidal synthesis have allowed for the creation of complex structures including triangular prisms, cubes and stars of uniform shapes and sizes [129]. Multi-mode biosensors can be formed using single or coupled nanostructures chemically immobilized to the substrate. Future work can focus on designing and implementing techniques to uniformly attach these gold or silver nanostructures to ITO or glass substrate for use as biosensors. For example, one can use electron beam lithography in combination with a SAM linker layer, like APTES, to selectively deposit nanostructures on ITO substrate. Further improvements in areas like flow cell design (e.g., using PDMS based cell instead of acrylic will provide improved chemical stability) and optical setup (e.g., using a higher mag objective that will restrict the spectral measurement to a smaller area, thereby reducing the resonance linewidth and improving the sensor's FOM) will also help develop improved multi-mode LSPR biosensors.

References

1. Faraday, M., *The Bakerian Lecture: Experimental Relations of Gold (and Other Metals) to Light.* Philosophical Transactions of the Royal Society of London, 1857. **147**: p. 145-181.
2. Mie, G., *Beiträge zur Optik trüber Medien, speziell kolloidaler Metallösungen.* Annalen der Physik, 1908. **330**(3): p. 377-445.
3. Garcia, M.A., *Surface plasmons in metallic nanoparticles: fundamentals and applications.* Journal of Physics D: Applied Physics, 2011. **44**(28): p. 283001.
4. Palik, E.D., *Handbook of Optical Constants of Solids*, Elsevier.
5. Maier, S., *Plasmonics - Fundamentals and Applications*. 2007: Springer-Verlag New York, LLC. 252.
6. Fox, M., *Optical Properties of Solids*. 2010: Oxford University Press.
7. Welford, K., *Surface plasmon-polaritons and their uses.* Optical and Quantum Electronics, 1991. **23**(1): p. 1-27.
8. Sambles, J.R., G.W. Bradbery, and F. Yang, *Optical excitation of surface plasmons: An introduction.* Contemporary Physics, 1991. **32**(3): p. 173-183.
9. Homola, J., *Surface Plasmon Resonance based Sensors*. 2006, Berlin, Germany.
10. Maier, S.A. and H.A. Atwater, *Plasmonics: Localization and Guiding of Electromagnetic Energy in Metal/Dielectric Structures.* Journal of Applied Physics, 2005. **98**(1): p. 011101-10.
11. Novotny, L. and B. Hecht, *Principle of Nano-optics*. 2006.
12. Bohren, C. and D. Huffman, *Absorption and Scattering of Light by Small Particles*. 1998: John Wiley and Sons. 544.
13. Zhao, J., et al., *Localized surface plasmon resonance biosensors.* Nanomedicine, 2006. **1**(2): p. 219-228.
14. Raschke, G., et al., *Biomolecular Recognition Based on Single Gold Nanoparticle Light Scattering.* Nano Letters, 2003. **3**(7): p. 935-938.
15. Kreibig, U. and M. Vollmer, *Optical Properties of Metal Clusters*. 1995: Springer-Verlag New York, LLC. 560.
16. Mock, J.J., et al., *Shape effects in plasmon resonance of individual colloidal silver nanoparticles.* The Journal of Chemical Physics, 2002. **116**(15): p. 6755-6759.
17. Sherry, L.J., et al., *Localized Surface Plasmon Resonance Spectroscopy of Single Silver Triangular Nanoprisms.* Nano Letters, 2006. **6**(9): p. 2060-2065.
18. Nehl, C.L., H. Liao, and J.H. Hafner, *Optical Properties of Star-Shaped Gold Nanoparticles.* Nano Letters, 2006. **6**(4): p. 683-688.
19. Hao, F., et al., *Plasmon Resonances of a Gold Nanostar.* Nano Letters, 2007. **7**(3): p. 729-732.
20. Sherry, L.J., et al., *Localized Surface Plasmon Resonance Spectroscopy of Single Silver Nanocubes.* Nano Letters, 2005. **5**(10): p. 2034-2038.
21. Knight, M.W. and N.J. Halas, *Nanoshells to nanoeggs to nanocups: optical properties of reduced symmetry core–shell nanoparticles beyond the quasistatic limit.* New Journal of Physics, 2008. **10**(10): p. 105006.
22. Knight, M.W., et al., *Substrates Matter: Influence of an Adjacent Dielectric on an Individual Plasmonic Nanoparticle.* Nano Letters, 2009. **9**(5): p. 2188-2192.

23. Huda, G.M., et al., *Effects of a silicon probe on gold nanoparticles on glass under evanescent illumination.* Opt. Express, 2011. **19**(13): p. 12679-12687.
24. Oubre, C. and P. Nordlander, *Optical Properties of Metallodielectric Nanostructures Calculated Using the Finite Difference Time Domain Method.* The Journal of Physical Chemistry B, 2004. **108**(46): p. 17740-17747.
25. Sosa, I.O., C. Noguez, and R.G. Barrera, *Optical Properties of Metal Nanoparticles with Arbitrary Shapes.* The Journal of Physical Chemistry B, 2003. **107**(26): p. 6269-6275.
26. Zhao, J., et al., *Methods for Describing the Electromagnetic Properties of Silver and Gold Nanoparticles.* Accounts of Chemical Research, 2008. **41**(12): p. 1710-1720.
27. Parsons, J., et al., *A comparison of techniques used to simulate the scattering of electromagnetic radiation by metallic nanostructures.* Journal of Modern Optics, 2010. **57**(5): p. 356-365.
28. Polycarpou, A.C., *Introduction to the Finite Element Method in Electromagnetics*. Synthesis Lectures on Computational Electromagnetics. Vol. 1. 2006: Morgan & Claypool Publishers. 1-126.
29. Kelly, K.L., et al., *The Optical Properties of Metal Nanoparticles: The Influence of Size, Shape, and Dielectric Environment.* The Journal of Physical Chemistry B, 2002. **107**(3): p. 668-677.
30. Meier, M. and A. Wokaun, *Enhanced fields on large metal particles: dynamic depolarization.* Opt. Lett., 1983. **8**(11): p. 581-583.
31. Link, S. and M.A. El-Sayed, *Shape and size dependence of radiative, non-radiative and photothermal properties of gold nanocrystals.* International Reviews in Physical Chemistry, 2000. **19**(3): p. 409-453.
32. Chen, H., et al., *Shape- and Size-Dependent Refractive Index Sensitivity of Gold Nanoparticles.* Langmuir, 2008. **24**(10): p. 5233-5237.
33. Johnson, P.B. and R.W. Christy, *Optical Constants of the Noble Metals.* Physical Review B, 1972. **6**(12): p. 4370.
34. Chan, G.H., et al., *Plasmonic Properties of Copper Nanoparticles Fabricated by Nanosphere Lithography.* Nano Letters, 2007. **7**(7): p. 1947-1952.
35. McMahon, J.M., G.C. Schatz, and S.K. Gray, *Plasmonics in the ultraviolet with the poor metals Al, Ga, In, Sn, Tl, Pb, and Bi.* Physical Chemistry Chemical Physics, 2013. **15**(15): p. 5415-5423.
36. Jr., D.D.E. and G. Chumanov, *Synthesis and Optical Properties of Silver Nanoparticles and Arrays.* ChemPhysChem, 2005. **6**(7): p. 1221-1231.
37. Petryayeva, E. and U.J. Krull, *Localized surface plasmon resonance: Nanostructures, bioassays and biosensing—A review.* Analytica Chimica Acta, 2011. **706**(1): p. 8-24.
38. Stewart, M.E., et al., *Nanostructured Plasmonic Sensors.* Chemical Reviews, 2008. **108**(2): p. 494-521.
39. Luo, Y.-L., Y.-S. Shiao, and Y.-F. Huang, *Release of Photoactivatable Drugs from Plasmonic Nanoparticles for Targeted Cancer Therapy.* ACS Nano, 2011. **5**(10): p. 7796-7804.
40. Dickerson, E.B., et al., *Gold nanorod assisted near-infrared plasmonic photothermal therapy (PPTT) of squamous cell carcinoma in mice.* Cancer Letters, 2008. **269**(1): p. 57-66.
41. El-Sayed, I.H., X. Huang, and M.A. El-Sayed, *Surface Plasmon Resonance Scattering and Absorption of anti-EGFR Antibody Conjugated Gold Nanoparticles in Cancer Diagnostics: Applications in Oral Cancer.* Nano Letters, 2005. **5**(5): p. 829-834.
42. Zhou, W., et al., *A label-free biosensor based on silver nanoparticles array for clinical detection of serum p53 in head and neck squamous cell carcinoma.* Int J Nanomedicine, 2011. **6**: p. 381-6.

43. Ozbay, E., *Plasmonics: Merging Photonics and Electronics at Nanoscale Dimensions.* Science, 2006. **311**(5758): p. 189-193.
44. Pillai, S., et al., *Surface plasmon enhanced silicon solar cells.* Journal of Applied Physics, 2007. **101**(9): p. 093105.
45. Cole, J.R. and N.J. Halas, *Optimized plasmonic nanoparticle distributions for solar spectrum harvesting.* Applied Physics Letters, 2006. **89**(15): p. 153120.
46. Miao, X. and L.Y. Lin. *Enhanced Optical Trapping through Localized Surface Plasmon Resonance of Au Nanoparticle Array*. in *Conference on Lasers and Electro-Optics/Quantum Electronics and Laser Science Conference and Photonic Applications Systems Technologies*. 2007. Baltimore, Maryland: Optical Society of America.
47. Englebienne, P., *Use of colloidal gold surface plasmon resonance peak shift to infer affinity constants from the interactions between protein antigens and antibodies specific for single or multiple epitopes.* Analyst, 1998. **123**(7): p. 1599-1603.
48. Kumar, A., B.M. Boruah, and X.J. Liang, *Gold Nanoparticles: Promising Nanomaterials for the Diagnosis of Cancer and HIV/AIDS.* Journal of Nanomaterials, 2011. **2011**(202187): p. 17.
49. Wang, C. and J. Irudayaraj, *Gold Nanorod Probes for the Detection of Multiple Pathogens.* Small, 2008. **4**(12): p. 2204-2208.
50. Miller, M.M. and A.A. Lazarides, *Sensitivity of Metal Nanoparticle Surface Plasmon Resonance to the Dielectric Environment.* The Journal of Physical Chemistry B, 2005. **109**(46): p. 21556-21565.
51. Svedendahl, M., et al., *Refractometric Sensing Using Propagating versus Localized Surface Plasmons: A Direct Comparison.* Nano Letters, 2009. **9**(12): p. 4428-4433.
52. Kvasnička, P. and J. Homola, *Optical sensors based on spectroscopy of localized surface plasmons on metallic nanoparticles: Sensitivity considerations.* Biointerphases, 2008. **3**(3): p. FD4-FD11.
53. Otte, M. and B. Sepulveda, *Figures of Merit for Refractometric LSPR Biosensing*, in *Nanoplasmonic Sensors*, A. Dmitriev, Editor. 2012, Springer New York. p. 317-331.
54. Verellen, N., et al., *Plasmon Line Shaping Using Nanocrosses for High Sensitivity Localized Surface Plasmon Resonance Sensing.* Nano Letters, 2011. **11**(2): p. 391-397.
55. Sonnefraud, Y., et al., *Experimental Realization of Subradiant, Superradiant, and Fano Resonances in Ring/Disk Plasmonic Nanocavities.* ACS Nano, 2010. **4**(3): p. 1664-1670.
56. Kubo, W. and S. Fujikawa, *Au Double Nanopillars with Nanogap for Plasmonic Sensor.* Nano Letters, 2010. **11**(1): p. 8-15.
57. Offermans, P., et al., *Universal Scaling of the Figure of Merit of Plasmonic Sensors.* ACS Nano, 2011. **5**(6): p. 5151-5157.
58. Riboh, J.C., et al., *A Nanoscale Optical Biosensor: Real-Time Immunoassay in Physiological Buffer Enabled by Improved Nanoparticle Adhesion.* The Journal of Physical Chemistry B, 2003. **107**(8): p. 1772-1780.
59. Malinsky, M.D., et al., *Chain Length Dependence and Sensing Capabilities of the Localized Surface Plasmon Resonance of Silver Nanoparticles Chemically Modified with Alkanethiol Self-Assembled Monolayers.* Journal of the American Chemical Society, 2001. **123**(7): p. 1471-1482.
60. Haes, A.J., et al., *A Nanoscale Optical Biosensor: The Long Range Distance Dependence of the Localized Surface Plasmon Resonance of Noble Metal Nanoparticles.* The Journal of Physical Chemistry B, 2003. **108**(1): p. 109-116.
61. Feuz, L., M.P. Jonsson, and F. Höök, *Material-Selective Surface Chemistry for Nanoplasmonic Sensors: Optimizing Sensitivity and Controlling Binding to Local Hot Spots.* Nano Letters, 2012. **12**(2): p. 873-879.

62. Larsson, E.M., et al., *Sensing Characteristics of NIR Localized Surface Plasmon Resonances in Gold Nanorings for Application as Ultrasensitive Biosensors.* Nano Letters, 2007. **7**(5): p. 1256-1263.
63. Wang, H., et al., *Nanorice: A Hybrid Plasmonic Nanostructure.* Nano Letters, 2006. **6**(4): p. 827-832.
64. Tam, F., C. Moran, and N. Halas, *Geometrical Parameters Controlling Sensitivity of Nanoshell Plasmon Resonances to Changes in Dielectric Environment.* The Journal of Physical Chemistry B, 2004. **108**(45): p. 17290-17294.
65. Mayer, K.M., et al., *A Label-Free Immunoassay Based Upon Localized Surface Plasmon Resonance of Gold Nanorods.* ACS Nano, 2008. **2**(4): p. 687-692.
66. Ma, W.Y., et al., *A numerical investigation of the effect of vertex geometry on localized surface plasmon resonance of nanostructures.* Opt. Express, 2010. **18**(2): p. 843-853.
67. Vo-Dinh, T. and B. Cullum, *Biosensors and biochips: advances in biological and medical diagnostics.* Fresenius' Journal of Analytical Chemistry, 2000. **366**(6-7): p. 540-551.
68. Fritz, J., et al., *Translating Biomolecular Recognition into Nanomechanics.* Science, 2000. **288**(5464): p. 316-318.
69. Arlett, J.L., E.B. Myers, and M.L. Roukes, *Comparative advantages of mechanical biosensors.* Nat Nano, 2011. **6**(4): p. 203-215.
70. Tamayo, J., et al., *Biosensors based on nanomechanical systems.* Chemical Society Reviews, 2013. **42**(3): p. 1287-1311.
71. Carrascosa, L.G., et al., *Nanomechanical biosensors: a new sensing tool.* TrAC Trends in Analytical Chemistry, 2006. **25**(3): p. 196-206.
72. Thévenot, D.R., et al., *Electrochemical biosensors: recommended definitions and classification.* Biosensors and Bioelectronics, 2001. **16**(1–2): p. 121-131.
73. Wang, J., *Glucose Biosensors: 40 Years of Advances and Challenges.* Sensors Update, 2002. **10**(1): p. 107-119.
74. Cui, Y., et al., *Nanowire Nanosensors for Highly Sensitive and Selective Detection of Biological and Chemical Species.* Science, 2001. **293**(5533): p. 1289-1292.
75. Grieshaber, D., et al., *Electrochemical Biosensors - Sensor Principles and Architectures.* Sensors, 2008. **8**(3): p. 1400-1458.
76. Luo, X. and J.J. Davis, *Electrical biosensors and the label free detection of protein disease biomarkers.* Chemical Society Reviews, 2013. **42**(13): p. 5944-5962.
77. Zheng, G., et al., *Multiplexed electrical detection of cancer markers with nanowire sensor arrays.* Nat Biotech, 2005. **23**(10): p. 1294-1301.
78. Calleja, M., et al., *Challenges for nanomechanical sensors in biological detection.* Nanoscale, 2012. **4**(16): p. 4925-4938.
79. Borisov, S.M. and O.S. Wolfbeis, *Optical Biosensors.* Chemical Reviews, 2008. **108**(2): p. 423-461.
80. Paulie, S., H. Perlmann, and P. Perlmann, *Enzyme-linked Immunosorbent Assay*, in *eLS*. 2001, John Wiley & Sons, Ltd.
81. Lequin, R.M., *Enzyme Immunoassay (EIA)/Enzyme-Linked Immunosorbent Assay (ELISA).* Clinical Chemistry, 2005. **51**(12): p. 2415-2418.
82. Heller, M.J., *DNA MICROARRAY TECHNOLOGY: Devices, Systems, and Applications.* Annual Review of Biomedical Engineering, 2002. **4**(1): p. 129-153.
83. Troia, B., et al., *Photonic Crystals for Optical Sensing: A Review.* 2013.
84. Zourob, M. and A. Lakhtakia, *Optical Guided-wave Chemical and Biosensors: II*. Vol. 2. 2010: Springer.
85. Sun, Y. and X. Fan, *Optical ring resonators for biochemical and chemical sensing.* Analytical and bioanalytical chemistry, 2011. **399**(1): p. 205-211.

86. Homola, J., S.S. Yee, and G. Gauglitz, *Surface plasmon resonance sensors: review.* Sensors and Actuators B: Chemical, 1999. **54**(1–2): p. 3-15.
87. Haes, A.J. and R.P. Van Duyne, *A unified view of propagating and localized surface plasmon resonance biosensors.* Analytical and Bioanalytical Chemistry, 2004. **379**(7): p. 920-930.
88. Nylander, C., B. Liedberg, and T. Lind, *Gas detection by means of surface plasmon resonance.* Sensors and Actuators, 1982. **3**: p. 79-88.
89. Forozan, F., et al., *Comparative genomic hybridization analysis of 38 breast cancer cell lines: a basis for interpreting complementary DNA microarray data.* Cancer Res, 2000. **60**(16): p. 4519-25.
90. Otte, M.A., et al., *Identification of the Optimal Spectral Region for Plasmonic and Nanoplasmonic Sensing.* ACS Nano, 2009. **4**(1): p. 349-357.
91. Fu, J., B. Park, and Y. Zhao, *Limitation of a localized surface plasmon resonance sensor for Salmonella detection.* Sensors and Actuators B: Chemical, 2009. **141**(1): p. 276-283.
92. Minh Hiep, H., et al., *A localized surface plasmon resonance based immunosensor for the detection of casein in milk.* Science and Technology of Advanced Materials, 2007. **8**(4): p. 331-338.
93. Rodríguez-Cantó, P., et al., *Demonstration of near infrared gas sensing using gold nanodisks on functionalized silicon.* Opt. Express, 2011. **19**(8): p. 7664-7672.
94. Dahlin, A.B., J.O. Tegenfeldt, and F. Höök, *Improving the instrumental resolution of sensors based on localized surface plasmon resonance.* Analytical chemistry, 2006. **78**(13): p. 4416-4423.
95. Feuz, L., et al., *Improving the Limit of Detection of Nanoscale Sensors by Directed Binding to High-Sensitivity Areas.* ACS Nano, 2010. **4**(4): p. 2167-2177.
96. Rosi, N.L. and C.A. Mirkin, *Nanostructures in biodiagnostics.* Chem Rev, 2005. **105**(4): p. 1547-62.
97. Elghanian, R., et al., *Selective Colorimetric Detection of Polynucleotides Based on the Distance-Dependent Optical Properties of Gold Nanoparticles.* Science, 1997. **277**(5329): p. 1078-1081.
98. Storhoff, J.J., et al., *One-Pot Colorimetric Differentiation of Polynucleotides with Single Base Imperfections Using Gold Nanoparticle Probes.* Journal of the American Chemical Society, 1998. **120**(9): p. 1959-1964.
99. Sato, K., K. Hosokawa, and M. Maeda, *Rapid Aggregation of Gold Nanoparticles Induced by Non-Cross-Linking DNA Hybridization.* Journal of the American Chemical Society, 2003. **125**(27): p. 8102-8103.
100. Kang, J.-H., et al., *Gold nanoparticle-based colorimetric assay for cancer diagnosis.* Biosensors and Bioelectronics, 2010. **25**(8): p. 1869-1874.
101. Chen, C.-K., C.-C. Huang, and H.-T. Chang, *Label-free colorimetric detection of picomolar thrombin in blood plasma using a gold nanoparticle-based assay.* Biosensors and Bioelectronics, 2010. **25**(8): p. 1922-1927.
102. Wei, H., et al., *Simple and sensitive aptamer-based colorimetric sensing of protein using unmodified gold nanoparticle probes.* Chemical Communications, 2007(36): p. 3735-3737.
103. Hirsch, L.R., et al., *A Whole Blood Immunoassay Using Gold Nanoshells.* Analytical Chemistry, 2003. **75**(10): p. 2377-2381.
104. Zhao, W., M.A. Brook, and Y. Li, *Design of Gold Nanoparticle-Based Colorimetric Biosensing Assays.* ChemBioChem, 2008. **9**(15): p. 2363-2371.
105. Vilela, D., M.C. González, and A. Escarpa, *Sensing colorimetric approaches based on gold and silver nanoparticles aggregation: Chemical creativity behind the assay. A review.* Analytica Chimica Acta, 2012. **751**(0): p. 24-43.

106. Schofield, C.L., R.A. Field, and D.A. Russell, *Glyconanoparticles for the Colorimetric Detection of Cholera Toxin.* Analytical Chemistry, 2007. **79**(4): p. 1356-1361.
107. Nusz, G.J., et al., *Label-Free Plasmonic Detection of Biomolecular Binding by a Single Gold Nanorod.* Analytical Chemistry, 2008. **80**(4): p. 984-989.
108. Marinakos, S.M., S. Chen, and A. Chilkoti, *Plasmonic Detection of a Model Analyte in Serum by a Gold Nanorod Sensor.* Analytical Chemistry, 2007. **79**(14): p. 5278-5283.
109. Nath, N. and A. Chilkoti, *A Colorimetric Gold Nanoparticle Sensor To Interrogate Biomolecular Interactions in Real Time on a Surface.* Analytical Chemistry, 2001. **74**(3): p. 504-509.
110. Haes, A.J. and R.P. Van Duyne, *A Nanoscale Optical Biosensor: Sensitivity and Selectivity of an Approach Based on the Localized Surface Plasmon Resonance Spectroscopy of Triangular Silver Nanoparticles.* Journal of the American Chemical Society, 2002. **124**(35): p. 10596-10604.
111. Siegel, R., D. Naishadham, and A. Jemal, *Cancer statistics, 2013.* CA: A Cancer Journal for Clinicians, 2013. **63**(1): p. 11-30.
112. Jain, K., *Advances in the field of nanooncology.* BMC Medicine, 2010. **8**(1): p. 83.
113. Huang, X. and M.A. El-Sayed, *Plasmonic photo-thermal therapy (PPTT).* Alexandria Journal of Medicine, 2011. **47**(1): p. 1-9.
114. Dreaden, E.C., et al., *Size matters: gold nanoparticles in targeted cancer drug delivery.* Therapeutic Delivery, 2012. **3**(4): p. 457-478.
115. Truong, P.L., B.W. Kim, and S.J. Sim, *Rational Aspect Ratio and Suitable Antibody Coverage of Gold Nanorod for Ultra-Sensitive Detection of a Cancer Biomarker.* Lab on a Chip, 2012. **12**(6): p. 1102-1109.
116. Truong, P.L., et al., *A New Method for Non-Labeling Attomolar Detection of Diseases Based on an Individual Gold Nanorod Immunosensor.* Lab on a Chip, 2011. **11**(15): p. 2591-2597.
117. Cao, C. and S.J. Sim, *Resonant Rayleigh light scattering response of individual Au nanoparticles to antigen-antibody interaction.* Lab on a Chip, 2009. **9**(13): p. 1836-1839.
118. Yuan, J., et al., *Detection of serum human epididymis secretory protein 4 in patients with ovarian cancer using a label-free biosensor based on localized surface plasmon resonance.* Int J Nanomedicine, 2012. **7**: p. 2921-8.
119. Roche, P.J., et al., *A Camera Phone Localised Surface Plasmon Biosensing Platform towards Low-Cost Label-Free Diagnostic Testing.* Journal of Sensors, 2011. **2011**.
120. Munge, B.S., et al., *Electrochemical immunosensors for interleukin-6. Comparison of carbon nanotube forest and gold nanoparticle platforms.* Electrochemistry Communications, 2009. **11**(5): p. 1009-1012.
121. Lu, W., et al., *Multifunctional Oval-Shaped Gold-Nanoparticle-Based Selective Detection of Breast Cancer Cells Using Simple Colorimetric and Highly Sensitive Two-Photon Scattering Assay.* ACS Nano, 2010. **4**(3): p. 1739-1749.
122. Chon, H., et al., *Highly Sensitive Immunoassay of Lung Cancer Marker Carcinoembryonic Antigen Using Surface-Enhanced Raman Scattering of Hollow Gold Nanospheres.* Analytical Chemistry, 2009. **81**(8): p. 3029-3034.
123. Lee, S., et al., *Surface-enhanced Raman scattering imaging of HER2 cancer markers overexpressed in single MCF7 cells using antibody conjugated hollow gold nanospheres.* Biosensors and Bioelectronics, 2009. **24**(7): p. 2260-2263.
124. Haes, A.J., et al., *A Localized Surface Plasmon Resonance Biosensor: First Steps toward an Assay for Alzheimer's Disease.* Nano Letters, 2004. **4**(6): p. 1029-1034.
125. Vestergaard, M.d., et al., *Detection of Alzheimer's tau protein using localised surface plasmon resonance-based immunochip.* Talanta, 2008. **74**(4): p. 1038-1042.

126. Lai, T., et al., *Clinical application of a novel sliver nanoparticles biosensor based on localized surface plasmon resonance for detecting the microalbuminuria.* Acta Biochimica et Biophysica Sinica, 2010. **42**(11): p. 787-792.
127. Lee, J.-H., et al., *Highly sensitive localized surface plasmon resonance immunosensor for label-free detection of HIV-1.* Nanomedicine: Nanotechnology, Biology and Medicine, 2013. **9**(7): p. 1018-1026.
128. Wang, X., et al., *Gold nanorod-based localized surface plasmon resonance biosensor for sensitive detection of hepatitis B virus in buffer, blood serum and plasma.* Biosensors and Bioelectronics, 2010. **26**(2): p. 404-410.
129. Murphy, C.J., et al., *Anisotropic Metal Nanoparticles: Synthesis, Assembly, and Optical Applications.* The Journal of Physical Chemistry B, 2005. **109**(29): p. 13857-13870.
130. Pelton, M., J. Aizpurua, and G. Bryant, *Metal-nanoparticle plasmonics.* Laser & Photonics Review, 2008. **2**(3): p. 136-159.
131. Homola, J., *Present and future of surface plasmon resonance biosensors.* Analytical and Bioanalytical Chemistry, 2003. **377**(3): p. 528-539.
132. Homola, J., H.B. Lu, and S.S. Yee, *Dual-channel surface plasmon resonance sensor with spectral discrimination of sensing channels using dielectric overlayer.* Electronics Letters, 1999. **35**(13): p. 1105-1106.
133. Hastings, J.T., et al., *Optimal self-referenced sensing using long- andshort- range surface plasmons.* Opt. Express, 2007. **15**(26): p. 17661-17672.
134. Radan, S., H. Jiří, and V. Hana, *Advanced biosensing using simultaneous excitation of short and long range surface plasmons.* Measurement Science and Technology, 2006. **17**(4): p. 932-939.
135. Huang, X., S. Neretina, and M.A. El-Sayed, *Gold Nanorods: From Synthesis and Properties to Biological and Biomedical Applications.* Advanced Materials, 2009. **21**(48): p. 4880-4910.
136. Sharma, V., K. Park, and M. Srinivasarao, *Colloidal dispersion of gold nanorods: Historical background, optical properties, seed-mediated synthesis, shape separation and self-assembly.* Materials Science and Engineering: R: Reports, 2009. **65**(1–3): p. 1-38.
137. Hao, E. and G.C. Schatz, *Electromagnetic fields around silver nanoparticles and dimers.* The Journal of Chemical Physics, 2004. **120**(1): p. 357-366.
138. Stefan Kooij, E. and B. Poelsema, *Shape and size effects in the optical properties of metallic nanorods.* Physical Chemistry Chemical Physics, 2006. **8**(28): p. 3349-3357.
139. Chen, C.-D., et al., *Sensing capability of the localized surface plasmon resonance of gold nanorods.* Biosensors and Bioelectronics, 2007. **22**(6): p. 926-932.
140. Scientific, T., *EZ-Link HPDP-Biotin Instructions.*
141. Nehru, N., et al., *Differentiating Surface and Bulk Interactions using Localized Surface Plasmon Resonances of Gold Nanorods.* Opt. Express, 2012. **20**(7): p. 6905-6914.
142. Tate, J. and G. Ward, *Interferences in immunoassay.* The Clinical Biochemist Reviews, 2004. **25**(2): p. 105.
143. Choi, S. and J. Chae, *Methods of reducing non-specific adsorption in microfluidic biosensors.* Journal of Micromechanics and Microengineering, 2010. **20**(7): p. 075015.
144. Uludag, Y. and I.E. Tothill, *Cancer Biomarker Detection in Serum Samples Using Surface Plasmon Resonance and Quartz Crystal Microbalance Sensors with Nanoparticle Signal Amplification.* Analytical Chemistry, 2012. **84**(14): p. 5898-5904.
145. Lahav, M., A. Vaskevich, and I. Rubinstein, *Biological Sensing Using Transmission Surface Plasmon Resonance Spectroscopy.* Langmuir, 2004. **20**(18): p. 7365-7367.
146. Huang, T.T., et al., *Composite surface for blocking bacterial adsorption on protein biochips.* Biotechnology and Bioengineering, 2003. **81**(5): p. 618-624.
147. Enkrich, C., et al., *Magnetic Metamaterials at Telecommunication and Visible Frequencies.* Physical Review Letters, 2005. **95**(20): p. 203901.

148. Linden, S., et al., *Magnetic Response of Metamaterials at 100 Terahertz.* Science, 2004. **306**(5700): p. 1351-1353.
149. Lai, Y.-C., et al., *Label-Free, Coupler-Free, Scalable and Intracellular Bio-imaging by Multimode Plasmonic Resonances in Split-Ring Resonators.* Advanced Materials, 2012. **24**(23): p. OP148-OP152.
150. Pryce, I.M., et al., *Compliant Metamaterials for Resonantly Enhanced Infrared Absorption Spectroscopy and Refractive Index Sensing.* ACS Nano, 2011. **5**(10): p. 8167-8174.
151. Corrigan, T.D., et al., *Optical Plasmonic Resonances in Split-Ring Resonator Structures: an Improved LC Model.* Opt. Express, 2008. **16**(24): p. 19850-19864.
152. Rockstuhl, C., et al., *Resonances of Split-Ring Resonator Metamaterials in the Near Infrared.* Applied Physics B: Lasers and Optics, 2006. **84**(1): p. 219-227.
153. Rockstuhl, C., et al., *On the Reinterpretation of Resonances in Split-Ring-Resonators at Normal Incidence.* Opt. Express, 2006. **14**(19): p. 8827-8836.
154. Enkrich, C., et al., *Focused-Ion-Beam Nanofabrication of Near-Infrared Magnetic Metamaterials.* Advanced Materials, 2005. **17**(21): p. 2547-2549.
155. Klein, M.W., et al., *Single-slit split-ring resonators at optical frequencies: limits of size scaling.* Opt. Lett., 2006. **31**(9): p. 1259-1261.
156. Katsarakis, N., et al., *Electric coupling to the magnetic resonance of split ring resonators.* Applied Physics Letters, 2004. **84**(15): p. 2943-2945.
157. Zhang, Z. and Y. Zhao, *Optical properties of U-shaped Ag nanostructures.* Journal of Physics: Condensed Matter, 2008. **20**(34): p. 345223.
158. Chang, Y.-T., et al., *A multi-functional plasmonic biosensor.* Opt. Express, 2010. **18**(9): p. 9561-9569.
159. Liu, Z., et al., *Visible transmission response of nanoscale complementary metamaterials for sensing applications.* Nanotechnology, 2012. **23**(27): p. 275503.
160. Raman, A. and S. Fan, *Perturbation theory for plasmonic modulation and sensing.* Physical Review B, 2011. **83**(20): p. 205131.
161. Iyer, S., S. Popov, and A.T. Friberg, *Transmission resonances in periodic U-shaped metallic nanostructures.* Opt. Express, 2010. **18**(17): p. 17719-17728.
162. Haes, A.J. and R.P.V. Duyne, *Preliminary studies and potential applications of localized surface plasmon resonance spectroscopy in medical diagnostics.* Expert Review of Molecular Diagnostics, 2004. **4**(4): p. 527-537.
163. Nehru, N., et al., *Using U-Shaped Localized Surface Plasmon Resonance Sensors to Compensate for Nonspecific Interactions.* Nanotechnology, IEEE Transactions on, 2014. **13**(1): p. 55-61.
164. Lee, K.-S. and M.A. El-Sayed, *Gold and Silver Nanoparticles in Sensing and Imaging: Sensitivity of Plasmon Response to Size, Shape, and Metal Composition.* The Journal of Physical Chemistry B, 2006. **110**(39): p. 19220-19225.
165. Wriedt, T., *Light scattering theories and computer codes.* Journal of Quantitative Spectroscopy and Radiative Transfer, 2009. **110**(11): p. 833-843.
166. Barnes, W.L., *Comparing experiment and theory in plasmonics.* Journal of Optics A: Pure and Applied Optics, 2009. **11**(11): p. 114002.
167. Supplies, S. *http://www.2spi.com/catalog/standards/ITO-coated-substrates-refractive-index-values.html*.
168. Hecht, E., *Optics*. 2002.
169. Huda, G.M., *Effect of a Silicon Tip on Absorption Cross Section, Field Enhancement, and Localized Surface Plasmon Resonance of Different Sized Gold Nanoparticles Under Evanescent Wave Illumination*, 2011.
170. Horiba. *http://www.horiba.com/fileadmin/uploads/Scientific/Documents/TFilm/se-18.pdf*.

171. Tudos, A.J. and R.B.M. Schasfoort, *Introduction to Surface Plasmon Resonance*, in *Handbook of surface plasmon resonance*. 2008, Royal Society of Chemistry. p. 1-13.
172. Healthcare, G.E., *Biacore Sensor Surface Handbook*.
173. Andersson, K., M. Hämäläinen, and M. Malmqvist, *Identification and Optimization of Regeneration Conditions for Affinity-Based Biosensor Assays. A Multivariate Cocktail Approach.* Analytical Chemistry, 1999. **71**(13): p. 2475-2481.
174. Wilchek, M. and E.A. Bayer, *The avidin-biotin complex in bioanalytical applications.* Analytical Biochemistry, 1988. **171**(1): p. 1-32.
175. Holmberg, A., et al., *The biotin-streptavidin interaction can be reversibly broken using water at elevated temperatures.* Electrophoresis, 2005. **26**(3): p. 501-510.
176. Nezlin, R., *The immunoglobulins: structure and function*. 1998: Access Online via Elsevier.
177. Paul, S., et al., *Surface plasmon resonance imaging detection of silver nanoparticle-tagged immunoglobulin.* Journal of The Royal Society Interface, 2011. **8**(61): p. 1204-1211.
178. Lyon, L.A., et al., *Surface plasmon resonance of colloidal Au-modified gold films.* Sensors and Actuators B: Chemical, 1999. **54**(1): p. 118-124.
179. Ducker, R.E., M.T. Montague, and G.J. Leggett, *A comparative investigation of methods for protein immobilization on self-assembled monolayers using glutaraldehyde, carbodiimide, and anhydride reagents.* Biointerphases, 2008. **3**(3): p. 59-65.
180. Love, J.C., et al., *Self-assembled monolayers of thiolates on metals as a form of nanotechnology.* Chemical reviews, 2005. **105**(4): p. 1103-1170.
181. Hermanson, G., *Bioconjugate techniques.* 2008.
182. Vashist, S., et al. *Quantification of human immunoglobulin G immobilized on gold-coated silicon chip for biosensing applications*. in *Journal of Physics: Conference Series*. 2006. IOP Publishing.
183. Zhou, J., *Indium tin oxide (ITO) deposition, patterning and Schottky contact fabrication.* 2006.
184. Vermeer, A.W. and W. Norde, *The thermal stability of immunoglobulin: unfolding and aggregation of a multi-domain protein.* Biophysical Journal, 2000. **78**(1): p. 394-404.
185. Trilling, A.K., J. Beekwilder, and H. Zuilhof, *Antibody orientation on biosensor surfaces: a minireview.* Analyst, 2013. **138**(6): p. 1619-1627.
186. Hale, G., et al., *Repeated cleaning of protein A affinity column with sodium hydroxide.* Journal of immunological methods, 1994. **171**(1): p. 15-21.
187. Briand, E., et al., *Immobilization of Protein A on SAMs for the elaboration of immunosensors.* Colloids and Surfaces B: Biointerfaces, 2006. **53**(2): p. 215-224.
188. Tinguely, J.-C., et al., *Gold nanoparticles for plasmonic biosensing: the role of metal crystallinity and nanoscale roughness.* BioNanoScience, 2011. **1**(4): p. 128-135.

Vita

EDUCATION

B.E. *(with distinction)* Electronics Engineering – June 2006
SGSITS, Indore, India.

RESEARCH EXPERIENCE

Graduate Research Assistant
Nanophotonics Group, Integrated Nanoscale Engineering – 2009-Present
University of Kentucky, Lexington, KY

Lab Associate,
Electron Beam Lithography Group – 2008-2009
University of Kentucky, Lexington, KY

PUBLICATIONS

Peer-reviewed

- "Using U-shaped localized surface plasmon resonance sensors to compensate for non-specific interactions", **Neha Nehru**, Linliang Yu, Yinan Wei and J. Todd Hastings, *IEEE Transactions on Nanotechnology,* 13, 2014
- "Site-specific growth of CdS nanostructures", M. Bresin, B.R. Nadimpally, **N. Nehru**, V. Singh and J.T. Hastings, *Nanotechnology,* 24, 2013
- "Differentiating surface and bulk interactions using localized surface plasmon resonances of gold nanorods", **Neha Nehru**, Eugenii U. Donev, Gazi M. Huda, Linliang Yu, Yinan Wei, and J. Todd Hastings, *Optics Express*, 20, 2012.
  Also selected for Virtual Journal of Biomedical Optics, vol. 20(7).

Conference proceeding

- "Optical sensing characteristics of nanostructures supporting multiple localized surface plasmon resonances", **Neha Nehru** and J. Todd Hastings, *Proc. SPIE 8594, Nanoscale Imaging, Sensing and Actuation for Biomedical Applications IX, 859405*, 2013.
- "Focused electron-beam induced deposition of plasmonic nanostructures from aqueous solutions", M. Bresin, **N. Nehru** and J. Todd Hastings, *Proc. SPIE 8613, Plasmonic Structures I, 86135*, 2013.
- "Multi-mode localized surface plasmon resonance sensors for compensation of interfering effects", **Neha Nehru**, Linliang Yu, Yinan Wei and J. Todd Hastings, *Nanotechnology (IEEE-NANO), 2012 12th IEEE Conference on*, vol., no., pp.1-4, 20-23, 2012.

AWARDS

- Kentucky Graduate Student Scholarship – University of Kentucky – 2013.
- Graduate Student Travel Award – University of Kentucky – 2011, 2012.
- 1st place – Poster Competition – *Center for Nanoscale Science and Engineering (CENSE) 2nd Annual Nanotechnology Contest* – University of Kentucky – 2011.
- International Student Tuition Scholarship – University of Kentucky – 2007.

PROFESSIONAL MEMBERSHIP & SERVICES

- Reviewer – *Optical Society of America*.
- Student member – *SPIE* – 2012-present.
- Student member – *IEEE* – 2006-2010.

SELECTED PRESENTATIONS

1. **N. Nehru** and J. T. Hastings. Novel Interference compensated localized surface plasmon resonance sensing technique. 2013 Kentucky nanoSymposium, Louisville, USA, Aug 16-17, 2013. (Oral)
2. **N. Nehru** and J.T. Hastings. Optical sensing characteristics of nanostructures supporting multiple localized surface plasmon resonances. *SPIE BiOS*, San Francisco, USA, Feb 2-7, 2013. (Oral)
3. M. Bresin, **N. Nehru** and J. T. Hastings. Focused electron-beam induced deposition of plasmonic nanostructures from aqueous solutions. *SPIE MOEMS-MEMS*, San Francisco, USA, Feb 2-7, 2013. (Oral)
4. **N. Nehru**, L. Yu, Y. Wei and J. T. Hastings. Multimode Localized Surface Plasmon Resonance Sensors for Compensation of Interfering Effects. *IEEE Conference on Nanotechnology*, Birmingham, UK, Aug 21 – 23, 2012. (Oral)
5. **N. Nehru**, E. U. Donev and J. T. Hastings. Differentiating Surface and Bulk Interactions using Localized Surface Plasmon Resonances of Gold Nanorods. *Nanoplasmonics Sensors and Spectroscopy*, Gothenburg, Sweden, September 19 – 22, 2011. (Poster)